Development of a Laser-Wire Beam Profile Monitor for PETRA-III and CLIC

Thomas Aumeyr

Department of Physics
Royal Holloway, University of London

A thesis submitted to the University of London for the
Degree of Doctor of Philosophy

February 13, 2013

DECLARATION

I confirm that the work presented in this thesis is my own. Where information has been derived from other sources, I confirm that this has been indicated in the document.

Thomas Aumeyr

Abstract

The Compact Linear Collider (CLIC) is a proposed electron-positron collider with a centre-of-mass energy of 0.5 to 5 TeV, optimised for a nominal centre-of-mass energy of 3 TeV, at high luminosities exceeding 10^{34} $cm^{-2}s^{-1}$. The high beam charges in the CLIC beams make classical techniques for measuring the transverse beam size such as optical transition radiation (OTR) screens or wire scanners very difficult, which necessitates the use of non-invasive beam-size monitors. The laser-wire is a system that meets these requirements; it uses inverse Compton scattering to determine transverse beam-sizes by scanning a laser beam across the electron beam.

This thesis describes how such a laser-wire system was installed and operated at PETRA-III at DESY, which uses an automated mirror to scan a Q-switched laser pulse across the electron beam and is developed from the system previously operated at PETRA-II.

The measurements of key performance parameters are described and used in determining the emittance of the PETRA-III beam. The thesis includes a detailed investigation of the laser system as well as the collision measurements. Furthermore, simulations were carried out to design a similar system for the proposed transfer line of the CLIC Drive-Beam and the necessary baseline characteristics of such a system are described.

Zusammenfassung

Der Compact Linear Collider (CLIC) ist vorgeschlagener Elektron-Positron-Beschleuniger mit einer Schwerpunktsenergie von 0.5 bis zu 5 TeV, optimiert für eine Schwerpunktsenergie von 3 TeV, bei hohen Luminositäten von über 10^{34} $\mathrm{cm}^{-2}\mathrm{s}^{-1}$. Die hohen Strahlladungen in den Teilchenstrahlen des CLIC erschweren klassische Techniken zur Messung der transversalen Strahlbreite, wie z.B. Übergangsstrahlungsdetektoren, erheblich. Dies führt zur Notwendigkeit des Einsatzes von nichtinvasiven Methoden zur Messung der Strahlbreite. Der Laserwire ist ein System, das diese Ansprüche erfüllt; es basiert auf dem Effekt der inversen Compton-Streuung und verwendet diese, um mit einem Laserstrahl, der quer durch den Elektronenstrahl getastet wird, die transversale Strahlbreite zu messen.

Die vorliegende Arbeit beschreibt, wie ein solches Laserwire-System am PETRA-III-Beschleuniger am DESY installiert und betrieben wurde. Dieses System verwendet einen automatisierten Spiegel, um einen Q-Switch-betriebenen Laserpuls durch den Elektronenstrahl zu tasten. Es ist eine Weiterentwicklung des Systems, welches vorher am PETRA-II-Beschleuniger eingesetzt wurde.

Die Messung von wichtigen Betriebsparametern wird beschrieben, mit denen dann die Emittanz des PETRA-III-Strahls bestimmt wird. Die Arbeit beinhaltet eine detaillierte Studie sowohl des Lasersystems als auch der Kollisionsmessungen. Darüberhinaus werden Simulationen für das Design eines ähnlichen Systems präsentiert, welches für die Verbindungsstrecke des CLIC Drive-Beams vorgeschlagen wird, und die notwendigen Grundsatzvoraussetzungen eines solchen Systems werden beschrieben.

First and foremost, I would like to thank my supervisor at RHUL, Grahame Blair, for his support, inspiration and guidance and also for taking the time for explanations and discussing results. I have greatly enjoyed working on the PETRA-III laser-wire and am deeply grateful for the help and input of the entire team, at RHUL and at DESY: Gary Boorman, Alessio Bosco, Vahagn Gharibyan, Gero Kube, Michael Seebach and Kai Wittenburg. I would also like to express my gratitude towards Lawrence Deacon, Thibaut Lefèvre and Piotr Skowronski from CERN, who were always available for answering questions.

A very big thank you also goes to all those people in the physics department at RHUL who provided further insight, feedback, advice and assistance, especially Stewart Boogert, Pavel Karataev and Stephen Molloy.

Furthermore, I would like to thank Neil Cooper-Smith, Richard D'Arcy, Dan Hayden, Andrea Hodgetts, Maximillian Micheler, Matthew Rose and Simon Schmidlin for being available for innumerable coffee chats, thus providing some welcome distraction from my work at RHUL (or sometimes UCL).

I am also incredibly grateful for the financial support and networking opportunities provided by the Marie Curie scheme and the DITANET network.

Ein großes Dankeschön geht natürlich auch an meine gesamte Familie. Ohne eure Motivation und Unterstützung, sowohl finanzielle als auch moralische, wäre ich mit Sicherheit nicht so weit gekommen.

To my partner Neale, who offered me unconditional love and support throughout the course of this thesis.

Contents

1 Thesis Overview **12**

1.1 Chapter 2 - CLIC Design Overview 12

1.2 Chapter 3 - Theory 12

1.3 Chapter 4 - The PETRA-III Laser-Wire 13

1.4 Chapter 5 - Laser-Wire Measurements 13

1.5 Chapter 6 - Simulations for the Laser-Wire in the CLIC Drive Beam Transfer Line 13

1.6 Personal Contributions 14

2 CLIC Design Overview **15**

2.1 Introduction 15

2.2 Parameters and general layout of the CLIC complex 17

2.3 Requirements for beam diagnostics 17

2.3.1 Overview of the Main Beam requirements 18

2.3.2 Overview of the Drive Beam requirements 20

2.3.3 Transverse profile measurements 22

2.4 Summary 25

3 Theory **26**

3.1 Transverse beam dynamics 26

3.1.1 Basic ideas 26

3.1.2 Equation of motion 27

3.1.3 Solution of trajectory equations 30

3.1.4 Dispersion 32

3.1.5 Beta function 33

3.1.6 Beam emittance and phase space ellipse . . . 35
3.1.7 Transformation of Twiss parameters . . . 37
3.1.8 Emittance measurement . . . 38
3.1.9 Beam dynamics summary . . . 41
3.2 Compton scattering . . . 41
3.2.1 Introduction to Gaussian wave optics . . . 42
3.2.2 Laser-wire Compton rates . . . 47
3.3 Synchrotron radiation . . . 49
3.3.1 Emission of radiation . . . 49
3.3.2 Spectrum of frequencies . . . 50
3.3.3 Expected backgrounds . . . 51

4 The PETRA-III Laser-Wire 52
4.1 The PETRA-III Accelerator Facility . . . 52
4.1.1 The storage ring . . . 53
4.1.2 Diagnostics beam-line . . . 54
4.2 The Laser-Wire Experiment . . . 57
4.2.1 Principle of operation . . . 57
4.2.2 Laser system . . . 59
4.2.2.1 Seed unit . . . 59
4.2.3 Optical components . . . 60
4.2.4 Calorimeter . . . 65
4.2.5 Cameras . . . 66
4.2.6 Data acquisition . . . 66
4.2.6.1 Timing . . . 68
4.2.6.2 User interface . . . 71
4.2.7 Data analysis . . . 71
4.2.7.1 Determine laser amplitude . . . 71
4.2.7.2 Determine transverse position . . . 73
4.2.7.3 Integrate and scale calorimeter output . . . 73
4.2.7.4 Display and bin data . . . 73
4.2.7.5 Fit binned data . . . 75

4.3 Characterisation of the Laser System 76
4.3.1 Pointing jitter 77
4.3.2 Transverse mode 77
4.3.3 Conclusions and discussion of discrepancies 84

5 Laser-Wire Measurements 85
5.1 Preliminary measurements 85
5.1.1 Translation stage linearity 85
5.1.2 Piezo range 86
5.1.3 Calorimeter behaviour 86
5.2 Benchmarking the Laser-Wire 88
5.3 Laser studies 89
5.3.1 Laser tilt 89
5.3.2 Vacuum window effect on spot size 90
5.4 Beam studies 91
5.4.1 Vertical bump 91
5.4.2 Adjusting the beam ellipse 92
5.4.3 Dispersion measurement 93
5.5 Conclusions and discussion of discrepancies 97

6 Simulations for the Laser-Wire in the CLIC Drive Beam Transfer Line 98
6.1 Transfer Line TL2 98
6.2 Proposed detector 99
6.3 Optics simulation using MADX 101
6.3.1 Tracking 101
6.4 Optics simulation using BDSIM 101
6.5 Simulations 105
6.5.1 Laser-wire Compton rates 105
6.5.2 Angular distribution 106
6.5.3 Separating the Compton photons 107
6.5.4 Signal detection efficiency 108
6.5.5 Energy loss 111

6.5.6 Background from beam-gas bremsstrahlung 111
6.5.7 Measurement sensitivity 112
6.5.8 Finding a laser-wire location 114
6.5.8.1 Emittance measurement 116
6.5.8.2 Energy spread measurement 118
6.5.8.3 Independent emittance measurement ($\frac{\Delta E}{E} \neq 0$) 120
6.5.8.4 Independent emittance measurement ($\frac{\Delta E}{E} = 0$) 122
6.6 Summary 125

7 Conclusions and Outlook **127**
7.1 Summary and main conclusions 127
7.2 Future work - PETRA-III laser system upgrade 128

List of Figures

2.1 General layout of CLIC Complex at 3 TeV 17
2.2 CLIC module layout 19
2.3 Full Drive Beam complex 21

3.1 Circular coordinate system. 26
3.2 A diagram showing the relationship between the shape and orientation of the ideal phase ellipse and the Twiss parameters. 36
3.3 Feynman diagrams for Compton scattering (s and t channel respectively). . . . 41
3.4 Normalised cross-section $\frac{\sigma_C}{\sigma_T}$ plotted versus the scattered photon energy. 43

4.1 Overview of PETRA storage ring. 53
4.2 Overview of the diagnostics beam-line starting from the entrance absorber. . . . 55
4.3 Vacuum chamber for the x-ray optics. The inserts show a single refractive lens and a photo of the pinhole respectively. 56
4.4 A diagram of the overlap of the laser and electron beams. 57
4.5 LW location at the PETRA-III facility. 58
4.6 Overview of the LW setup. 59
4.7 Schematic layout of the setup in the laser hut. 60
4.8 Superimposed oscilloscope traces of the laser pulse as measured by a fast photodiode (rise time $\sim$ 1 ns) when the laser was unseeded (a) and seeded (b). 61
4.9 Unseeded single pulse internally (i) and externally (ii) triggered; unseeded envelope internally (iii) and externally (iv) triggered. 62
4.10 Schematic layout of the vertical breadboard. 63
4.11 Photograph of the LW optical breadboard. 64

4.12 LW scanning unit. 64
4.13 LWDAQ process distribution. 67
4.14 LWDAQ communication overview. 68
4.15 LWDAQ acquisition flowchart. 69
4.16 LWDAQ acquisition timing. 70
4.17 LWDAQ Petra-Laser-DAQ synchronisation. 70
4.18 Timing the laser pulse with respect to the PETRA-III revolution clock. 71
4.19 User Interface of LWDAQ. 72
4.20 Steps of the data analysis process. 72
4.21 Example traces of sampled laser pulses, displayed (a) in the full 150 ns sampling range and (b) further zoomed in. 73
4.22 Example calorimeter output of a Compton event: (a) raw trace and (b) windowed signal with pedestal removed. 74
4.23 The integrated calorimeter pulses plotted against the transverse position: (a) scatter plot and (b) binned. 74
4.24 Example binned scan profiles with applied fit. 76
4.25 Histograms showing the pointing jitter at the laser IP for the LAP 250 lens (a) and the LAP 750 lens (b) respectively. 77
4.26 Laser pulse image taken using CCD profiling equipment in the post IP section of the LW system. 78
4.27 CCD image of a laser pulse in the far field. 80
4.28 Binned laser pulse profiles fitted with the mode-mixing Gaussian fit-function in Eq. 4.3. 81
4.29 Parameters of the mode-mixing Gaussian fit in Eq. 4.3 along the longitudinal axis for the LAP250 lens. 82
4.30 σ of the mode-mixing Gaussian fit in Eq. 4.3 plotted against the stage position along the longitudinal axis for the LAP250 lens. 82
4.31 Parameters of the mode-mixing Gaussian fit along the longitudinal axis for the LAP750 lens. 83
4.32 σ of the mode-mixing Gaussian fit plotted against the stage position along the longitudinal axis for the LAP750 lens. 84

5.1 Measured laser centroid position versus set translation stage position for both scan axes. The proportionality factor is given in the legend. 86
5.2 Measured laser centroid position versus applied piezo voltage for both scan axes. The proportionality factor is given in the legend. 87
5.3 Measured calorimeter charge versus signal spread. The fit on the right plot was performed using the function in Eq. 5.1. 87
5.4 Schematic illustrating how the beam size measurement is affected by a tilted laser beam. 89
5.5 Vertical scan profiles, before (a) and after (b) bumping the beam vertically by 1 mm. 91
5.6 Measured vertical beam sigma versus the current applied to quadrupole QS1 and QS4 respectively 92
5.7 Measured horizontal beam sigma versus the current applied to quadrupole QS1 and QS4 respectively. 93
5.8 Laser timing delay versus frequency shift. The proportionality factor is also given in the legend. 95
5.9 Horizontal beam position versus frequency shift. The proportionality factor of the linear fit is given in the legend. 95
5.10 Vertical beam position versus frequency shift. The proportionality factor of the linear fit is given in the legend. 96

6.1 BDSIM visualisation of the end of the straight section of TL2 99
6.2 Theoretical beam sigma without an energy spread. 102
6.3 Theoretical beam sigma with an energy spread of $\frac{\Delta E}{E} = 0.0033333$. 102
6.4 Beam sigma of the tracked particles without an energy spread. 103
6.5 Beam sigma of the tracked particles with an energy spread of $\frac{\Delta E}{E} = 0.0033333$. 103
6.6 Energy distribution of the electrons at injection. 104
6.7 Energy distribution of the Compton-scattered electrons after the laser IP. 104
6.8 Energy distribution of the Compton photons. 105
6.9 Simulated scan profile at the laser-wire IP for a laser with $M^2 = 1.3$ and wavelength $\lambda = 1064$ nm. 106

6.10 Evolution of the energy of the scattered photons as a function of the observation angle. 107
6.11 Sketch illustrating the photon separation. 108
6.12 Horizontal distribution of the electrons before the bending magnet. 109
6.13 Horizontal distribution of the photons before the bending magnet with respect to the beam centroid. 109
6.14 Horizontal distribution of the photons after the bending magnet with respect to the beam centroid. 110
6.15 Efficiency of Compton detection over distance. 110
6.16 Energy loss per metre of the Compton photons normalised to one Compton event. 111
6.17 Beta functions and horizontal dispersion over the last 100 m of the straight section in TL2. 113
6.18 Theoretical beam size $\sigma_{x,y}$ over the last 100 m of the straight section in TL2. . . 113
6.19 Sensitivity of the beam size measurement with respect to the horizontal emittance and the dispersion over the last 100 m of the straight section in TL2. . . . 114
6.20 Theoretical detection efficiency over the last 100 m of the straight section in TL2. 115
6.21 Effective sensitivity of the beam size measurement with respect to the horizontal emittance and the energy spread. 115
6.22 Horizontal dispersion and effective sensitivity of the beam size measurement with respect to the horizontal emittance. 116
6.23 Horizontal beta function and effective sensitivity of the beam size measurement with respect to the energy spread. 117
6.24 Proposed location for a laser-wire experiment, optimised for measuring the horizontal emittance. 118
6.25 Proposed location for a laser-wire experiment, optimised for measuring the energy spread. 119
6.26 Studied locations for a three-fold laser-wire experiment, optimised for measuring the emittance independently. 121
6.27 MC simulation of the emittance measurement with an LW transversal profile measurement error of 1.8%. 122

6.28 MC simulated emittance and emittance error versus increasing LW transversal profile measurement error. 123
6.29 Studied locations for a three-fold laser-wire experiment, optimised for measuring the emittance independently ($\frac{\Delta E}{E} = 0$). 124
6.30 MC simulation of the emittance measurement with an LW transversal profile measurement error of 1.8%. 124
6.31 MC simulated emittance and emittance error versus increasing LW transversal profile measurement error. 125

7.1 Longitudinal development of the horizontal (a) and vertical (b) spot size of the laser before entering the fibre. 130
7.2 Oscilloscope trace showing a single laser pulse. 131

List of Tables

2.1 3-TeV CLIC parameter list. 18
2.2 Transverse beam size requirements for the Main Beam. 23
2.3 Transverse beam size requirements for the Drive Beam. 23

4.1 PETRA-III machine parameters. 54
4.2 Table of parameters for the WinCamD UCM CCD camera. 66
4.3 Table of parameters for the Basler A601f CMOS camera. 66
4.4 Input parameters for the convolved profile fit. 75
4.5 Fit parameters for the Rayleigh fit for the LAP250 lens. 79
4.6 Fit parameters for the Rayleigh fit for the LAP750 lens. 83

5.1 Comparing the results of the laser-wire and the synchrotron radiation imaging system. 88
5.2 Results from the quadratic fit for the beam ellipse orientation. 93

6.1 ATF parameter list. 100
6.2 Parameter values and errors for the emittance measurement. 118
6.3 Parameter values and errors for the energy spread measurement. 121

Chapter 1

Thesis Overview

The topic of this thesis is research and development towards a laser-wire capable of measuring transversal beam sizes for the Compact Linear Collider (CLIC). Part of the work involves developing and testing such a system at PETRA-III, the third incarnation for the PETRA storage ring (Positron-Elektron-Tandem-Ring-Anlage, "positron-electron tandem-ring facility") at DESY (Deutsches Elektronen Synchrotron, "German Electron Synchrotron") in Hamburg, Germany. At PETRA-III, various beam studies were carried out with the laser-wire system in order to further an understanding of certain beam parameters. Also, simulations were carried out for a suggested laser-wire in the CLIC Drive-Beam transfer line TL2.

1.1 Chapter 2 - CLIC Design Overview

The thesis starts with motivating the need for a future e^+e^- collider. The general layout of the CLIC complex is presented and key parameters are introduced. The principal functions for both the Main and the Drive Beam, are explained and requirements are defined. Specifications for measuring the transverse beam profile in the Drive Beam are explained.

1.2 Chapter 3 - Theory

The accelerator and laser physics relevant to the experimental work and simulations that were carried out are explained. Hill's equation and its solution are derived and the concept of *emittance* is defined. Emittance is a conserved quantity, which is shown using Liouville's theorem.

The solutions to Hill's equation are the introduced in matrix notation, which leads to the definition of the *Twiss parameters*. This matrix description is then used to explain how emittance measurements are carried out and also adapted to include the effects of *dispersion*.

The principle of Compton scattering is illustrated. Laser propagation theory is explained together with deriving the rate of Compton scattering. This is applied to motivate the measurement of the electron beam sizes using a laser-wire.

Synchrotron radiation (SR) is the main source of background for the Laser-wire signal. Therefore, equations for SR power and spectrum are presented.

1.3 Chapter 4 - The PETRA-III Laser-Wire

The PETRA-III accelerator facility and the laser-wire (LW) setup as well as the diagnostics beam-line are described and the principle of operation of the laser-wire system is explained. The laser system and its components are described and measurements of several characteristics are presented.

The hardware and functionality of the data acquisition system is described and the data analysis procedure is explained.

1.4 Chapter 5 - Laser-Wire Measurements

Preliminary measurements of the laser-wire system are explained and the results are given. Possible limitations on the scan accuracy are introduced and ruled out. Laser-wire scans for varying beam parameters and their results are presented and conclusions towards functionality are drawn.

1.5 Chapter 6 - Simulations for the Laser-Wire in the CLIC Drive Beam Transfer Line

The CLIC Drive-Beam transfer line TL2 and its components are presented. The need for a Cerenkov radiation detector is motivated to be used in the laser-wire setup at the CLIC Drive-Beam transfer line TL2. The Cerenkov detector for the laser-wire at the ATF2 extraction line is introduced and key parameters and performance are explained. The electron beam optics

processing software MADX and the beam line simulation toolkit BDSIM are introduced. Simulations of the laser-wire signal are described and the results are presented. Calculations of beam-gas bremsstrahlung related background are presented. Conclusions are drawn regarding the location of the laser-wire and the Compton photon detector in the transfer line TL2.

1.6 Personal Contributions

I worked on and developed the following:

- Together with Alessio Bosco, installation, alignment and re-alignment of the optical components of the LW system, in the laser-hut as well as on the breadboard in the PETRA-III tunnel during access; data acquisition for the transversal laser profiles and other characteristics.
- Evaluation and fitting of the laser data and modelling the laser pulse.
- Together with Gary Boorman, installation and synchronisation of the data acquisition hardware; development of parts of the control software for the DAQ.
- Acquisition of LW scan data either parasitically with PETRA-III running in normal user shifts or in shifts with dedicated fill patterns and machine settings (skew quadrupole current, horizontal beam bump, frequency shift).
- Programming the analysis software package.
- Simulation of the CLIC Drive-Beam TL2 laser-wire system including all beam line components to determine the best location for a possible beam diagnostic system.

Chapter 2

CLIC Design Overview

The contents of this chapter are a summary of the 2008 parameters note [1] and the up-coming conceptual design report [2].

2.1 Introduction

The next energy frontier in High Energy Physics is the TeV energy range, and will first be explored by the LHC which has been on-line since the end of 2008. The data of this collider are highly anticipated and will set the direction in which high energy particle physics will go in the next decade and beyond. Just as e^+e^- colliders complemented hadron-hadron colliders in the 100 GeV energy range, thus validating much of the Standard Model, it is expected that higher-energy e^+e^- colliders will be needed to study TeV physics in greater detail, if discovered by the LHC. Their main advantage is that they provide very clean experimental environments and produce all particles within the accessible energy range democratically, including those with only electroweak interactions. These considerations motivate several projects for future e^+e^- colliders. CLIC has the so far unique feature that it aims for an e^+e^- centre-of-mass energy of 0.5 to 5 TeV, at high luminosities around 10^{35} cm^{-2}s^{-1}. It is optimised for a nominal center-of-mass energy of 3 TeV.

In order to keep the size of a linear collider within reason, i.e. smaller than about 50 km, the accelerating gradient to reach a centre-of-mass energy of 3 TeV must be higher than 100 MV/m. Superconducting (SC) technology is excluded because of the fundamental limit on the peak magnetic field, which results in an achievable gradient of 'only' about 60 MV/m. Higher gradi-

ents (>50 MV/m) are only reachable with normal conducting (NC) accelerating structures. As NC standing wave structures would have high ohmic losses, travelling wave structures must be used. In these structures, the RF pulse 'flows' with group velocity v_g along the structure into a load at the structure exit and particles 'surf' the electromagnetic wave.

The full accelerating fields are established after the cavity filling time, which is not useful for the beam and thus long beam pulse lengths are favoured. The pulse length must be sufficiently long compared to the fill time of the structure to accelerate a bunch train which provides a good luminosity-to-power ratio. However, the pulse length is limited by an increased probability of breakdown and by an increased level of pulsed surface heating.

The accelerating gradient is limited by various effects:

- The magnetic RF field heats up the walls in the RF cavities which causes extensions and therefore compressive stress. This can lead to fatigue in the material resulting in cracks. The temperature rise in the structure is proportional to the square root of the pulse length and the square of the peak magnetic field [3]. The field can only be reduced by changing geometry, but a high field is needed for high gradient. This therefore limits the maximum pulse length to short pulses of about a few 100 ns.

- RF breakdowns are a severe problem in high power RF applications and limit the achievable gradient and the efficiency of RF accelerating structures. Breakdowns damage the structures because a local plasma triggered by field emission leads to erosion of the surface. This effect limits the lifetime of the structure. The surface of the RF material has some intrinsic roughness from the machining process which enhances the electric field locally. To reach the ultimate gradient, the structure must be conditioned by gradually increasing the RF power with time. This RF processing can melt field emission points and the surface becomes smoother thus reducing the local field enhancement. In this way higher electric fields with fewer breakdowns can be achieved.

  The conditioning process however is also limited by electrons with sufficient energy to generate a plasma. This plasma melts the surface which then splatters and generates new field emission points. Excessive fields can also damage the structures. The goal is to design a structure with low ratio of electric field on the surface to the accelerating field. Also, new materials such as molybdenum and tungsten are being studied.

- RF power flow and/or iris aperture also have a strong impact on the achievable accelerating gradient and on surface erosion [3].

2.2 Parameters and general layout of the CLIC complex

A general layout of the CLIC complex is depicted in Fig. 2.1 and a list of overall parameters can be found in Tab. 2.1.

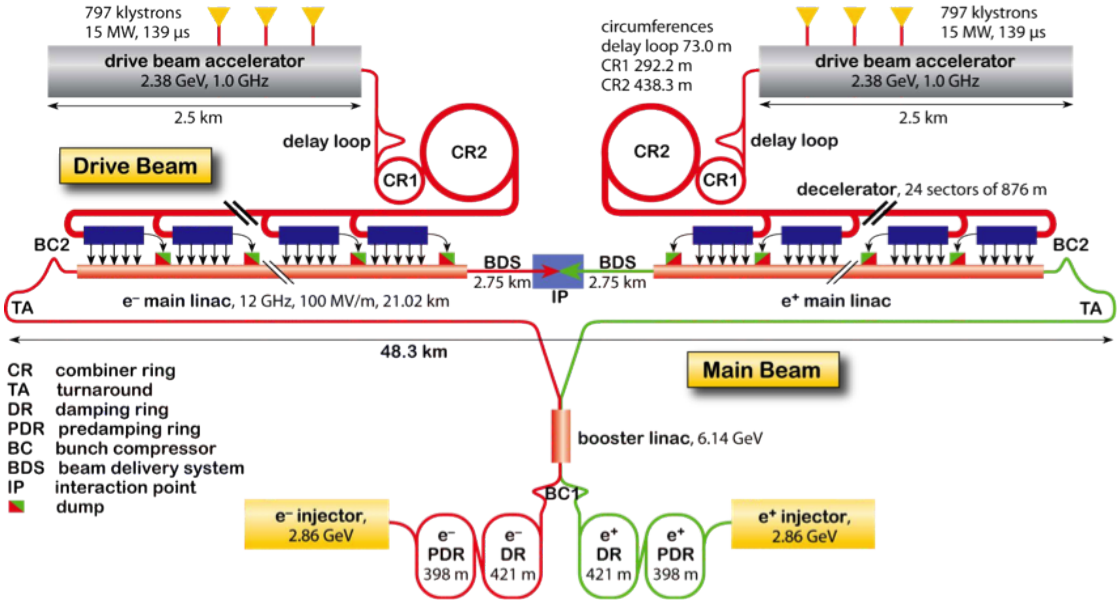

Figure 2.1: General layout of CLIC Complex at 3 TeV

The main components of the CLIC complex and their requirements on beam diagnostics in general and transverse beam profile measurement in particular are presented in the following sections.

2.3 Requirements for beam diagnostics

Beam dynamic considerations demand very tight tolerances on most beam parameters and these in turn dictate most of the requirements for beam instrumentation. Particle beams with extremely small emittances are generated in the damping rings and these must be conserved over more than 40 km of beam lines. This requires a precise control of the beam position over a long distance. Just before the main linac, the bunch length must be compressed and controlled at the femtosecond level. After the final focus, the beam has only a few nanometers in transverse

Table 2.1: 3-TeV CLIC parameter list [4].

Parameter	Symbol	Value	Unit
Center of mass energy	E_{cm}	3000	GeV
Main Linac RF Frequency	f_{RF}	11.994	GHz
Total luminosity	L	5.9	10^{34} cm^{-2}s^{-1}
Peak luminosity (in 1% of energy)	$L_{99\%}$	2	10^{34} cm^{-2}s^{-1}
Linac repetition rate	f_{rep}	50	Hz
No. of particles / bunch	N_b	3.72	10^9
No. of bunches / pulse	k_b	312	
Bunch separation	Δt_b	0.5 (6 RF periods)	ns
Bunch train length	τ_{train}	156	ns
Beam power / beam	P_b	14	MW
Unloaded / loaded gradient	$G_{unl/l}$	120 / 100	MV/m
Overall two linac length	l_{linac}	42.16	km
Total beam delivery length	l_{BD}	2×2.75	km
Proposed site length	l_{tot}	48.4	km
Total site AC power	P_{tot}	415	MW
Wall plug to main beam power efficiency	η_{tot}	7	%

size. Post-IP, the highly disrupted beams must be dumped cleanly, i.e. making sure that the power carried by the particles is safely absorbed. The CLIC technology relies on a two-beam acceleration scheme, where a second electron beam with a moderate energy but a high current and high bunch frequency is used to generate the radiofrequency power required to accelerate the main beam. The Drive Beam complex is basically a 12-GHz relativistic multi-beam klystron distributed over a distance of 48 km, which is supposed to provide power efficiently and reliably.

2.3.1 Overview of the Main Beam requirements

The electron source is based on a photo-injector with a direct current (DC) gun. Once extracted, the electrons are directly accelerated to 200 MeV in a linear accelerator using 2-GHz normal conducting cavities. The positron source relies on a much larger accelerator complex and requires a preliminary electron injector complex of 5 GeV. These electrons are then converted in a first target into high-energy photons, which then generate positrons through e^+/e^- pair production in a second target. The positron beam is then pre-accelerated to 200 MeV. Electrons and positrons are finally accelerated in a common 2 GHz linac up to 2.86 GeV.

The transverse normalised beam emittances are then reduced from mm·rad to nm·rad in two consecutive rings, the Pre-Damping Ring (PDR) and the Damping Ring (DR). In the injector

complex, the positron beam has an emittance about a hundred times larger than that of the electron beam. However, they both reach similar emittance values after the PDR. At the extraction of the DR, typical values are below 500 and 5 nm·rad for the horizontal and vertical emittances respectively.

Exiting the DR, the beam enters the Ring-To-Main-Linac (RTML) where the bunches are compressed in a first magnetic chicane, accelerated to an energy of 9 GeV in a Booster Linac and transferred to the entrance of the Main Linac through more than 20 km of beam line. After a final 1.5 km long turn-around loop, bunches are compressed even further in a second magnetic chicane to a final bunch length of 44 µm root mean square (RMS).

The beam is then accelerated in the Main Linac, consisting of more than 70,000 of 12 GHz accelerating structures arranged in units, so-called CLIC Modules. A schematic layout of one of these modules is shown in Fig. 2.2. The beam energy increases to 1.5 TeV over a total distance of 20.5 km. Along the entire linac, the beam properties (beam position, current, emittance, losses and bunch length) must be measured in a non-interceptive way to guarantee the overall performance of the machine and provide reliable information for feedback systems. In order to reach the design luminosity, the beam emittance growth from the DR to the IP must be kept below 20%. Thus, any active devices installed in the beam line (magnets, cavities, etc.) are demanded to be accurately aligned and stabilised which requires very precise tools to measure the beam positions and sizes.

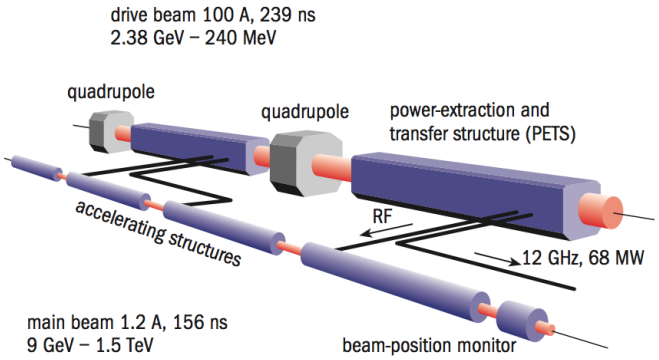

Figure 2.2: CLIC module layout

The beam is finally transported through the Beam Delivery System (BDS) to the IP. The BDS has three main purposes. Firstly, a beam diagnostic section characterises the beam properties by measuring emittance, energy and polarisation. Secondly, the beam is 'cleaned' by a collimation

system and thirdly, the final optic adjustment focusses the beam down to nanometre beam sizes at the IP.

Post-IP, the highly disrupted beam is then guided towards a huge water dump. This part of the machine is called the Spent Beam Line and has also some crucial impact for instrumentation. The CLIC luminosity monitor is based on the detection of beamstrahlung photons generated at the IP. The Spent Beam Line uses a combination of vertical bends to separate these high-energy photons from the charged particles themselves. An intermediate beam dump absorbs the particles with the lowest energy and the oppositely charged particles coming from coherent pair creation in the IP. Each magnet comes with its own protection system which consists of collimators and absorbers. At this point, the beam has a large energy spread and is then diluted using C-shape dipoles over the 30-cm aperture of the vacuum window. The beam is finally stopped in a water dump. In this line, the beam diagnostics do not require high precision, but must be reliable enough to prove the beam has been dumped correctly. The instrumentation consists mainly of beam loss and intensity monitors to check the efficiency of the intermediate dump, a series of beam position monitors to steer the beam through and few beam size monitors to confirm the dilution of the particles at the entrance of the dump.

2.3.2 Overview of the Drive Beam requirements

The Drive Beam (DB) linac uses fully loaded accelerating structures. The high pulse current of the CLIC DB (about 4 A), together with using short travelling wave accelerating structures with relatively low gradient, results in a highly efficient high energy transfer to the beam. No RF power is transmitted to the load when the beam is present, and the resistive losses in the cavity walls are minimal [3]. However, an energy transient is present at the beginning of the pulse, where the first bunches have double the energy compared to the steady state reached after the filling time. This mode of operation also strongly couples beam current fluctuations to the beam energy.

As mentioned above, the DB has an extremely high beam charge of 590 μC corresponding to a current of 4.2 A over a 140.3-μs long pulse. As a consequence, the technology for beam instrumentation has to be carefully chosen. Any intercepting devices would be limited to the observation of a small fraction of the DB, most likely by reducing its pulse length or current. The average radiation level would make radiation-hard designs necessary and the maintenance

work of such systems would need to be optimised.

Another special feature of the DB scheme comes from the beam frequency multiplication technique proposed to convert a long low intensity low frequency beam into a succession of shorter high intensity high frequency beams. In this way the necessary 12-GHz RF power is distributed to the MB accelerating structure, see Fig 2.3. The DB scheme uses RF deflecting cavities to inject and combine bunch trains. The performance of this operation relies heavily on longitudinal beam diagnostics capable of measuring the evolution of the bunch scaling with a good precision.

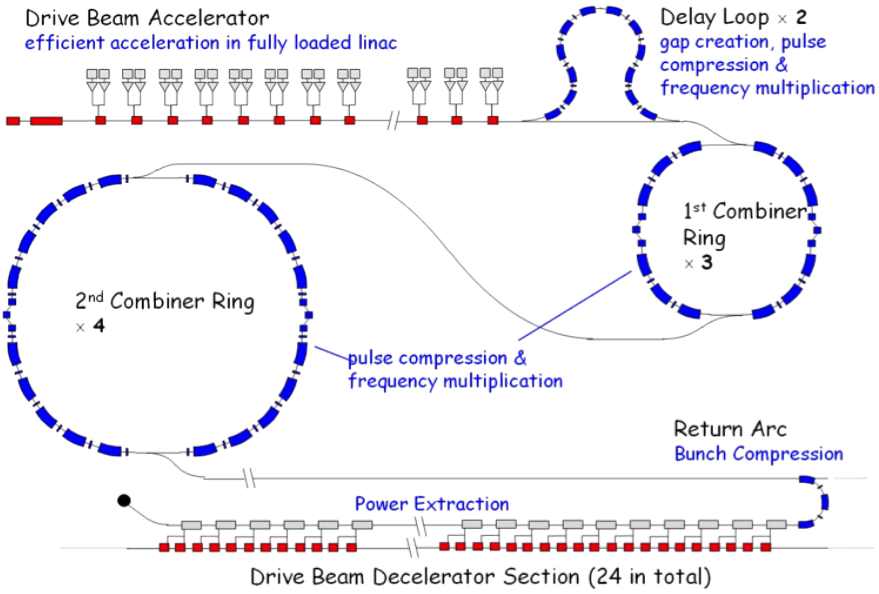

Figure 2.3: Full Drive Beam complex

Once the DB trains have been combined, they are sent down to the CLIC tunnel and distributed to their respective decelerator sectors using so called turn-around loops. The particle bunches are further compressed from 2 ps to 1.4 ps and finally 1 ps using two consecutive magnetic chicanes located just before and after the turn-arounds respectively. The precise synchronisation of the Main Beam with the RF power produced by the Drive Beam is also performed in the turn-arounds and is an important aspect of the two beam acceleration scheme. Timing errors lead to energy variations in the main linac and a subsequent reduction of luminosity. A timing jitter of 15 fs will give a luminosity reduction of around 2%.

It is very unlikely that the required phase tolerance in the turn-arounds of 0.1° at 12 GHz could be achieved without feedback, feedforward or both types of beam-based correction. A

possible scheme for CLIC is to measure the arrival time of the Drive and the Main beams in the transfer lines between the injector complex and the main linac. A high-precision local clock would be required to keep time from the arrival of the reference until the end of the drive beam train, 140 μs later. Precise time measurements of both beams are then performed and compared, and depending on the observed difference, a correction on the drive beam would be applied. Corrections could be achieved using RF structures, either with deflecting cavities or by adjusting the energy before the final DB bunch compressor. The system relies on a precise timing measurement by means of RF phase and amplitude measurements. A resolution better than 10 fs has been already demonstrated on CTF3 [5].

In the decelerator, the beam energy is gradually transformed into 12-GHz RF power over several hundred metres. Along the decelerator, the beam energy spread increases linearly to finally reach a value of 90% [3], which is unusual compared to any accelerator in the world. The beam optics must be adapted to provide constant RF power without allowing beam losses and relies therefore on the continuous monitoring of the beam properties.

2.3.3 Transverse profile measurements

In Tables 2.2 and 2.3, the requirements for transverse profile monitoring for the Main and the Drive Beam respectively are presented. The tables show the development of the normalised beam emittance throughout the CLIC complex together with the corresponding expected spatial resolution and the number of measurement devices requested. The beam energy is also given as it may influence the choice of detector technology. Furthermore, the typical charge densities are mentioned because they will set an upper limit for the damage threshold of intercepting devices like screens or wire scanners. For highly thermal-resistant materials like carbon, beryllium or silicon carbide, the limit corresponds to a charge density of 10^6 nC/cm^2 [6]. This number refers to the survival of the material after a single shot pulse and does not take into account thermal effects that would also need to be considered in the final design (e.g. machine repetition rate or material cooling).

In general, for the Drive Beam the beam size ranges from 20 μm to 2 mm both horizontally and vertically and for the Main Beam (after damping) from 1/10 to 50/500 μm in the horizontal and vertical respectively [7]. As a rule of thumb it can be said that resolution approximately tracks the beam size. From the emittance values in Table 2.2 and Table 2.3 and example values

Table 2.2: Transverse beam size requirements for the Main Beam (H and V indicate horizontal and vertical) [2].

Machine Sub-systems	Emittance [nm·rad]	Energy [GeV]	Resolution [μm]	Quantity	Charge density [nC/cm^2]
e^- source & pre-injector	10^5	< 0.2	50	2	$< 5 \cdot 10^5$
e^+ source & pre-injector	$93 \cdot 10^5$	< 0.2	50	4	$< 5 \cdot 10^5$
Injector Linac (e^-/e^+)	$1/93 \cdot 10^5$	< 2.86	50	2	$< 5 \cdot 10^5$
Pre-Damping Rings (H/V)	$63/1.5 \cdot 10^3$	2.86	50/10	4	$< 5 \cdot 10^6$
Damping Rings (H/V)	<500/5	2.86	10/1	4	$< 5 \cdot 10^8$
RTML (H/V)	510/5	< 9	10/1	70	$< 5 \cdot 10^8$
Main Linac (H/V)	600/10	< 1500	10/1	48	$< 5 \cdot 10^8$
BDS (H/V)	660/20	1500	10/1	8	$< 5 \cdot 10^8$
Spent Beam Line (H/V)	>660/20	<1500	1000	6	$< 5 \cdot 10^3$

Table 2.3: Transverse beam size requirements for the Drive Beam [2].

Machine Sub-systems	Emittance [nm·rad]	Energy [GeV]	Resolution [μm]	Quantity	Charge density [nC/cm^2]
Source & Linac	100	< 2.37	50	10	$< 40 \cdot 10^6$
Frequency Multiplication	100	2.37	50		$< 40 \cdot 10^6$
(Delay Loops/Combiner Rings/Transfer Lines)				6/8/6	
Transfer to Tunnel	100	2.37	50		$< 40 \cdot 10^6$
(Electron Loop/Transfer to Tunnel/Long Transfer Lines)				2/0/0	
Turn-arounds	100	2.37	50	96	$< 1.5 \cdot 10^6$
(Bunch Compressor 1/Turn-arounds/Bunch Compressor 2)					
Decelerator	150	< 2.37	50	576	$> 1.5 \cdot 10^6$
Dump Lines	> 150	< 2.37	100	96	$> 1.5 \cdot 10^6$

of the beta functions given in [2], a few indicative beam sizes can be estimated. Just before the main linac, $\beta_x = 40$ m and $\beta_y = 18$ m which leads to $\sigma_x = 37$ µm and $\sigma_y = 3$ µm. The initial part of the BDS, from the end of the main linac to the start of the collimation system, is where the properties of the beam are measured and corrected before it enters the Collimation and Final Focus system. Here, the beta functions are approximately $\beta_{x/y} = 140$ m which results in beam sizes of $\sigma_x = 6$ µm and $\sigma_y = 1$ µm. Transfer line TL2 is located in the frequency multiplication section of the Drive Beam linking the two combiner rings (CR1 and CR2). Here the beam sizes are roughly between 250 and 650 µm (see Section 6.3). In the DB decelerator, the maximum beta function is given as 3.4 m and the initial maximal beam size is $\sigma_{x/y} = 0.3$ mm.

From the source of the Main Beam to the end of the injector linac, the resolution of 50 µm can be achieved using standard techniques such as optical transition radiation (OTR) screens or wire scanners as the expected charge densities are compatible with the use of interceptive techniques. OTR screens image the beam in a single shot whereas wire scanners only give beam profiles over several shots. However, wire scanners are less interceptive than screens for which the beam is most likely to be dumped afterwards. These technologies have been used for 20-30 years and recent systems have even achieved a resolution of a few µm [8, 9, 10].

The emittance of the Main Beam is significantly reduced first in the PDR and finally in the DR. Consequently, typical beam sizes shrink which requires a much better spatial resolution for the beam size measurement. This issue has been studied during the last ten years either to optimise the performance of 3rd generation synchrotron light sources or in the framework of the ILC/CLIC studies with R&D programmes aiming to prove the feasibility of low emittance generation in damping rings. Several techniques have been developed which can provide beam size measurements with resolution of the order of 1 µm.

For highly relativistic particles, the spatial resolution of an imaging system using Synchrotron Radiation (SR) is intrinsically limited by diffraction, which can be minimised by using shorter wavelengths (see Section 3.3). To provide a resolution of the order of 1 µm, imaging systems were developed in the X-ray regime using X-ray lenses and cameras [11, 12]. Another technique based on the measurements of the Point Spread Function (PSF) on an imaging system has been developed and successfully tested at MAX-lab [13]. However, contrary to the rings or turnarounds, where synchrotron radiation could be envisaged as a natural source of light for instrumentation, there is no natural source of photons in a linear accelerator. The use of inter-

cepting devices must be restricted to single bunch mode to prevent any beam-induced damages.

In terms of spatial resolution, the transverse profile monitors for the Drive Beam do not need to be as accurate and could be achieved with classical instruments like OTR screens or wire scanners. However, the major constraint comes from the high beam charge which causes a difficulty for the use of any interceptive monitors.

Laser-wires are well suited for use at CLIC because they are relatively non-invasive devices that can be used continuously during machine operation. They are also suitable for very high intensity beams, whereas solid wires would be destroyed. They can also be used for beam sizes approaching the wavelength of the laser-light. Typically light of wavelength 532 nm has been used to date, however shorter wavelength light has been used at SLC [14]. The interplay between laser-wire location and the corresponding technical requirements on the laser-wire systems, including Compton signal extraction, needs to be integrated into the beamline design throughout the machine.

2.4 Summary

For CLIC, the Drive Beam will require 800 laser-wire installations, the Main Beam will require 134. Development of a cheap, robust, flexible laser-wire system is clearly need. Studies and simulations for a laser-wire system at the Drive Beam transfer line TL2 are presented in Chapter 6. To showcase an example for such a system, Chapter 4 presents the operating laser-wire beam profile monitor at PETRA-III.

Chapter 3

Theory

This chapter presents the theoretical background required for understanding the laser-wire system and summarises the necessary principles in accelerator beam optics, laser optics and Compton scattering.

3.1 Transverse beam dynamics

This section gives an overview basic accelerator beam dynamics and outlines the concept of emittance [15].

3.1.1 Basic ideas

In Fig. 3.1, an ideal circular orbit of a particle in an accelerator is shown, where ρ is the orbit radius and θ the angular coordinate.

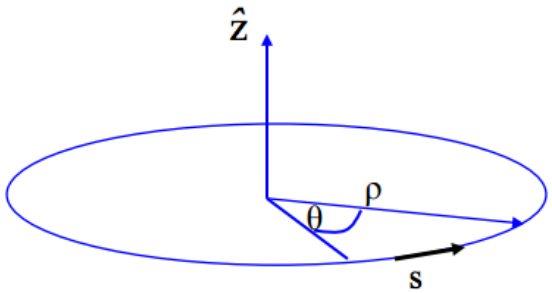

Figure 3.1: Circular coordinate system.

In such an orbit, a transverse deflecting force is needed, the so-called Lorentz force F_L. It is

defined as

$$\mathbf{F_L} = q \cdot (\cancel{\mathbf{E}} + \mathbf{v} \times \mathbf{B}), \tag{3.1}$$

where q is the particle charge, E the electric field, v the particle velocity and B the magnetic field. Since the typical velocity in high energy machines is about the speed of light, the electric field term is small in comparison and can be neglected.

The condition for an ideal circular orbit is that the Lorentz force and the centrifugal force,

$$F_{Zentr} = \frac{\gamma m_0 v^2}{\rho}, \tag{3.2}$$

are equal, where γ is the relativistic Lorenz factor and m_0 the rest mass of the particle. For an electron, this leads to

$$\begin{aligned} F_L &= F_{Zentr} && (3.3)\\ q\cancel{v}B &= \frac{\gamma m_0 \cancel{v^2}}{\rho} && (3.4)\\ \frac{p}{e} &= B\rho, && (3.5) \end{aligned}$$

where $B\rho$ is called beam rigidity.

3.1.2 Equation of motion

For deriving the equation of motion for a particle in a circular accelerator, a linear approximation is considered. The ideal particle travels around the design orbit, any other particle occupies coordinates x, y which are small quantities away from the ideal orbit. Since x, y are much smaller than the radius of the ideal orbit, ρ, only linear terms in x and y of the magnetic field, B, have to be taken into account. The vertical component of the magnetic field, B_y, can expanded as

$$\begin{aligned} B_y(x) &= B_{y0} + \frac{dB_y}{dx}x + \cancel{\frac{1}{2!}\frac{d^2B_y}{dx^2}x^2 + \ldots} && (3.6)\\ &\approx B_0 + gx. && (3.7) \end{aligned}$$

where g is the quadrupole gradient resulting in focusing forces to keep trajectories in vicinity of the ideal orbit.

The vertical field can then be normalised by the particle momentum $p/e = B\rho$, where e is

the charge of the electron. This results from the condition that for a circular orbit the Lorentz force must be equal to the centrifugal force. $B\rho$ is called beam rigidity.

$$\frac{B(x)}{p/e} = \frac{B_0}{B_0\rho} + \frac{gx}{p/e} \tag{3.8}$$

$$= \frac{1}{\rho} + kx, \tag{3.9}$$

where $k = \frac{g}{p/e}$.

Now considering a local segment of a particle trajectory, the radial acceleration a_r is

$$a_r = \frac{d^2\rho}{dt^2} - \rho\left(\frac{d\theta}{dt}\right)^2, \tag{3.10}$$

with time t and angle θ. For the ideal orbit, ρ is constant and therefore the resulting force becomes

$$F = m\rho\left(\frac{d\theta}{dt}\right)^2 = m\rho\omega^2 \tag{3.11}$$

$$= \frac{mv^2}{\rho}, \tag{3.12}$$

where m is the particle mass, ω is the angular velocity and $v = \omega\rho$ is the velocity. For a general trajectory, ρ is replaced by $\rho + x$. Therefore,

$$F = m\frac{d^2}{dt^2}(x+\rho) - \frac{mv^2}{x+\rho} = eB_y v. \tag{3.13}$$

As ρ is constant the first term reduces to

$$\frac{d^2}{dt^2}(x+\rho) = \frac{d^2}{dt^2}x. \tag{3.14}$$

Since x is in the order of mm and ρ in the order of m, the second term in Eq. 3.13 can be developed for small x,

$$\frac{1}{x+\rho} = \frac{1}{\rho} - \frac{1}{\rho^2}x + \cancel{\frac{1}{\rho^3}x^2 + \ldots} \tag{3.15}$$

$$\approx \frac{1}{\rho}\left(1 - \frac{x}{\rho}\right), \tag{3.16}$$

$$m\frac{d^2x}{dt^2} - \frac{mv^2}{\rho}\left(1-\frac{x}{\rho}\right) = eB_y v. \tag{3.17}$$

With the linear approximation of the magnetic field $B_y = B_0 + x\frac{dB_y}{dx}$, this becomes

$$m\frac{d^2x}{dt^2} - \frac{mv^2}{\rho}\left(1-\frac{x}{\rho}\right) = ev\left(B_0 + x\frac{dB_y}{dx}\right) \tag{3.18}$$

$$\frac{d^2x}{dt^2} - \frac{v^2}{\rho}\left(1-\frac{x}{\rho}\right) = \frac{evB_0}{m} + \frac{evxg}{m}. \tag{3.19}$$

At this point, a shift in variables has to be done ($t \to s$).

$$\frac{dx}{dt} = \frac{dx}{ds}\frac{ds}{dt} = x'v \tag{3.20}$$

$$\frac{d^2x}{dt^2} = \frac{d}{dt}\left(\frac{dx}{ds}\frac{ds}{dt}\right) = \frac{d}{ds}(x'v)v = \tag{3.21}$$

$$= x''v^2 + \frac{dx}{ds}\cancelto{0}{\frac{dv}{ds}}v, \tag{3.22}$$

where primes indicate derivatives with respect to s. This leads to

$$x''v^2 - \frac{v^2}{\rho}\left(1-\frac{x}{\rho}\right) = \frac{evB_0}{m} + \frac{evxg}{m} \tag{3.23}$$

$$x'' - \frac{1}{\rho}\left(1-\frac{x}{\rho}\right) = \frac{eB_0}{mv} + \frac{exg}{mv}. \tag{3.24}$$

Normalising this to the particle momentum and with $\frac{B_0}{p/e} = -\frac{1}{\rho}$ and $\frac{g}{p/e} = k$, this expression can be further simplified,

$$x'' - \frac{1}{\rho}\left(1-\frac{x}{\rho}\right) = \frac{B_0}{p/e} + \frac{xg}{p/e} \tag{3.25}$$

$$x'' \cancel{-\frac{1}{\rho}} + \frac{x}{\rho^2} = \cancel{-\frac{1}{\rho}} + kx \tag{3.26}$$

$$x'' + x\left(\frac{1}{\rho^2} - k\right) = 0. \tag{3.27}$$

For the vertical motion, this expression is even simpler as there are no dipoles acting in the vertical plane ($\frac{1}{\rho^2} = 0$). The quadrupole field also changes sign, thus resulting in

$$y'' + ky = 0. \tag{3.28}$$

3.1.3 Solution of trajectory equations

Eq. 3.27 and 3.28 can be solved, first defining a parameter K,

$$K = \begin{cases} \frac{1}{\rho^2} - k & \text{... horizontal plane} \\ k & \text{... vertical plane,} \end{cases} \tag{3.29}$$

both equations represent differential equations of harmonic oscillators with spring constant K,

$$x'' + Kx = 0. \tag{3.30}$$

This is usually solved with the ansatz

$$x(s) = a_1 \cos(\omega s) + a_2 \sin(\omega s). \tag{3.31}$$

The general solution is a linear combination of two independent cosine-like and sine-like solutions,

$$\begin{aligned} x'(s) &= -a_1 \omega \sin(\omega s) + a_2 \omega \cos(\omega s) \\ x''(s) &= -a_1 \omega^2 \cos(\omega s) - a_2 \omega^2 \sin(\omega s) = -\omega^2 x(s) \\ &\Rightarrow \quad \omega = \sqrt{K}. \end{aligned}$$

The constants are determined by boundary conditions ($s = 0$),

$$\begin{aligned} x(0) = x_0 &\quad \Rightarrow \quad a_1 = x_0 \\ x'(0) = x_0' &\quad \Rightarrow \quad a_2 = \frac{x_0'}{\sqrt{K}}. \end{aligned}$$

For a horizontally focusing quadrupole ($K > 0$), the trajectory equations take the following form

$$x(s) = x_0 \cos(\sqrt{|K|}s) + x_0' \frac{1}{\sqrt{|K|}} \sin(\sqrt{|K|}s) \tag{3.32}$$

$$x'(s) = -x_0 \sqrt{|K|} \sin(\sqrt{|K|}s) + x_0' \cos(\sqrt{|K|}s). \tag{3.33}$$

This can also be expressed in matrix formalism.

$$\begin{aligned}\begin{pmatrix} x \\ x' \end{pmatrix}_{s_1} &= M_{QF} \cdot \begin{pmatrix} x \\ x' \end{pmatrix}_{s_0} \\ \text{with } M_{QF} &= \begin{pmatrix} \cos(\sqrt{|K|}s) & \frac{1}{\sqrt{|K|}}\sin(\sqrt{|K|}s) \\ -\sqrt{|K|}\sin(\sqrt{|K|}s) & \cos(\sqrt{|K|}s) \end{pmatrix}.\end{aligned}$$

For a horizontally defocusing quadrupole ($K < 0$), the following ansatz has to be used

$$x(s) = a_1 \cosh(\omega s) + a_2 \sinh(\omega s). \tag{3.34}$$

Solving the equation in the same manner as above, the resulting matrix is

$$M_{QD} = \begin{pmatrix} \cosh(\sqrt{|K|}s) & \frac{1}{\sqrt{|K|}}\sinh(\sqrt{|K|}s) \\ \sqrt{|K|}\sinh(\sqrt{|K|}s) & \cosh(\sqrt{|K|}s) \end{pmatrix}. \tag{3.35}$$

For a drift space, where in the limit $K \to 0$, the transfer matrix results as

$$M_D = \begin{pmatrix} 1 & l \\ 0 & 1 \end{pmatrix}, \tag{3.36}$$

where l is the length of the drift space.

The transfer matrix for any type of transfer line made up of various elements is just the product of the transfer matrices of these elements, for example

$$\begin{aligned} M_{line} &= M_{QF} \cdot M_D \cdot M_{QD} \cdot M_{Bend} \cdot M_D \cdot ... \\ M(s_2|s_0) &= M(s_2|s_1) \cdot M(s_1|s_0). \end{aligned}$$

Combining all elements, the solution of the resulting differential equation can be written as

$$x(s) = C(s,s_0)x_0 + S(s,s_0)x_0' \tag{3.37}$$

$$x'(s) = C'(s,s_0)x_0 + S'(s,s_0)x_0', \tag{3.38}$$

where S and C are the sine and cosine like solutions and S' and C' are the derivatives of S and C

with respect to s. This can also be expressed in matrix notation

$$\begin{pmatrix} x \\ x' \end{pmatrix}_s = \begin{pmatrix} C & S \\ C' & S' \end{pmatrix} \cdot \begin{pmatrix} x \\ x' \end{pmatrix}_0 . \tag{3.39}$$

3.1.4 Dispersion

To calculate particle trajectories for a non-zero momentum spread, Eq. 3.24 has to be slightly altered. Still only linear fields are considered but now a small momentum error is taken into account ($\Delta p/p \neq 0$),

$$x'' - \frac{1}{\rho}\left(1 - \frac{x}{\rho}\right) = \frac{eB_0}{p_0 + \Delta p} + \frac{exg}{p_0 + \Delta p}. \tag{3.40}$$

This can then be developed for a small momentum error $\Delta p \ll p_0$,

$$\frac{1}{p_0 + \Delta p} \approx \frac{1}{p_0} - \frac{\Delta p}{{p_0}^2}, \tag{3.41}$$

$$x'' - \frac{1}{\rho} + \frac{x}{\rho^2} = \underbrace{\frac{eB_0}{p_0}}_{-\frac{1}{\rho}} - \frac{\Delta p}{{p_0}^2} eB_0 + \underbrace{\frac{exg}{p_0}}_{kx} - \underbrace{\frac{\Delta p}{{p_0}^2}}_{\approx 0} exg \tag{3.42}$$

$$x'' + \frac{x}{\rho^2} \approx \frac{\Delta p}{p_0} \underbrace{\frac{(-eB_0)}{p_0}}_{\frac{1}{\rho}} + kx = \frac{\Delta p}{p_0}\frac{1}{\rho} + kx \tag{3.43}$$

$$x'' + \frac{x}{\rho^2} - kx = \frac{\Delta p}{p_0}\frac{1}{\rho}. \tag{3.44}$$

It can be seen that a momentum spread of the beam adds a term to the right hand side of the equation of motion and leads to an inhomogeneous differential equation,

$$x'' + x\left(\frac{1}{\rho^2} - k\right) = \frac{\Delta p}{p_0}\frac{1}{\rho}. \tag{3.45}$$

The general solution can be expressed as a linear superposition of the solution of the homogenous equation and the particular solution and is of the structure $x(s) = x_h(s) + x_i(s)$ where

$$x_h(s)'' + K(s)x_h(s) = 0 \tag{3.46}$$

$$x_i(s)'' + K(s)x_i(s) = \frac{\Delta p}{p}\frac{1}{\rho}. \tag{3.47}$$

The dispersion function $D(s)$ is defined as

$$D(s) = \frac{x_i(s)}{\Delta p/p}. \tag{3.48}$$

$D(s)$ is that special orbit that an ideal particle would have for $\Delta p/p = 1$. The orbit of any particle is therefore the sum of the well known betatron motion x_β and the dispersion. As D(s) is just another orbit, it is subject to the focusing properties of the lattice,

$$\begin{aligned} x(s) &= x_\beta(s) + D(s)\frac{\Delta p}{p} && (3.49)\\ &= C(s,s_0)x_0 + S(s,s_0)x_0' + D(s)\frac{\Delta p}{p}. && (3.50) \end{aligned}$$

In matrix formalism, this can be written as

$$\begin{pmatrix} x \\ x' \end{pmatrix}_s = \begin{pmatrix} C & S \\ C' & S' \end{pmatrix} \cdot \begin{pmatrix} x \\ x' \end{pmatrix}_0 + \frac{\Delta p}{p} \begin{pmatrix} D \\ D' \end{pmatrix} \tag{3.51}$$

or expressed as a 3x3 matrix

$$\begin{pmatrix} x \\ x' \\ \frac{\Delta p}{p} \end{pmatrix}_s = \begin{pmatrix} C & S & D \\ C' & S' & D' \\ 0 & 0 & 1 \end{pmatrix} \cdot \begin{pmatrix} x \\ x' \\ \frac{\Delta p}{p} \end{pmatrix}_0 . \tag{3.52}$$

3.1.5 Beta function

As we have seen, the restoring force K is not constant but depends on the position s. An accelerator is usually constructed with repetitive modules and K is therefore a periodic function

$$K(s+L) = K(s), \tag{3.53}$$

where L is the length of a module. The resulting equation is called Hill's equation.

$$x''(s) - K(s)x(s) = 0. \tag{3.54}$$

This is a differential equation for motions with periodic focusing properties. It can be seen, that the solution to this equation will be a kind of quasi-harmonic oscillation. The amplitude and phase will depend on the position s in the ring.

The general solution to Hill's equation is of the following form

$$x(s) = \sqrt{\varepsilon}\sqrt{\beta(s)}\cos(\Psi(s)+\Phi) \tag{3.55}$$

$$x'(s) = -\frac{\sqrt{\varepsilon}}{\sqrt{\beta(s)}}[\alpha(s)\cos(\Psi(s)+\Phi)+\sin(\Psi(s)+\Phi)], \tag{3.56}$$

with $\alpha(s) = -\frac{\beta'(s)}{2}$. The integration constants ε and Φ are determined by initial conditions. The betatron amplitude function $\beta(s)$ is a periodic function given by the focusing and defocusing properties of the lattice,

$$\beta(s+L) = \beta(s). \tag{3.57}$$

Inserting Eq. 3.55 into Eq. 3.54, the phase advance $\Psi(s)$ of the oscillation between the starting point at position s in the lattice can be calculated,

$$\Psi(s) = \int_0^s \frac{ds}{\beta(s)}. \tag{3.58}$$

Using various angle sum identities, the solution to Hill's equation can be further modified,

$$\begin{aligned} x(s) &= \sqrt{\varepsilon}\sqrt{\beta(s)}(\cos\Psi(s)\cos\Phi - \sin\Psi(s)\sin\Phi)) \\ x'(s) &= -\frac{\sqrt{\varepsilon}}{\sqrt{\beta(s)}}[\alpha(s)\cos\Psi(s)\cos\Phi - \alpha(s)\sin\Psi(s)\sin\Phi + \\ &\quad + \sin\Psi(s)\cos\Phi + \cos\Psi(s)\sin\Phi]. \end{aligned}$$

Inserting the boundary conditions for $s(0) = s_0$ ($\Psi(0) = 0$),

$$\begin{aligned} \cos\Phi &= \frac{x_0}{\sqrt{\varepsilon\beta_0}} \\ \sin\Phi &= -\frac{1}{\sqrt{\varepsilon}}\left(x_0'\sqrt{\beta_0} + \frac{\alpha_0 x_0}{\sqrt{\beta_0}}\right), \end{aligned}$$

into the equations above,

$$\begin{aligned} x(s) &= \sqrt{\frac{\beta_s}{\beta_0}}(\cos\Psi_s + \alpha_0 \sin\Psi_s)x_0 + (\sqrt{\beta_s\beta_0}\sin\Psi_s)x_0' \\ x'(s) &= \frac{1}{\sqrt{\beta_s\beta_0}}[(\alpha_0-\alpha_s)\cos\Psi_s - (1+\alpha_s\alpha_0)\sin\Psi_s]x_0 + \\ &\quad + \sqrt{\frac{\beta_s}{\beta_0}}(\cos\Psi_s - \alpha_0\sin\Psi_s)x_0'. \end{aligned}$$

This can be expressed in matrix form.

$$\begin{pmatrix} x \\ x' \end{pmatrix}_s = \begin{pmatrix} \sqrt{\frac{\beta_s}{\beta_0}}(\cos\Psi_s + \alpha_0\sin\Psi_s) & (\sqrt{\beta_s\beta_0}\sin\Psi_s) \\ \frac{(\alpha_0-\alpha_s)\cos\Psi_s - (1+\alpha_s\alpha_0)\sin\Psi_s}{\sqrt{\beta_s\beta_0}} & \sqrt{\frac{\beta_s}{\beta_0}}(\cos\Psi_s - \alpha_0\sin\Psi_s) \end{pmatrix} \cdot \begin{pmatrix} x \\ x' \end{pmatrix}_0 .$$

This means that the single particle trajectories between two locations in the ring can be calculated, if α and β at these locations are known. The transfer matrix above simplifies considerably for one complete revolution,

$$M(s) = \begin{pmatrix} \cos\Psi_{turn} + \alpha_s\sin\Psi_{turn} & \beta_s\sin\Psi_{turn} \\ -\gamma_s\sin\Psi_{turn} & \cos\Psi_{turn} - \alpha_s\sin\Psi_{turn} \end{pmatrix}, \tag{3.59}$$

with $\gamma(s) = \frac{1+\alpha(s)^2}{\beta(s)}$. The phase advance per period Ψ_{turn} is defined by

$$\Psi(s) = \int_s^{L+s} \frac{ds}{\beta(s)} \tag{3.60}$$

and the phase advance per turn in units of 2π known as the machine betatron tune is defined by

$$Q = \frac{1}{2\pi}\int_s^{L+s} \frac{ds}{\beta(s)}. \tag{3.61}$$

3.1.6 Beam emittance and phase space ellipse

If Eq. 3.55 is inserted into Eq. 3.56 and solved for ε, the following expression is obtained,

$$\varepsilon = \gamma(s)x^2(s) + 2\alpha(s)x(s)x'(s) + \beta(s)x'^2(s). \tag{3.62}$$

The beam emittance ε is a constant of motion and therefore independent of position s. The above equation is a parametric representation of an ellipse in the (x,x') space. The shape and orientation of the phase space ellipse are given by the Twiss parameters α, β and γ. Fig. 3.2 shows how the dimensions and orientation of the phase ellipse are related to the Twiss parameters.

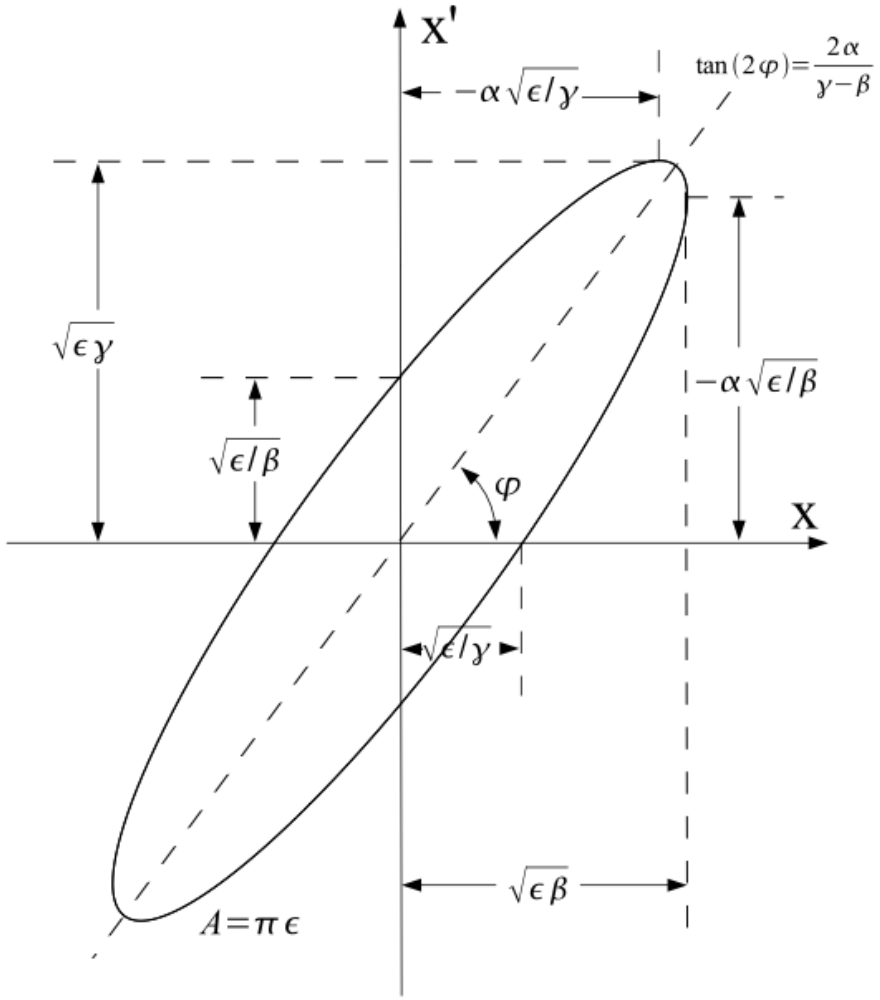

Figure 3.2: A diagram showing the relationship between the shape and orientation of the ideal phase ellipse and the Twiss parameters [16].

The extrema of the ellipse as shown in Fig. 3.2 are as follows,

$$\hat{x} = \sqrt{\varepsilon\beta} \quad \text{at} \quad x' = -\alpha\sqrt{\frac{\varepsilon}{\beta}} \tag{3.63}$$

$$\hat{x}' = \sqrt{\varepsilon\gamma} \quad \text{at} \quad x = -\alpha\sqrt{\frac{\varepsilon}{\gamma}}. \tag{3.64}$$

When dipoles are used to bend the particle trajectory in the $x-z$ plane, a non-zero dispersion

is expected and consequently a contribution to the horizontal beam size of the electron bunch. For a bunch in which the particles have a Gaussian distribution, the RMS displacement of all particles due to dispersion (Δx_D) must be combined in quadrature with the beam size contribution from the bunch beta function and bunch emittance (i.e. $\sqrt{\beta\varepsilon}$, see Eq. 3.63) to obtain the total beam size (σ_{total}) as follows,

$$\sigma_{total} = \sqrt{\beta\varepsilon + \left(D_x \frac{\delta p}{p}\right)^2}, \tag{3.65}$$

where D_x is the horizontal dispersion, and $\frac{\delta p}{p}$ is the RMS momentum spread.

In most accelerators, there are no dipole magnets used to bend the electron beam trajectory in the $y-z$ plane, so the dispersion in this plane (D_y) is usually expected to be zero.

3.1.7 Transformation of Twiss parameters

It has been shown, that between two positions in a storage ring the following relation holds.

$$\begin{pmatrix} x \\ x' \end{pmatrix}_s = M \cdot \begin{pmatrix} x \\ x' \end{pmatrix}_{s_0} \text{ with } M = \begin{pmatrix} C & S \\ C' & S' \end{pmatrix}, \tag{3.66}$$

which inverted gives

$$\begin{pmatrix} x \\ x' \end{pmatrix}_{s_0} = M^{-1} \cdot \begin{pmatrix} x \\ x' \end{pmatrix}_s \text{ with } M^{-1} = \begin{pmatrix} S' & -S \\ -C' & C \end{pmatrix}. \tag{3.67}$$

This implies

$$\begin{aligned} x_0 &= S'x - Sx' \\ x_0' &= -C'x + Cx'. \end{aligned}$$

Since the beam emittance ε is constant

$$\begin{aligned} \varepsilon &= \gamma_s x^2 + 2\alpha_s xx' + \beta_s x'^2 \\ \varepsilon &= \gamma_0 x_0^2 + 2\alpha_0 x_0 x_0' + \beta_0 x_0'^2 \\ \varepsilon &= \gamma_0 (S'x - Sx')^2 + 2\alpha_0 (S'x - Sx')(-C'x + Cx') + \beta_0 (-C'x + Cx')^2. \end{aligned}$$

Arranging for x and x' and comparing the coefficients, one gets

$$\begin{aligned}\beta(s) &= C^2\beta_0 - 2SC\alpha_0 + S^2\gamma_0 \\ \alpha(s) &= -CC'\beta_0 + (SC' + S'C)\alpha_0 - SS'\gamma_0 \\ \gamma(s) &= C'^2\beta_0 - 2S'C'\alpha_0 + S'^2\gamma_0,\end{aligned}$$

or in matrix notation

$$\begin{pmatrix}\beta \\ \alpha \\ \gamma\end{pmatrix}_s = \begin{pmatrix}C^2 & -2SC & S^2 \\ -CC' & SC' + S'C & -SS' \\ C'^2 & -2S'C' & S'^2\end{pmatrix} \cdot \begin{pmatrix}\beta_0 \\ \alpha_0 \\ \gamma_0\end{pmatrix}. \tag{3.68}$$

This means, that given the Twiss parameters α, β and γ at any point in the lattice, they can be transformed and their values can be calculated at any other point in the ring. The transfer matrix is given by the focusing properties of the lattice elements, the matrix entries are those calculated for the single particle trajectories.

3.1.8 Emittance measurement

Eq. 3.62 shows the relationship between emittance, Twiss parameters and phase ellipse. Due to Liouville's theorem, ε, the Courant and Snyder invariant for one particle anywhere in the ring, without acceleration is a constant along the beam line, but α, β and γ can change. Unlike the beam profile, the transverse momentum distribution is difficult to measure directly. Therefore, a minimum of three beam profiles have to be taken at different locations in order to get a measurement of the emittance. In this way, different parts of the transforming phase space ellipse are probed. The positions of the measurements together with the beam transformation matrices are then used to fit the results.

As established before, the beam envelope in phase space is described by an ellipse. Such an ellipse in an n-dimensional space can be written as

$$\mathbf{u}^T\sigma^{-1}\mathbf{u} = 1, \tag{3.69}$$

where σ is a symmetric matrix yet to be determined and $\mathbf{u}$ is an n-dimensional vector given by

$$\mathbf{u}^T = \begin{pmatrix} x & x' & y & y' & \tau & \delta & \dots & \dots \end{pmatrix}, \tag{3.70}$$

where x, x', y and y' are the transverse space coordinates and $\tau = t - t_0$ and $\delta = \frac{\Delta E}{E}$ are the longitudinal phase space coordinates.

The volume of an n-dimensional ellipse is defined by

$$V_n = \frac{\pi^{n/2}}{\Gamma(1+n/2)}\sqrt{\det\sigma}, \tag{3.71}$$

where Γ is the Gamma function. For $n = 2$, i.e. in the two-dimensional case, $\mathbf{u}^T = \begin{pmatrix} x, & x' \end{pmatrix}$ and $V_2 = \pi\sqrt{\det\sigma}$. Since the area of the phase space ellipse is equal to $\pi\varepsilon$, the emittance can be written as

$$\varepsilon^2 = \det\sigma. \tag{3.72}$$

Because the determinant can be used to calculate the inverse of a 2×2 matrix, σ can be expressed as

$$\sigma^{-1} = \frac{1}{\det\sigma}\begin{pmatrix} \sigma_{22} & -\sigma_{12} \\ -\sigma_{12} & \sigma_{11} \end{pmatrix} \tag{3.73}$$

$$= \frac{1}{\varepsilon^2}\begin{pmatrix} \sigma_{22} & -\sigma_{12} \\ -\sigma_{12} & \sigma_{11} \end{pmatrix}. \tag{3.74}$$

Using this expression together with the two-dimensional ellipse volume, V_2, Eq. 3.72 then becomes

$$\varepsilon^2 = \sigma_{22}x^2 - 2\sigma_{12}x'x + \sigma_{11}x'^2. \tag{3.75}$$

Compared with Eq. 3.62, the two-dimensional beam matrix can be written as

$$\sigma^{-1} = \begin{pmatrix} \sigma_{11} & \sigma_{12} \\ \sigma_{12} & \sigma_{22} \end{pmatrix} = \varepsilon\begin{pmatrix} \beta & -\alpha \\ -\alpha & \gamma \end{pmatrix}. \tag{3.76}$$

A general, n-dimensional vector $\mathbf{u}$ is transformed from point P_0 to point P_1 by a matrix $\mathcal{M}$,

such that

$$\mathbf{u}_1 = \mathcal{M}\mathbf{u}_0 \text{ and } \mathbf{u}_0 = \mathcal{M}^{-1}\mathbf{u}_1. \tag{3.77}$$

Using this relation, Eq. 3.69 can be written as

$$\begin{aligned} (\mathcal{M}^{-1}\mathbf{u}_1)^T \sigma_0{}^{-1} (\mathcal{M}^{-1}\mathbf{u}_1) &= 1 && (3.78)\\ \mathbf{u}_1{}^T (\mathcal{M}^T)^{-1} \sigma_0{}^{-1} \mathcal{M}^{-1}\mathbf{u}_1 &= 1 && (3.79)\\ \mathbf{u}_1{}^T [\mathcal{M}\sigma_0\mathcal{M}^T]^{-1}\mathbf{u}_1 &= 1. && (3.80) \end{aligned}$$

By comparing Eq. 3.80 and Eq. 3.69, it can be seen that the beam matrix transforms as

$$\sigma_1 = \mathcal{M}\sigma_0\mathcal{M}^T. \tag{3.81}$$

From Eq. 3.68 and Eq. 3.75, it follows that

$$\begin{pmatrix} \sigma_{1,11} \\ \sigma_{2,11} \\ \sigma_{3,11} \end{pmatrix} = \mathcal{M}_\sigma \begin{pmatrix} \sigma_{0,11} \\ \sigma_{0,12} \\ \sigma_{0,22} \end{pmatrix}, \tag{3.82}$$

with

$$\mathcal{M}_\sigma = \begin{pmatrix} C_1{}^2 & 2C_1S_1 & S_1{}^2 \\ C_2{}^2 & 2C_2S_2 & S_2{}^2 \\ C_3{}^2 & 2C_3S_3 & S_3{}^2 \end{pmatrix}. \tag{3.83}$$

$\sigma_{i,kj}$ are the beam matrix elements at points P_i and C_i and S_i are matrix elements of the transformation from point P_0 to P_i, which is calculated with the known beam line elements between P_0 and P_i. To get the elements of beam matrix at P_0, the following equation has to be solved

$$\begin{pmatrix} \sigma_{0,11} \\ \sigma_{0,12} \\ \sigma_{0,22} \end{pmatrix} = \mathcal{M}_\sigma{}^{-1} \begin{pmatrix} \sigma_{1,11} \\ \sigma_{2,11} \\ \sigma_{3,11} \end{pmatrix}. \tag{3.84}$$

This shows, that the elements of σ can be determined by taking beam size measurements at three different locations and with Eq. 3.72 the emittance can be calculated.

3.1.9 Beam dynamics summary

In Section 3.1, the main aspects of the necessary beam optics, the concept of emittance and the dispersion have been explained. The emittance as a function of beam size, beta function and dispersion was given in Eq. 3.65 as $\sigma_{total} = \sqrt{\beta\varepsilon + \left(D_x \frac{\delta p}{p}\right)^2}$. The following section presents the physics processes behind the laser-wire interaction process, i.e. Compton scattering and laser optics.

3.2 Compton scattering

A current and common technique for measurement of particle beam size is to use a solid wire scanner. For such a scan the wire is moved across the particle beam so that the transverse beam size can be determined from the scattered particles. However, in high luminosity machines such as CLIC, this technique cannot be used because the wire would be destroyed by the beam. Furthermore, using a wire scanner is an invasive process as it disrupts the beam and might decrease the integrated machine luminosity. Another method, using Compton scattered light, overcomes these problems and is the subject of this thesis. The Feynman diagrams for the electron Compton scattering process are shown in Fig. 3.3.

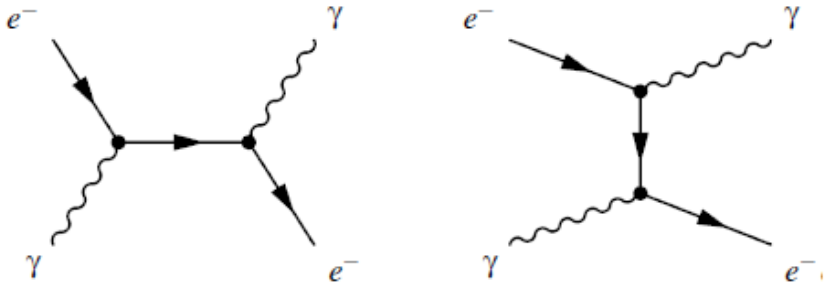

Figure 3.3: Feynman diagrams for Compton scattering (s and t channel respectively). Time goes from left to right, space vertically.

The original paper on Compton scattering can be found in [17]. A summary of the main results for inverse Compton scattering at ultra-relativistic energies is presented in [18] as follows: Considering a laser beam with a power density ρ_L and frequency ν_0, the average number of Compton photons scattered out of the laser $\langle N_\gamma \rangle$ by collision with an electron bunch containing N_e electrons is given by

$$\langle N_\gamma \rangle = \sigma_C \langle n_0 \rangle D N_e = \sigma_C \frac{\rho_L}{ch\nu_0} D N_e, \tag{3.85}$$

where $\langle n_0 \rangle$ is the average photon density, σ_C is the Compton scattering cross section, c is the speed of light and h is Planck's constant. The laser power is assumed to be uniformly distributed along its trajectory over a total distance D. The Compton cross section is related to the Thomson scattering cross section, $\sigma_T \equiv 0.665 \times 10^{28}$ m^2, by

$$\frac{\sigma_C}{\sigma_T} = \frac{3}{4}\left\{\frac{1+\varepsilon_1}{{\varepsilon_1}^3}\left[\frac{2\varepsilon_1(1+\varepsilon_1)}{(1+2\varepsilon_1)} - \ln(1+2\varepsilon_1)\right] + \frac{1}{2\varepsilon_1}\ln(1+2\varepsilon_1) - \frac{1+3\varepsilon_1}{(1+2\varepsilon_1)^2}\right\}, \tag{3.86}$$

where $\varepsilon_1 \equiv \frac{\gamma h\nu_0}{m_0 c^2}$ is the normalised photon energy in the rest frame of the electron and γ here is the Lorentz factor of the electron in the lab frame. Thomson scattering is the elastic scattering of electromagnetic radiation by a free charged particle, as described by classical electromagnetism. It is the low-energy limit of Compton scattering: the kinetic energy of the charged particle and the photon frequency are the same before and after the scattering. This limit is valid as long as the photon energy is much less than the mass energy of the particle.

The energy spectrum of the scattered photons is given by

$$\frac{d\sigma/\sigma_T}{d\omega} = \frac{3}{8\varepsilon_1}F(\varepsilon_1,\omega), \tag{3.87}$$

where $\omega \equiv \frac{h\nu_\gamma}{E}$ is the energy of the outgoing photon normalised to the electron energy E, The parameter F is given by

$$F(\varepsilon_1,\omega) = \frac{1}{1-\omega} + 1 - \omega + \left[\frac{\omega}{\varepsilon_1(1-\omega)}\right]^2 - \frac{2\omega}{\varepsilon_1(1-\omega)}. \tag{3.88}$$

The maximum photon energy is given by $h\nu_{max} = \frac{2E\varepsilon_1}{1+2\varepsilon_1}$. The photons are generally emitted in a cone whose half-angle is a few times the critical angle $\alpha_c = \frac{\sqrt{1+2\varepsilon_1}}{\gamma}$.

Fig. 3.4 shows the normalised cross-section $\frac{\sigma_C}{\sigma_T}$ plotted versus the scattered photon energy for both Laser-wire setups considered in this theses.

3.2.1 Introduction to Gaussian wave optics

This section is a summary of the concepts presented in [19]. Electromagnetic fields in free space are described by the scalar wave equation

$$\left[\nabla^2 + k^2\right]\tilde{E}(x,y,z) = 0, \tag{3.89}$$

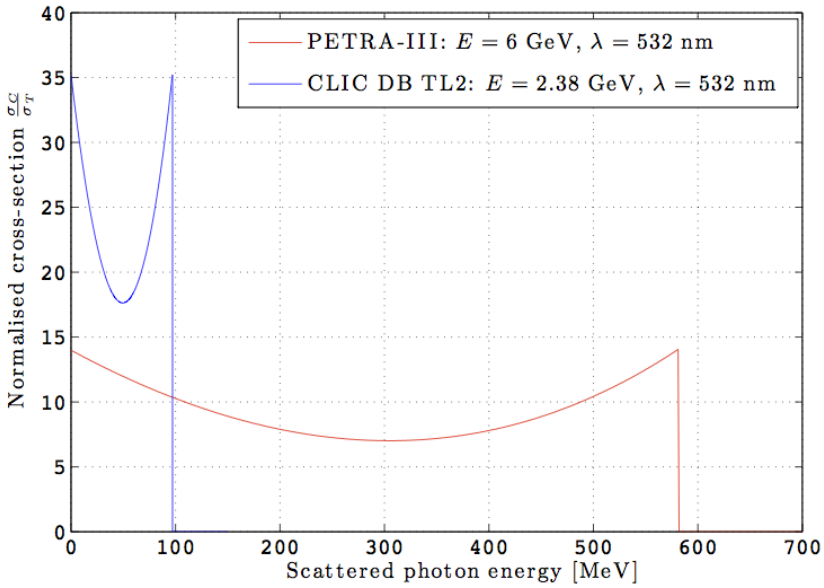

Figure 3.4: Normalised cross-section $\frac{\sigma_C}{\sigma_T}$ plotted versus the scattered photon energy for the LW at PETRA-III and a possible LW at CLIC DB TL2.

where $\tilde{E}(x,y,z)$ is the phasor electric field amplitude of a temporally sinusoidal distribution.

Taking the propagation direction of the laser beam to be the z direction, the primary spatial dependence is e^{-ikz} with a wave number $k = \frac{2\pi}{\lambda}$, where λ is the wavelength. If the beam is considered to be collimated, the transverse beam profile varies much more slowly than the plane-wave variation in the z direction. Therefore, the phasor amplitude can be expressed as

$$\tilde{E}(x,y,z) \equiv \tilde{u}(x,y,z)e^{-ikz}. \tag{3.90}$$

With this, the scalar wave equation in Eq. 3.89 can be written as

$$\frac{\partial^2\tilde{u}}{\partial x^2} + \frac{\partial^2\tilde{u}}{\partial y^2} + \frac{\partial^2\tilde{u}}{\partial z^2} - 2ik\frac{\partial\tilde{u}}{\partial z} = 0. \tag{3.91}$$

After factoring out the e^{-ikz} dependence, the residual z dependence of $\tilde{u}(x,y,z)$ caused by diffraction effects varies slowly compared to the transverse variations due to the finite width of the beam. Therefore, the term $\frac{\partial^2\tilde{u}}{\partial z^2}$ can be neglected. This so-called paraxial approximation results in the paraxial wave equation which can be expressed more generally as

$$\nabla_t{}^2\tilde{u}(\mathbf{s},z) - 2ik\frac{\partial\tilde{u}(\mathbf{s},z)}{\partial z} = 0, \tag{3.92}$$

where ${\nabla_t}^2$ is the Laplacian operating on the transverse coordinates $\mathbf{s} \equiv (x,y)$ or $\mathbf{s} \equiv (r,\theta)$ in the transverse plane.

An electromagnetic field $\tilde{E}(\mathbf{r},\mathbf{r}_0)$ at point $\mathbf{r}$ caused by a point source at $\mathbf{r}_0$ is represented by a uniform spherical wave diverging from $\mathbf{r}_0$,

$$\tilde{E}(\mathbf{r},\mathbf{r}_0) = \frac{\exp[-ik\rho(\mathbf{r},\mathbf{r}_0)]}{\rho(\mathbf{r},\mathbf{r}_0)}, \tag{3.93}$$

where $\rho(\mathbf{r},\mathbf{r}_0)$ is the distance from the source point $(\mathbf{s}_0,z_0)$ to the observation point $(\mathbf{s},z)$,

$$\rho(\mathbf{r},\mathbf{r}_0) = \sqrt{(x-x_0)^2+(y-y_0)^2+(z-z_0)^2}. \tag{3.94}$$

Assuming a source point not too far away from the z axis and for values of x and y farther along but also close to the z axis, $\rho(\mathbf{r},\mathbf{r}_0)$ can be expanded into

$$\rho(\mathbf{r},\mathbf{r}_0) = (z-z_0) + \frac{(x-x_0)^2+(y-y_0)^2}{2(z-z_0)} + \ldots. \tag{3.95}$$

Neglecting the higher-order terms, this is called the Fresnel approximation. Eq. 3.93 then simplifies to

$$\tilde{E}(x,y,z) = \frac{1}{z-z_0}\exp\left[-ik(z-z_0) - ik\frac{(x-x_0)^2+(y-y_0)^2}{2(z-z_0)}\right] \tag{3.96}$$

and

$$\begin{aligned}
\tilde{u}(x,y,z) &= \frac{1}{z-z_0}\exp\left[-ik\frac{(x-x_0)^2+(y-y_0)^2}{2(z-z_0)}\right] &(3.97)\\
&= \frac{1}{R(z)}\exp\left[-ik\frac{(x-x_0)^2+(y-y_0)^2}{2R(z)}\right] &(3.98)\\
&= \frac{1}{R(z)}\exp\left[-i\phi(x,y,z)\right], &(3.99)
\end{aligned}$$

where $R(z) = z - z_0$ is the radius of curvature of the spherical wave at the z plane and phase $\phi(x,y,z)$ is defined as

$$\begin{aligned}
\phi(x,y,z) &\equiv k\frac{(x-x_0)^2+(y-y_0)^2}{2R(z)} &(3.100)\\
&= \frac{\pi}{\lambda}\frac{(x-x_0)^2+(y-y_0)^2}{R(z)}. &(3.101)
\end{aligned}$$

The wave described in Eq. 3.97 is a non-physical one as its amplitude does not decrease with increasing distance from the z axis. Since real beams have a finite transversal extent, the real radius of curvature is substituted by a complex one, $\tilde{q}(z) = \tilde{q}_0 + z - z_0$, thus giving

$$\tilde{u}(x,y,z) = \frac{1}{z - z_0 + \tilde{q}_0} \exp\left[-ik\frac{x^2+y^2}{2(z-z_0+\tilde{q}_0)}\right] \tag{3.102}$$

$$= \frac{1}{\tilde{q}(z)} \exp\left[-ik\frac{x^2+y^2}{2\tilde{q}(z)}\right]. \tag{3.103}$$

Separating the real and imaginary parts of the inverse of the complex radius of curvature, $\frac{1}{\tilde{q}(z)} \equiv \frac{1}{\tilde{q}_r(z)} - i\frac{1}{\tilde{q}_i(z)}$, the spherical wave can be written as

$$\tilde{u}(x,y,z) = \frac{1}{\tilde{q}(z)} \exp\left[-ik\frac{x^2+y^2}{2\tilde{q}_r(z)} - k\frac{x^2+y^2}{2\tilde{q}_i(z)}\right] \tag{3.104}$$

$$= \frac{1}{\tilde{q}(z)} \exp\left[-ik\frac{x^2+y^2}{2R(z)} - \frac{x^2+y^2}{W^2(z)}\right]. \tag{3.105}$$

This beam now has a transverse variation which is purely real resulting in a Gaussian transverse amplitude profile. In standard notation, $R(z)$ is the radius of curvature of the beam's wavefronts and $W(z)$ is the radius at which the wave intensity drops to $1/e^2$ of its axial value. The complex radius of curvature $\tilde{q}(z)$ is related to the spot size and the radius of curvature at any plane z by

$$\frac{1}{\tilde{q}(z)} \equiv \frac{1}{R(z)} - i\frac{\lambda}{\pi W^2(z)} \tag{3.106}$$

and the fundamental propagation law for all Gaussian beams in free space is determined by

$$\tilde{q}(z) = \tilde{q}_0 + z - z_0. \tag{3.107}$$

Gaussian beams are just one possible solution to the paraxial wave equation. Various other sets of orthogonal solutions are used for modelling laser beams. In the general case, if a complete basis set of solutions is chosen, any real laser beam can be described as a superposition of solutions from this set. Laser-wires and many other other applications require an almost single-mode Gaussian laser beam, because they are well defined and provide a high spatial density. However, in real laser beams other modes are most likely also present which reduces the quality of the laser and therefore the performance of the laser-wire system as this limits the minimum

achievable spot size and, consequently, the minimum measurable transverse electron beam size.

The initial value $\tilde{q}_0$ in Eq. 3.107 is defined as

$$\tilde{q}_0 = i\frac{\pi {W_0}^2}{\lambda} = iz_R, \tag{3.108}$$

where $W_0 = W(0)$ is the spot size at the beam waist. All important parameters of a Gaussian beam can then be expressed in terms of W_0 and the ratio z/z_R by

$$W(z) = W_0\sqrt{1+\left(\frac{z}{z_R}\right)^2}, \tag{3.109}$$

$$R(z) = z+\frac{{z_R}^2}{z}, \tag{3.110}$$

$$\psi(z) = \tan^{-1}\left(\frac{z}{z_R}\right). \tag{3.111}$$

Real laser beams are not purely in single transverse mode but contain additional modes. The propagation of a real beam is therefore not only dependent on W_0 but also on the so-called beam quality factor M^2. The value of M^2 is ≥ 1 for any arbitrary beam profile, with the limit of $M^2 = 1$ occurring only for a single-mode lowest-order Gaussian beam. The M^2 value represents a measure of "how many times diffraction limited" the real beam is [20]. Using this concept, Eq. 3.109, and subsequently all other equations, can be generalised in the way that the wavelength λ is replaced by $M^2\lambda$ to account for the laser beam quality,

$$W(z) = W_0\sqrt{1+\left(\frac{(z-z_0)M^2\lambda}{\pi {W_0}^2}\right)^2}. \tag{3.112}$$

The beam spot size $W(z)$ increases by a factor $\sqrt{2}$ between $z = z_0$ and $z = z_0 + z_R$, this distance z_R is called the Rayleigh range.

Far from focus, the beam size expands linearly. The far-field beam angle is defined by using the $1/e$ or 86% criterion, so that the far field half-angular spread is defined by the width of the transverse beam profile where the amplitude falls to the $1/e$ point for the maximum amplitude. This can be written as

$$\theta_{1/e} = \lim_{z\to\infty}\frac{W(z)}{z} = \frac{\lambda}{\pi W_0}. \tag{3.113}$$

For distances far from the focus, i.e. $z \gg z_R$, Eq. 3.109 simplifies to

$$W(z) \approx \frac{W_0 z}{z_R} = \frac{\lambda z}{\pi W_0}, \tag{3.114}$$

which gives the simple relation

$$W_0 \times W(z) \approx \frac{\lambda z}{\pi}. \tag{3.115}$$

For a Gaussian spot size at a focusing lens at $z = f$, where f is the focal length of the lens, this expression turns into

$$W_0 \times W(f) \approx \frac{\lambda f}{\pi}. \tag{3.116}$$

This relation shows that in order to minimise the focus spot size, the incident Gaussian beam should fill the aperture of the focusing lens to the largest extent possible without overfilling the lens as this causes diffraction effects.

3.2.2 Laser-wire Compton rates

The Compton cross section decreases with increasing electron beam energy. For an electron beam with energy E_b and a laser with photon energy $k = \frac{hc}{\lambda}$ and $\omega = \frac{kE_b}{m_e{}^2c^4}$, the Compton cross section is given by Eq. 3.86 [21]. The number of produced Compton photons, $N(\Delta_x, \Delta_y)$, is a function of relative horizontal and vertical offsets, Δ_x and Δ_y, and will be proportional to the overlap between the electron beam and the laser beam resulting in a three-dimensional overlap integral, $\varepsilon(\Delta_x, \Delta_y)$,

$$N(\Delta_x, \Delta_y) = N_0 \varepsilon(\Delta_x, \Delta_y), \tag{3.117}$$

where

$$N_0 = \frac{P_l N_e \lambda f(\omega) \sigma_T}{hc^2}, \tag{3.118}$$

in which P_l is the instantaneous laser power at the laser-wire IP, N_e is the number of electrons in the bunch, and $f(\omega)$ is the ratio of cross sections for Compton and Thomson scattering, $\frac{\sigma_C}{\sigma_T}$, in Eq. 3.86.

The Rayleigh range, x_R, is a longitudinal quantity defined as the distance from the waist of the laser profile along the laser propagation direction to the point at which the transversal laser beam width, σ, becomes $\sqrt{2}$ times the waist size, σ_0. In the M^2 model of laser propagation,

where M^2 is the quality factor for the laser, x_R is given by

$$x_R = M^2 \frac{4\pi\sigma_0}{\lambda}, \tag{3.119}$$

where $\sigma_0 = \lambda f_\#$ is the diffraction limited beam size at the laser waist. An ideal single TM_{00} mode laser would have $M^2 = 1$. The presence of other modes increases the quality factor, which effectively increases the wavelength $\lambda \to M^2\lambda$. The waist size is also limited by the f-number of the optics, $f_\# = D_l/F$, where D_l is the diameter of the lens and F is its focal length. From

$$\sigma_l = M^2\sigma_0 = M^2\lambda f_\# \tag{3.120}$$

can be seen, that the smallest possible waist size is achieved with $M^2 = 1$ and $f_\# = 1$.

For the TM_{00} laser mode, the transverse overlap integral is

$$\varepsilon(\Delta_x, \Delta_y) = \int \frac{dxdyI_lI_e}{(2\pi)^{3/2}\sigma_{ex}\sigma_{ey}\sigma_l\sqrt{f_R(x-\Delta_x)}} \exp\left[-\frac{x^2}{2{\sigma_{ex}}^2} - \frac{y^2}{2{\sigma_{ey}}^2} - \frac{(y-\Delta_y)^2}{2{\sigma_l}^2 f_R(x-\Delta_x)}\right] \tag{3.121}$$

where

$$f_R(x) = 1 + \left(\frac{x}{x_R}\right)^2, \tag{3.122}$$

where x_R is the Rayleigh range. Performing the y-integral in Eq. 3.121 gives

$$\varepsilon(\Delta_x, \Delta_y) = \frac{I_lI_e}{2\pi\sigma_{ex}} \int \frac{dx}{\sigma_s(x,\Delta_x)} \exp\left[-\frac{x^2}{2{\sigma_{ex}}^2} - \frac{{\Delta_y}^2}{2{\sigma_s}^2(x,\Delta_x)}\right], \tag{3.123}$$

where

$$\sigma_s(x,\Delta_x) = \sqrt{{\sigma_{ey}}^2 + {\sigma_l}^2 f_R(x-\Delta_x)}. \tag{3.124}$$

Approximating an infinite Rayleigh range, $f_R(x-\Delta_x) \approx 1$ and the width of the vertical Compton scattering profile reduces to the more familiar form

$$\sigma_{sy} = \sqrt{{\sigma_{ey}}^2 + {\sigma_{ly}}^2} \tag{3.125}$$

and the overlap integral becomes

$$\varepsilon(\Delta_y) = \frac{1}{\sqrt{2\pi}\sigma_{sy}} \exp\left[-\frac{{\Delta_y}^2}{2{\sigma_{sy}}^2}\right]. \tag{3.126}$$

In case the Rayleigh range is small or comparable to the horizontal size of the electron beam, then the general form in Eq. 3.124 must be used.

3.3 Synchrotron radiation

Synchrotron radiation (SR) is the main source of background for the ATF laser-wire [16, 22] and will also be for the CLIC Drive-Beam Transfer Line TL2. It is the reason for using a Cerenkov detector to detect higher-energy Compton scattered photons, as this detector serves as a threshold under which low-energy synchrotron photons are not detected (see Section 6.2).

SR from a bending magnet is also a versatile tool for beam size measurement in its own right. A dedicated diagnostics beam-line was constructed at PETRA-III to image the beam profile via bending magnet SR using two systems: a pinhole optics for normal operation and an optical system involving a high resolution compound refractive lens (CRL) (see Section 4.1.2).

3.3.1 Emission of radiation

This section is a summary of the contents presented in [15] and [23]. When charged particles are accelerated radially, they emit radiation due to their electric fields being rearranged. This field perturbation is called synchrotron radiation (SR). In storage rings, particles pass through through many bending magnets to be kept on orbit and thus produce large amounts of SR.

The power radiated by a relativistic particle circulating in a synchrotron is

$$P_\gamma = \frac{1}{6\pi\varepsilon_0}\frac{e^2 c}{\rho^2}\cdot\gamma^4 = \frac{2}{3}\frac{r_e c}{(m_0c^2)^3}\frac{E^4}{\rho^2}, \tag{3.127}$$

where E is the energy of the particle, ρ is the bending radius of the particle trajectory in the magnetic field, $r_e = \frac{e^2}{4\pi\varepsilon_0 m_0 c^2}$ is the classical electron radius, m_0 is the mass of the particle, c is the speed of light, e is the elementary charge, ε_0 is the electric constant and $\gamma = \frac{E}{m_0c^2}$ is the Lorentz factor.

In theory, this applies to protons as well as electrons. However, the the mass of the electron is about 2000 times smaller than the mass of the proton and, therefore, for the same energy it has a γ that is 2000 times larger. Since the emission of SR depends on γ^4, the main reason to build a linear electron positron collider, rather than a circular machine, is the large amounts of lost energy due to SR.

When using the radiation constant $C_\gamma = \frac{4\pi}{3}\frac{r_e}{(m_0c^2)^3} = 8.8575 \times 10^{-5}$ m/GeV^3, Eq. 3.127 can be expressed in more practical units,

$$P_\gamma \text{ [GeV/s]} = \frac{cC_\gamma}{2\pi}\frac{E^4}{\rho^2}. \tag{3.128}$$

The energy radiated by a particle on each turn can be calculated by multiplying P_γ with the revolution time ($2\pi R/\beta c$),

$$\Delta E = C_\gamma \frac{E^4}{\rho}. \tag{3.129}$$

The Large Electron Positron Collider (LEP) at CERN had $\rho = 3100$ m and $E = 104.4$ GeV in 2000 [24]. Therefore the particle energy lost per turn was 3.4 GeV or roughly 3%. Since the available accelerating power to keep the beams in orbit was limited, the energy could not be further increased. For comparison, the same fractional energy loss at 500 GeV (the CLIC energy) would result in an average dipole bending radius of 341 km. The actual LEP radius was 4 km, about 1.3 times the dipole bending radius. With the assumption that the actual radius scales with the bending radius, the radius for a 500 GeV circular machine would be 443 km which is more than 100 times the LEP radius. It can be seen that in this energy regime, linear acceleration of particles is to be preferred.

However, SR is still a source of background in linear colliders and needs to be kept reasonably small compared to the Compton scattered photons from the laser-wire. To solve this problem, the difference in the spectra of the SR and the Compton photons can be used.

3.3.2 Spectrum of frequencies

SR is emitted over a broad spectrum of frequencies. However, this spectrum falls off rapidly above the critical energy, which is defined as

$$\varepsilon_c = \hbar\omega_c = \frac{3}{2}\frac{\hbar c\gamma^3}{\rho} = \frac{\hbar C_c E^3}{\rho}, \tag{3.130}$$

where $\hbar$ is the reduced Planck constant ($\frac{h}{2\pi}$), ρ is the bending radius of the particle trajectory in the magnetic field, γ is the Lorentz factor, E is the particle energy and $C_c = \frac{3c}{2(m_0c^2)^3)} = 3.37 \times 10^{18}$ m$/$(s$\cdot$GeV^3) for electrons. This critical energy is used as a mathematical scaling parameter.

It can be written in terms of keV as

$$\varepsilon_c\ [\text{keV}] = 2.218 \frac{E^3\ [\text{GeV}]}{\rho\ [\text{m}]} = 0.665\ E^2[\text{GeV}]\ B[\text{T}]. \tag{3.131}$$

The spectral density for $\frac{\omega}{\omega_c} \gg 1$ can be approximated by

$$\frac{dP}{d\omega} \approx \frac{9\sqrt{3}}{8\sqrt{2\pi}} \sqrt{\frac{\omega}{\omega_c}} e^{-\omega/\omega_c} \frac{P_\gamma}{\omega_c} = 0.78 \sqrt{\frac{\omega}{\omega_c}} e^{-\omega/\omega_c} \frac{P_\gamma}{\omega_c}. \tag{3.132}$$

The number of SR photons emitted in a dipole per unit length and per beam particle is

$$\frac{dN_{SR}}{ds} = \frac{5\alpha}{2\sqrt{3}} \frac{\gamma}{\rho}, \tag{3.133}$$

where γ denotes the Lorentz factor and α the fine-structure constant.

3.3.3 Expected backgrounds

At PETRA-III (see Section 4.1), the dipoles have a bending angle of $\alpha = 1.61^\circ$ and a length of $L = 5.378$ m. This leads to a bending radius of $\rho = 191.7$ m. With a beam energy of 6 GeV, the critical energy can be calculated with Eq. 3.130 to $\varepsilon_c = 2.5$ keV. With a bunch population of $N_{e^+} = 12 \cdot 10^{10}$, the total number of photons emitted in such a dipole is $N_{SR,tot} = 4.1 \cdot 10^{11}$.

At the CLIC Drive Beam transfer line TL2, the dipole which is considered for the laser-wire system has a bending angle of $\alpha = 0.26^\circ$ and a length of $L = 2.0057$ m. This leads to a bending radius of $\rho = 7.7$ m. With a beam energy of 2.38 GeV, the critical energy can results in $\varepsilon_c = 3.9$ keV. With a bunch population of $N_{e^-} = 5.25 \cdot 10^{10}$, the total number of photons emitted in this a dipole is $N_{SR,tot} = 6.7 \cdot 10^{11}$.

Chapter 4

The PETRA-III Laser-Wire

4.1 The PETRA-III Accelerator Facility

PETRA stands for positron-electron tandem-ring facility (Positron-Elektron-Tandem-Ring-Anlage) and was built between 1975 and 1978. At the time of its construction it was the biggest storage ring of its kind with a circumference of 2.304 km and still is, after HERA, DESY's second largest synchrotron. It is a circular collider with eight arc sections. The schematic layout of PETRA II is given in Fig. 4.1. After each arc section follows either a long or a short straight section and these alternate resulting in PETRA's four-fold symmetry. Each short straight section contains one interaction point. The long straight sections are equipped with RF cavities to maintain the particle beam energies. PETRA could accelerate electrons and positrons up to 15 GeV.

The original purpose of PETRA was to do research on elementary particles. Four experimental collaborations called TASSO, JADE, PLUTO and MARK J, respectively, established themselves on PETRA. In 1979, planar three-jet events were observed, which was the first direct evidence to confirm the existence of gluons.

In 1990, the facility was recommissioned under the name PETRA-II as a pre-accelerator for protons and electrons/positrons for the new particle accelerator HERA (hadron-electron ring accelerator). In March 1995, PETRA-II was equipped with two undulator beam-lines to producing a synchrotron radiation spectral energy range from 15 keV to 500 keV. Since then PETRA serves HASYLAB (Hamburg synchrotron radiation laboratory) as a source of high-energy synchrotron radiation and for this purpose possesses three test experimental areas. In July 2007, HERA was decommissioned and PETRA-II stopped being used as its pre-accelerator. After that, PETRA-II

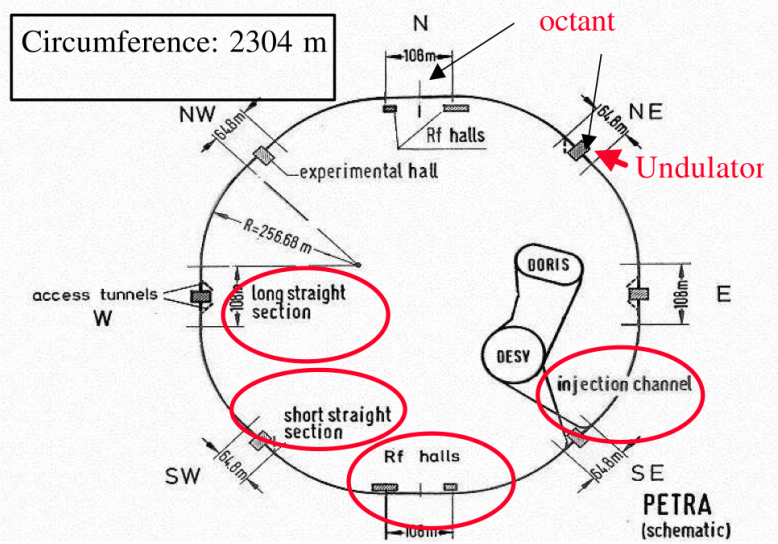

Figure 4.1: Overview of PETRA storage ring [25].

was upgraded to PETRA-III. One-eighth of the ring was rebuilt and equipped with 14 undulators. In November 2009, PETRA-III started running with 14 experimental stations.

4.1.1 The storage ring

The upgrade of the PETRA II storage ring to PETRA III required the total rebuilding of one octant of the ring, about 300 m out of the total 2.3 km, to provide the electron-beam optics for nine straight sections, each offering space for one 5 m long or two 2 m long undulators. 14 experimental stations with independently tunable insertion devices are available. The positron energy is 6 GeV, with a beam current of 100 mA. The nominal parameters for PETRA-III are given in Table 4.1

PETRA-III operates in so-called top-up mode, which means that the current in the storage ring is kept constant to within 1% via frequent injections of new particles. The time between top-ups can be as short as 70 s for a 40-bunch filling pattern. PETRA-III has a horizontal emittance of 1 nm·rad. This was achieved by installing 20 damping wigglers, each with a length of 4 m, in two of the long straight sections of the ring. The power loss of the beam through synchrotron radiation in these wigglers damps the horizontal motion of the stored particles and thus reduces the horizontal momentum spread of the photon beams.

Table 4.1: PETRA-III machine parameters [26]

Parameter	Symbol	Value	Unit
Positron energy	E	6.0	GeV
RF Frequency	f_{RF}	499.562	MHz
Revolution frequency	f_{rev}	130.1	kHz
Revolution Time	τ_{rev}	7.685	µs
No. of buckets		3840	
No. of bunches / fill	N_{fill}	960 and 40	
Bunch separation	Δt_b	8 and 192	ns
Positron beam current	I_B	100 (top-up mode)	mA
Positron beam charge	Q_B	769	nC
No. of positrons		4.8	10^{12}
No. of positrons / bunch	N_{e^+}	0.5 and 12	10^{10}
Horizontal positron beam emittance		1	nm·rad (RMS)
Coupling factor		1	%
Vertical positron beam emittance		0.01	nm·rad (RMS)
Positron beam energy spread		0.1	% (RMS)

4.1.2 Diagnostics Beam-Line [27]

In addition to the laser-wire, a second emittance measurement system was installed at PETRA-III. A dedicated diagnostics beam-line was constructed to image the beam profile using synchrotron radiation. Synchrotron radiation (SR) from a bending magnet is a versatile tool for beam size measurements. In order to resolve beam profiles of a few tens of µm, at PETRA-III imaging is performed in the x-ray region at a photon energy of 20 keV. The diagnostics beam-line uses two interchangeable x-ray optical systems: a pinhole optics for normal operation and an optical system involving a high resolution compound refractive lens (CRL). The measurements of these two systems were compared with the laser-wire and the results are presented in Section 5.2.

The diagnostics beam-line is located at the end of the new PETRA-III experimental hall. With a total length of about 15 m, the whole beam-line is situated inside the accelerator tunnel. SR with a critical energy of 20.9 keV is produced in a long standard dipole with a length of about 1 m. According to the beam optical design parameters, the electron beam has an RMS size of $\sigma_x = 42.5$ µm and $\sigma_y = 18.5$ µm at the source point of the beam-line.

For the design current of 100 mA the total emitted SR power is 3.5 kW. A water cooled absorber located 5.1 m after the source point reduces the power entering the diagnostics beam-line to about 15 W. The x-ray part of the emitted radiation is used to image the beam spot onto a

CCD via two interchangeable x-ray optical systems, a pinhole optic and a high resolution CRL optic. A sketch of the diagnostics beam-line can be found in Fig. 4.2. The x-ray optics are housed in a small vacuum chamber located 6.1 m after the source point. They are mounted onto motorised stages, allowing to exchange the optical systems and to align the optics with respect to the beam axis in three degrees of freedom: two linear translations perpendicular to the beam axis and the rotation around the vertical axis. The whole system is fixed onto a granite beam-line girder together with diagnostic screens for photon beam steering.

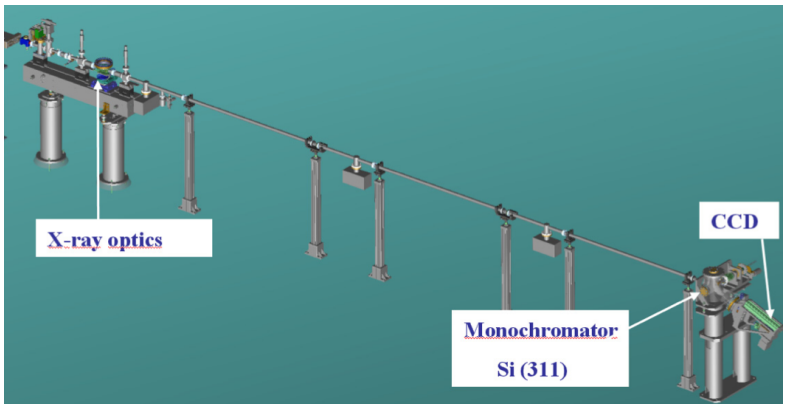

Figure 4.2: Overview of the diagnostics beam-line starting from the entrance absorber [27].

Fig. 4.3 shows a view of the open housing for the x-ray optics together with the optical systems and absorbers. The CRL system consists of 31 individual beryllium lenses. Each single lens is centred inside a ring made of hard metal alloy with a thickness of 1.6 mm. The lenses are stacked behind each other on a high-precision V-profile shaft in order to align their optical axes along one common optical axis. Each lens surface has the shape of a concave rotational paraboloid with an apex radius of curvature of 200 µm and a geometrical aperture of 0.9 mm. For adapting the SR spot size to the lens aperture and also to minimise the heat load on the lenses, an additional conical copper absorber with 0.8 mm free aperture is placed just in front of the lens stack onto the profile shaft. The focal length of the CRL system is 3.72 m with a diffraction limit in the image plane calculated to be 0.3 µm (RMS).

The pinhole is incorporated in the exit absorber. It consists of a 0.5 mm thick tungsten plate with a bore hole of 20 µm diameter. The pinhole diameter is a result of an optimisation using numerical near field calculations. The resolution of the pinhole is $\Delta\sigma_x = 20$ µm and $\Delta\sigma_y = 16$ µm respectively.

The electron beam is imaged either with non-monochromatised SR in the straight direction

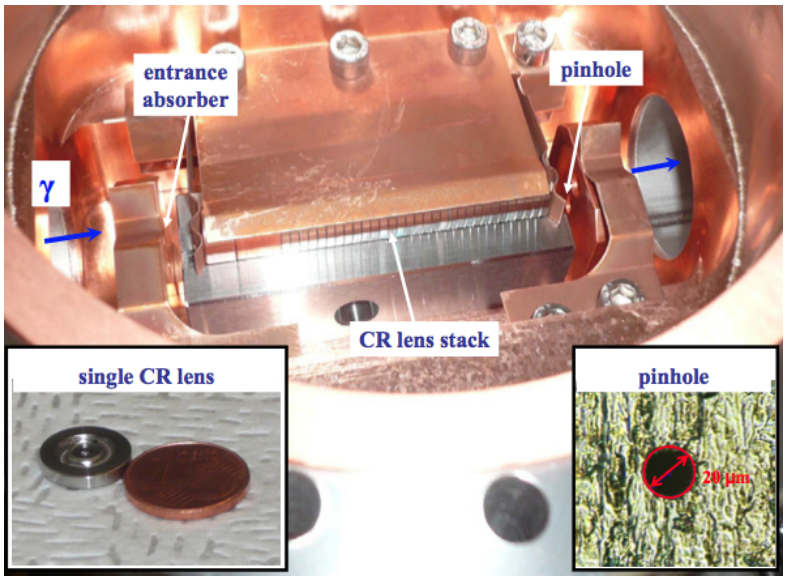

Figure 4.3: Vacuum chamber for the x-ray optics. The inserts show a single refractive lens and a photo of the pinhole respectively [27].

or with monochromatised 20 keV SR deflected out of the orbit plane. Both detection systems consist of a LYSO scintillator converting the incoming xrays into visible light, a 12 bit GigE CCD camera with 4.65×4.65 µm^2 pixel size, and a precision telecentric objective with optical magnification of 2 imaging the scintillation light spot onto the CCD chip. The x-ray optical system has a magnification factor of about 1.55. While it is unlikely that there is an error in the x-ray magnification, a misunderstanding of the optical magnification could introduce a factor of 2 to 3. However, this is unlikely with a well calibrated expander. Also, it is believed it is a fixed magnification. The LYSO crystal typically causes the optical transfer function to blur which would also increase the measured beam size. Possible chromatic effects without the monochromator could blur the x-ray image as well and would result in a larger beam size. Furthermore, multiple peaks associated with the monochromator (see [27]) would make the beam size appear larger. In general the systematic effects reported in [27] are probably small and typically overestimate the beam size.

4.2 The Laser-Wire Experiment

4.2.1 Principle of operation

Laser-wire (LW) beam profile monitors will be the key beam diagnostic instruments for future very high energy/intensity particle accelerators to replace the use of traditional profiling techniques such as wire scanners or screens. LWs can be employed in synchrotron light sources [28], linear electron-positron colliders [21], and most recently H^- ion accelerators [29].

The principle of operation is to scan a finely focused laser beam across an electron beam. The resulting overlap of the two beams is schematically shown in Fig. 4.4. The photons in the laser beam scatter from the electrons in the electron beam through Compton scattering ($e^-\gamma \rightarrow e_C{}^-\gamma_C$). At maximum beam overlap, the number of Compton scattered particles for an electron bunch population of $2\cdot 10^{10}$ and a pulsed laser with peak power of 10 MW and a wavelength of 532 nm is $N_{det} = 4.72\cdot 10^4[\mu m]\times \eta_{det}/\sigma_c$ [21]. In this expression, η_{det} is the detector efficiency and σ_c is the transverse size of the convolution between the laser and electron beams. In the approximation of infinite Rayleigh range ($z_r \gg \sigma_{e,x}$), this is given by $\sigma_c = \sqrt{\sigma_{e,y}{}^2 + \sigma_{l,y}{}^2}$ (see Eq. 3.125), where $\sigma_{e,x/y}$ are the RMS horizontal and vertical electron beam sizes and $\sigma_{l,y}$ is the RMS vertical laser beam size. Since the scattering rate is proportional to the spatial overlap of the particle distributions, through knowledge of σ_l at the laser-wire interaction point and the scattering rate as a function of relative transverse displacement, σ_e can be determined.

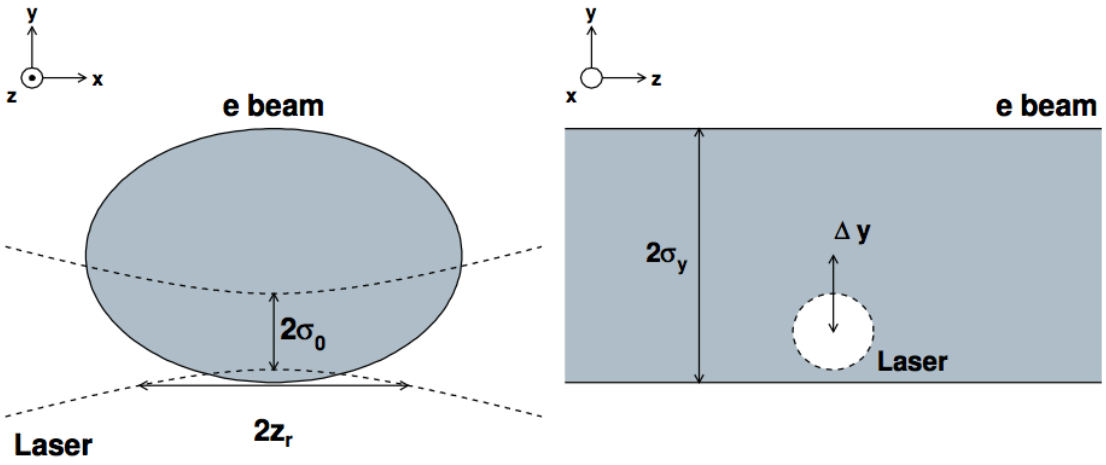

Figure 4.4: A diagram of the overlap of the laser and electron beams. On the left, the electron beam is shown travelling into the page and the laser beam travels from left to right. σ_y here is the vertical electron beam size. Δ_y is the displacement in y from the maximum overlap position. The dotted lines are the edges of a Gaussian laser beam converging to a waist of size σ_0 and with Rayleigh range z_r (Eq. 3.112) [16].

In Fig. 4.5, the location of the laser-wire at PETRA III is shown. Fig. 4.6 presents a plan overview of the LW experimental layout. It illustrates the major components of the LW system: high power laser, optical scanning systems, beam position monitor (BPM) and Compton calorimeter.

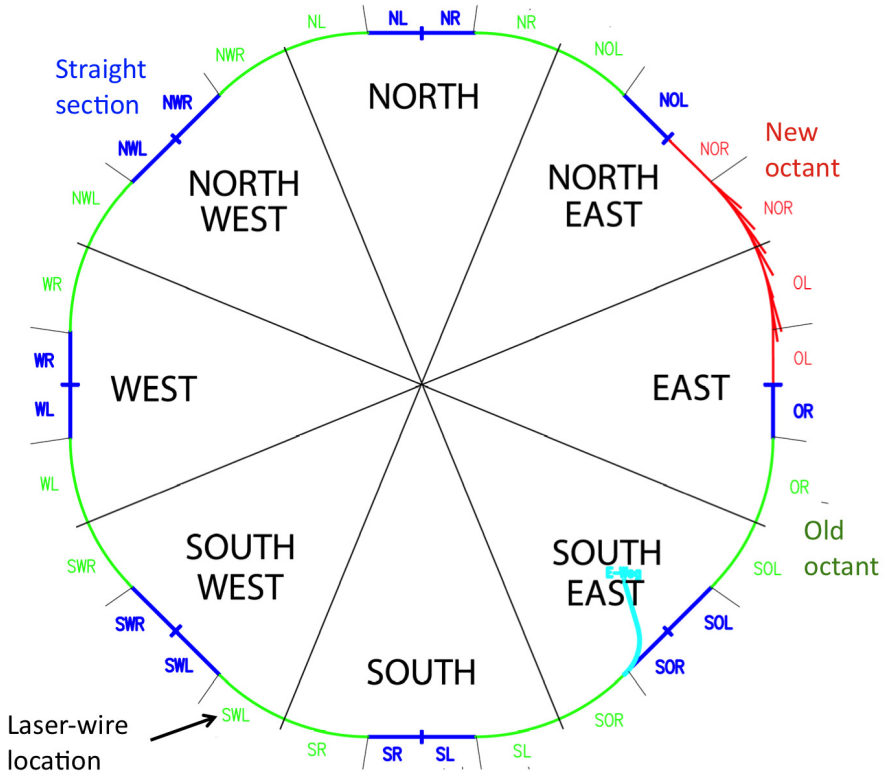

Figure 4.5: LW location at the PETRA-III facility.

High-energy green ($\lambda = 532$ nm) laser pulses, which are synchronised with the PETRA bunch clock, are transported into the tunnel and onto the optical breadboard via a series of mirrors. The laser light is then steered onto the final focus lens using a scanning mirror and collided with the positron bunches within a custom built vacuum vessel with optical view ports. The Compton photons produced in the collisions between the positron bunches and the laser light are separated downstream from the particle beam by a dipole magnet. After separation, the Compton photons exit the beam pipe through an aluminium window to reduce the synchrotron radiation background and are detected by a calorimeter. The photon detector is made of nine lead tungstate crystals organised in a 3×3 matrix which is optically connected to a photo-multiplier [28]. The position of the positron beam on either side of the IP is measured by a four-button pick-up BPM.

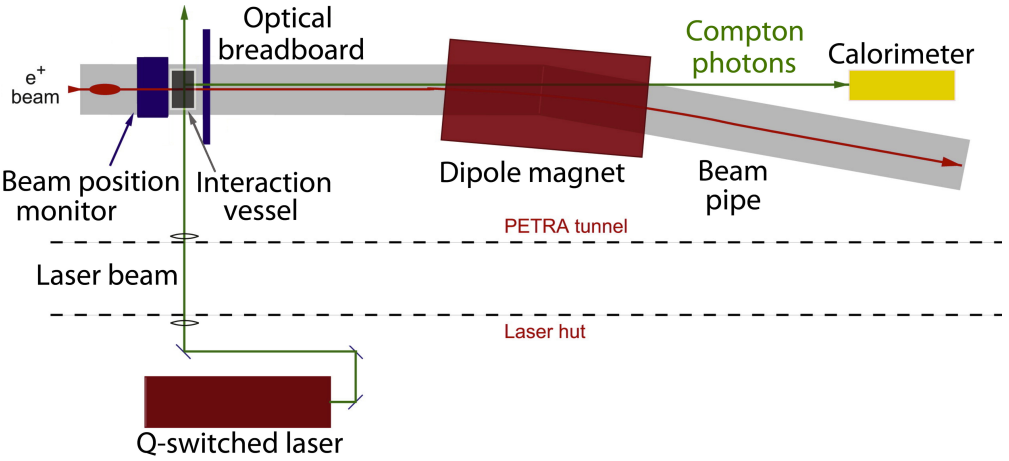

Figure 4.6: Overview of the LW setup [28].

4.2.2 Laser system

A commercially available Q-switched Nd:YAG laser system with a repetition rate of 20 Hz is used to produce the high power light pulses required for Compton scattering. The fundamental wavelength produced by the Nd:YAG laser is 1064 nm, which is frequency doubled (using a second harmonic generating crystal) to obtain a wavelength of 532 nm. Since this process is not completely efficient, the remnant 1064 nm light component is separated using dichroic mirrors and then dumped. Dichroic mirrors are plane glass mirrors that are reflective to a narrow range of wavelengths (532 nm) and transmissive to the remaining wavelengths (1064 nm). The intensity of the laser light is adjustable by rotating the polarisation of the laser light relative to a Brewster plate using a half-wave plate.

In Fig. 4.7, the setup in the laser hut is shown which houses the various components for the laser pulse production: second harmonic generator, motorised half-wave plate for polarisation control and polarisation sensitive beam splitter. An LAP250 lens together with the CMOS camera were installed to monitor the laser beam position jitter and spot size shot-by-shot. Furthermore, a low-power CW laser is used for aligning all components.

4.2.2.1 Seed unit

Seeding the laser is important for two reasons: it optimises the laser pulse build-up time and eliminates mode-beating. This is an effect that occurs when two different resonant modes of the laser cavity travel coincidentally and superpose, which causes an interference pattern produc-

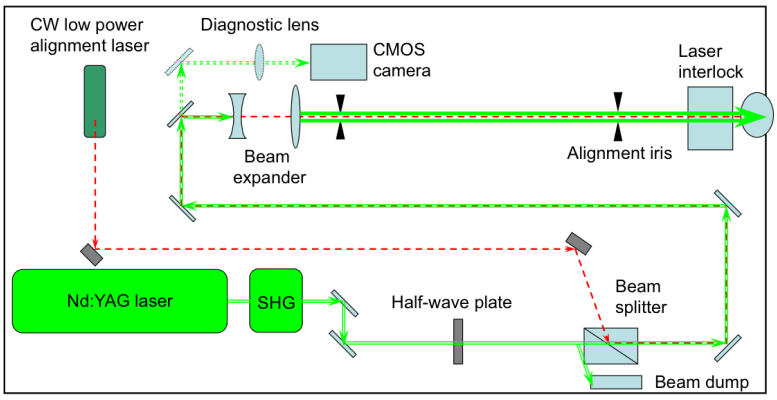

Figure 4.7: Schematic layout of the setup in the laser hut.

ing alternating regions of low and high laser intensity within a single laser pulse. The seeder produces an extremely narrow-band laser pulse at very precise time intervals. Its wavelength is to be carefully selected; it is important that the wavelength is a cavity mode to ensure good resonance, and that this cavity mode is one that is close to the Nd:YAG intensity emission peak to ensure good amplification of laser light .

To illustrate the effect of the seeding process on the longitudinal profile of the laser pulse, scope traces of the output of a photodiode are shown for the laser system unseeded and seeded in Figs. 4.8(a) and (b), respectively. The oscilloscope traces in Fig. 4.9 were taken with a 12.5-GHz photodiode connected to an oscilloscope with an analogue bandwidth of 6 GHz and a sampling rate of 20 GSa/s.

4.2.3 Optical components

The laser beam is expanded by a 5× beam expander ($f_1 = -50$ mm, $f_2 = 250$ mm) and collimated to approximately 25 mm diameter and transported from the laser hut into the accelerator tunnel underneath (see Fig. 4.7). The laser beam is then guided onto the LW breadboard mounted around the beam pipe, which contained the vertical (V) and horizontal (H) scanning systems. It consists of a piezo-electric driven mirror that deflects the laser beam before it is focused by the scanning lens. Fig. 4.10 and Fig. 4.11 show a schematic of the optical layout and a photo of the LW breadboard respectively. The arrows indicate movable translation stages. For the LW scanning system, two scanning lenses were chosen with different focal length. This was a necessary upgrade in order to match the different beam sizes and scan range requirements in the two profiling directions (V and H). The focussing lenses are an aplanatic lens with $f = 250$ mm (LV)

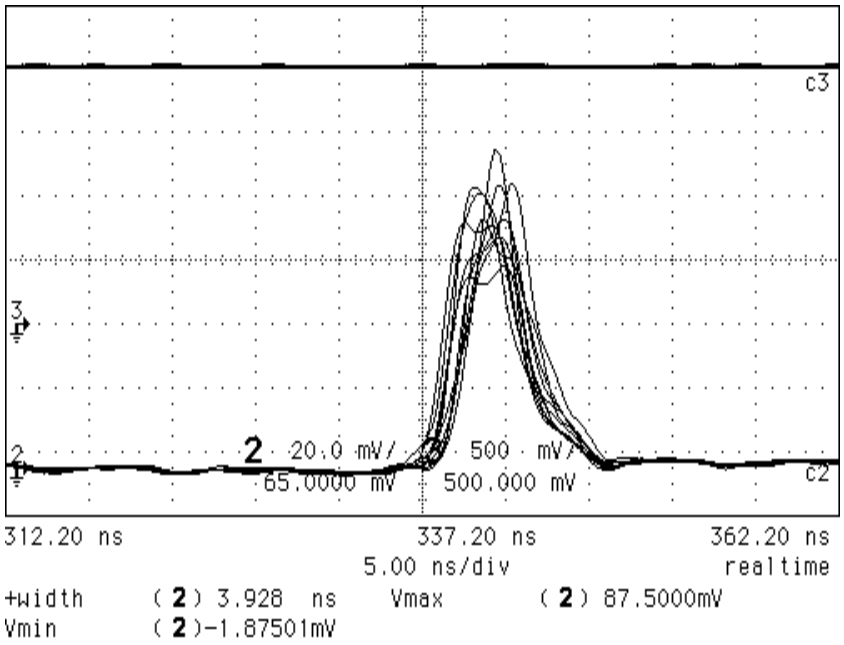

(a) Laser unseeded.

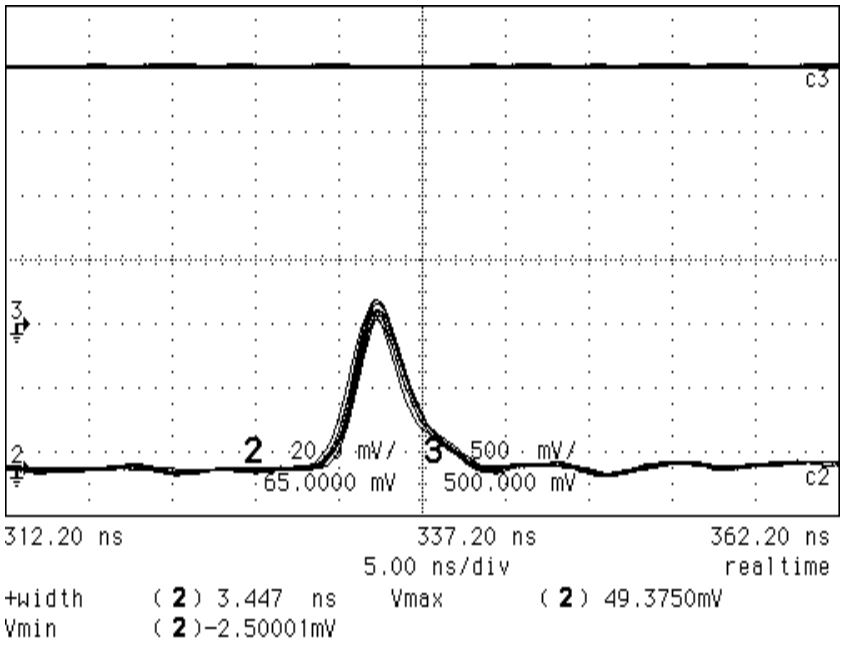

(b) Laser seeded.

Figure 4.8: Superimposed oscilloscope traces of the laser pulse as measured by a fast photo-diode (rise time $\sim$ 1 ns) when the laser was unseeded (a) and seeded (b).

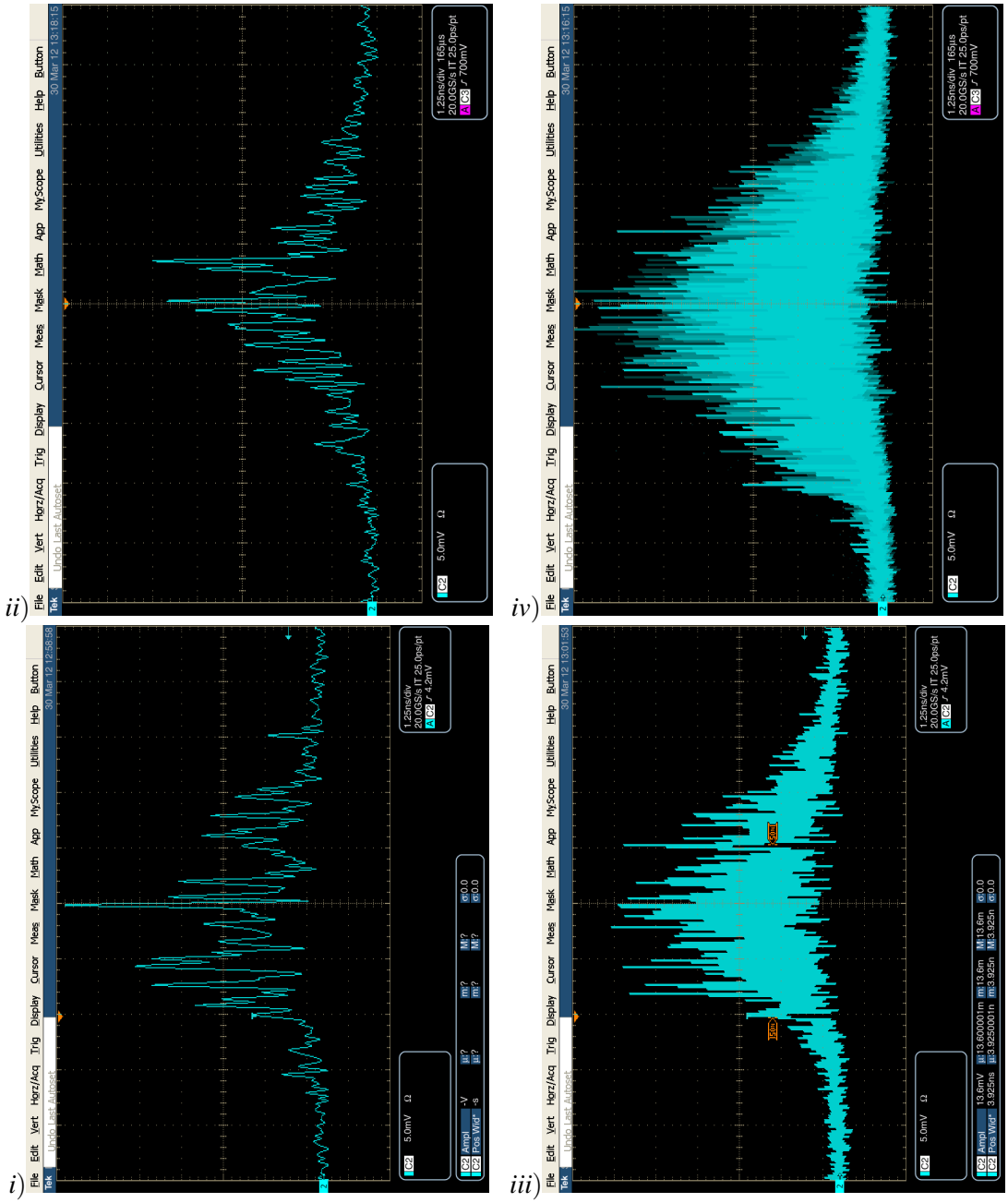

Figure 4.9: Unseeded single pulse internally (i) and externally (ii) triggered; unseeded envelope internally (iii) and externally (iv) triggered.

and a spherical singlet lens with $f = 750$ mm (LH). The scanning axis (V or H) is set by the position of the first movable mirror. The LW scanning units are similar to the ones used in [28] and a schematic is shown in Fig. 4.12.

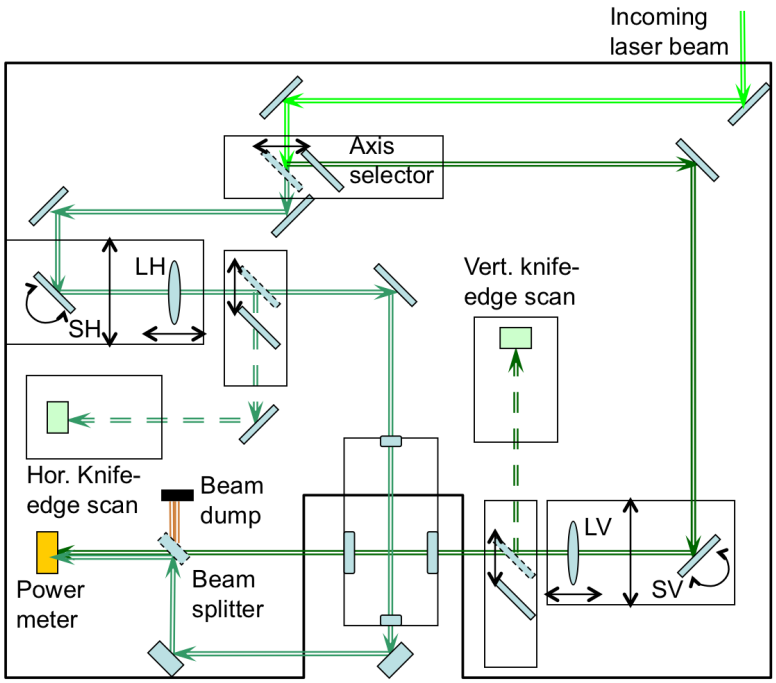

Figure 4.10: Schematic layout of the optical breadboard. The black arrows represent the direction in which each unit can be moved or rotated, the green arrows represent the laser.

By rotating the piezo-driven mirror by an angle θ, the laser beam is steered by an angle 2θ. The shift in transverse position of the focus (Δ) obtained when a laser beam is deflected by angle 2θ at the input of a focusing lens with focal length f, is given by $\Delta = 2f\theta$.

The scanning mirrors (SV and SH) are identical for both axes. These are 2-inch mirrors mounted on a piezo-electric stack that can be deflected by applying a voltage. The maximum deflection angle is 2.5 mrad with an applied voltage of 100 V. Therefore, given the focal lengths of 250 mm and 750 mm, the total maximum scanning range is 1.25 mm for the vertical axis and 3.75 mm for the horizontal axis.

Due to the longer focal length of the horizontal profiler lens, and the consequent increment of the laser Rayleigh range, the spot size at the input window of the old vacuum vessel was too small and the intensity definitely above the damage threshold of the window. An extension of the vacuum vessel was therefore necessary in order to move the input window further away from the focus of the laser beam and work in safe conditions. Simulations performed by DESY

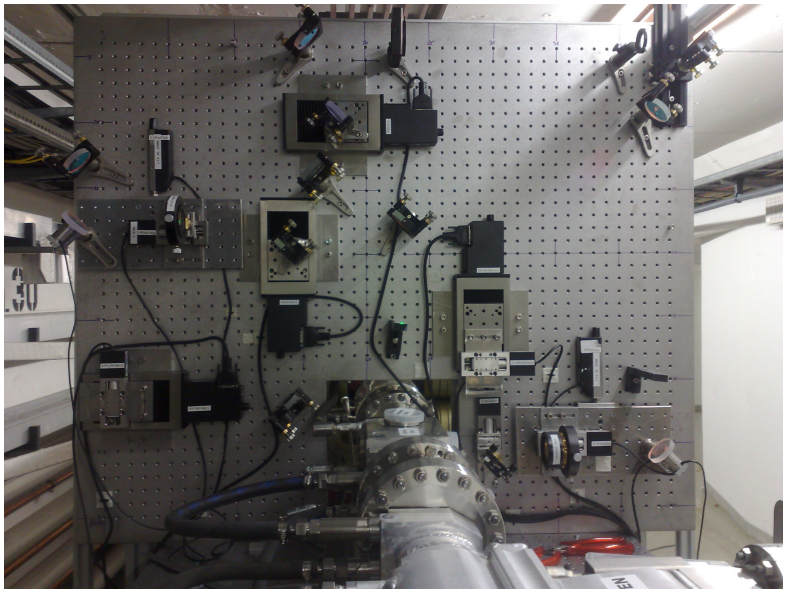

Figure 4.11: Photograph of the LW optical breadboard.

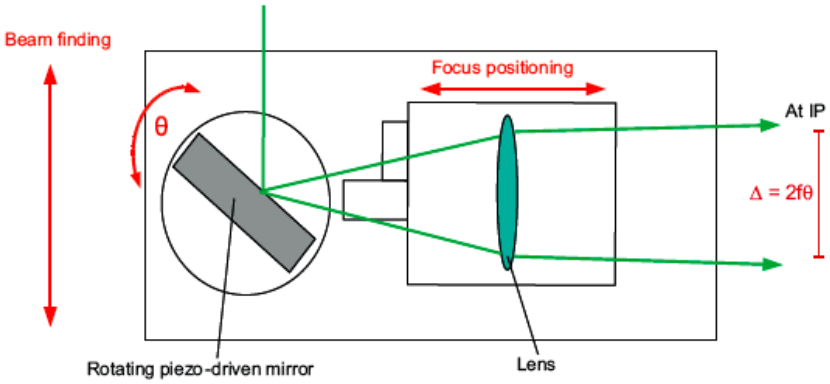

Figure 4.12: LW scanning unit.

showed that the new extended vessel does not introduce unacceptable RF fields.

In addition, there are also three webcams with alignment crosses to enable remote monitoring of the laser alignment.

4.2.4 Calorimeter

The PETRA-III laser-wire setup uses a photon detector to measure the energy deposited by Compton scattered photons downstream of the IP. This detector is the same used in the previous laser-wire experiment at PETRA-II; the information below is a summary of [30] and further details of calorimeter testing can be found in the same work.

Scintillation is a process by which radiation is absorbed in a medium and the energy from this goes into creating photons with specific frequencies characteristic of that medium. Lead tungstate (PbWO4) crystals have a fast-response time, are radiation hard and can be made into a compact form suitable for use in small detectors [38]. Its scintillation produces two main emission lines at 420 and 500 nm, which are fed into the PMT. The photon detector uses nine lead tungstate crystals, arranged in a 3×3 matrix of dimensions 18 mm $\times$ 18 mm $\times$ 150 mm. The crystals are wrapped in a glossy white film (to reduce light loss at the crystal surface), and are supported by an external aluminium frame. One end (18 mm $\times$ 18 mm cross-section) is fixed to the PMT using BICRON BC-630 optical grease. The crystals, supporting structure and PMT are stored in a light tight aluminium box which has been custom made to include BNC and HV connectors for the PMT unit. The whole structure is then encased with an arrangement of lead shielding which serves to protect against synchrotron radiation.

The Hamamatsu R2238 PMT unit works by first converting the incident photon flux into an electron flux via a photocathode, the electron flux is increased by multiple reflection off dynodes until it is finally focused onto an anode. The anode delivers an electrical signal whose area (and amplitude) is proportional to the original incident scintillation photon energy. However, if the PMT is exposed to too much energy, then the photocathode over-saturates the PMT and proportionality of the calorimeter signal is lost. Conversely, if exposed to too little energy, the photocathode produces too few electrons; some of which scatter in the non-perfect vacuum, also resulting in proportionality loss.

The calorimeter was tested in the DESY Test Beam 24 beam line, and exposed to single electrons of various energies. This test showed that the calorimeter response is linear. Further

details of this work can be found in [28, 30].

4.2.5 Cameras

An integral part of setting up and monitoring the laser were two cameras. A CCD camera was used for profiling the laser, i.e. measuring the longitudinal development of the transversal profile, and also for measuring the pointing jitter (see Section 4.3). Table 4.2 summarises the technical details for the CCD camera.

Table 4.2: Table of parameters for the WinCamD UCM CCD camera [31].

Vendor	Gentec
Model	WinCamD UCM
Pixel size	6.7×6.7 µm
Frame rate	> 5 Hz maximum for full frame
Resolution	1280×1024 pixels

A complementary metal oxide semiconductor (CMOS) camera was installed in the laser hut to enable monitoring the laser jitter and spot size shot-by-shot online. This camera is controlled by the laser-wire data acquisition (LWDAQ, see section 4.2.6). Table 4.3 summarises the technical details for the CMOS camera.

Table 4.3: Table of parameters for the Basler A601f CMOS camera [32].

Vendor	Basler
Model	A601f
Pixel size	9.2×9.2 µm
Frame rate	60 Hz
Resolution	656×491 pixels

Furthermore, there were also three webcams with alignment crosses installed to enable remote monitoring of the laser alignment.

4.2.6 Data acquisition

The Laserwire DAQ system (LWDAQ) hardware is based on a Peripheral Component Interconnect (PCI) Extensions for Instrumentation (PXI) system from National Instruments (NI). It consists of a PXI-8106 controller, a 1 GSa/s two-channel digitizer (PXI-5152), a precision timing module (PXI-6653) and a general-purpose DAQ (PXI-6251). Other hardware is accessed by using RS232 and GPIB communication. The DAQ software is written using NI LabVIEW

(version 8.5) and runs on the PXI controller module. It can be run from a User Interface (UI) on the controller module or accessed from the Petra Accelerator Control Room (BKR) via the TINE control system [33].

The voltage resolution of the digitizer is 8 bits. It was run with a full-scale range of 2 V. For a 500 mV, signal this means a DC accuracy of $\pm(1.26\%$ of 500 mV $+ 1.0\%$ of 2 V $+ 5$ mV$) =$ ± 31.3 mV [34].

Fig. 4.13 shows the processes that are part of the whole LW:

- The actual DAQ runs on the PXI controller.
- The Windows PC AccXPPelaser1 runs the interface between the TINE server and LW-DAQ (this is done using labview Shared Variables). This needs to be done in order to separate the LWDAQ from having to run a DESY standard windows installation.

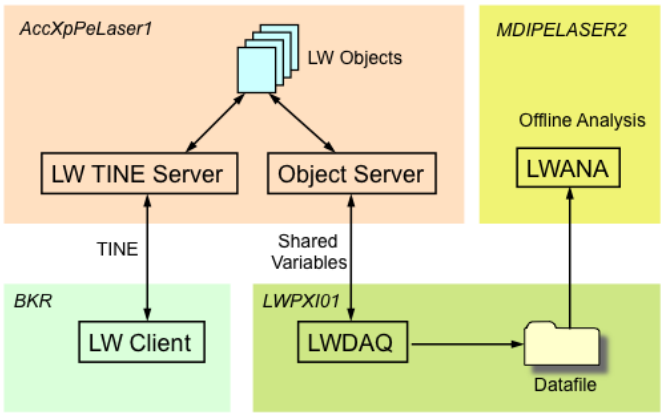

Figure 4.13: LWDAQ process distribution [35].

The functionality of LWDAQ based on an event-driven producer-consumer model. This model contains two processes, the producer and the consumer, who share a common buffer used as a queue. The producer generates data, puts it into the buffer and starts again. At the same time, the consumer is consuming the data, thus removing it from the buffer, one piece at a time.

The LWDAQ application is based on the *Model-View-Controller* (MVC) design pattern, which divides an application into three areas of responsibility: the *model*, where the data is handled; the *view*, which is the user interface (UI); and the *controller* which connects UI input and output to the model domain. The UI is based on a producer/consumer design pattern. The producer takes input from either the UI or a BKR command and passes it to the consumer where

it is refined and sent to the controller. The controller communicates with modules that interface directly with hardware (the digitizer, triggering, camera etc). This design is illustrated in Fig. 4.14.

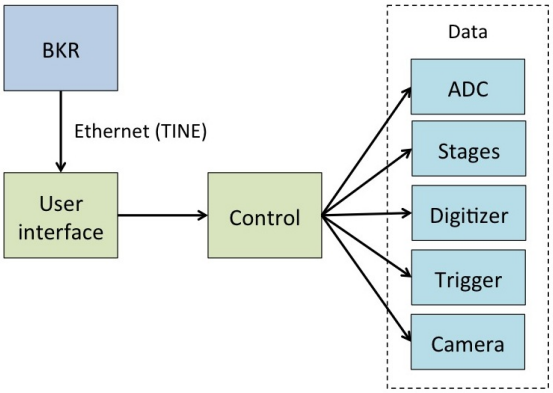

Figure 4.14: LWDAQ communication overview.

The following steps are performed:

1. Once the stages are in the correct positions then data are taken.
2. If the active stage is at the end of the scan range then the scan ends.
3. If not then data is taken and the stage then moved by an amount corresponding to the step size of the scan
4. Go back to step 2.

A flowchart describing a full scan process is presented in Fig 4.15.

4.2.6.1 Timing

The timing and sequencing of LWDAQ is shown in Fig. 4.16. It illustrates how many ADC samples per record (i.e. per laser pulse) are taken. The Digitizer and ADC are triggered every laser pulse (when stages have stopped moving). For each scanning stage position there are N triggers (records), and the ADC produces M samples - this is done so that if the DAC is moving the Piezo scanner it can detect any variation of the amplifier output with respect to the input signal.

A schematic overview of the synchronisation between the PETRA bunch clock, laser pulses and DAQ is shown in Fig. 4.17. The PETRA revolution clock runs with a frequency of 130.2 kHz,

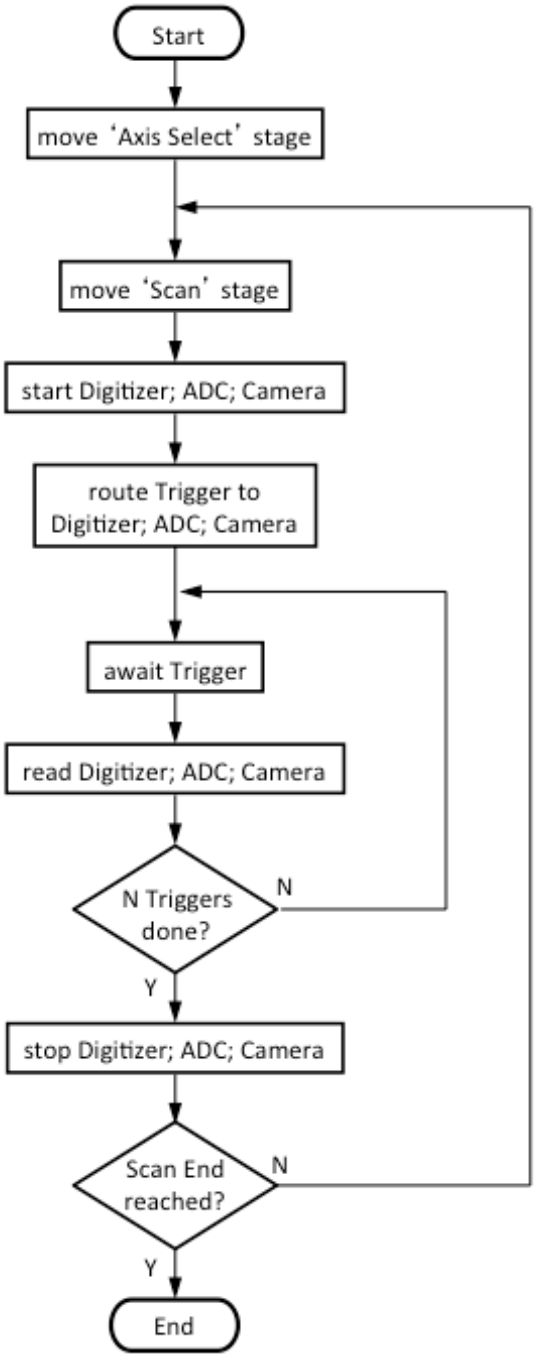

Figure 4.15: LWDAQ acquisition flowchart [35].

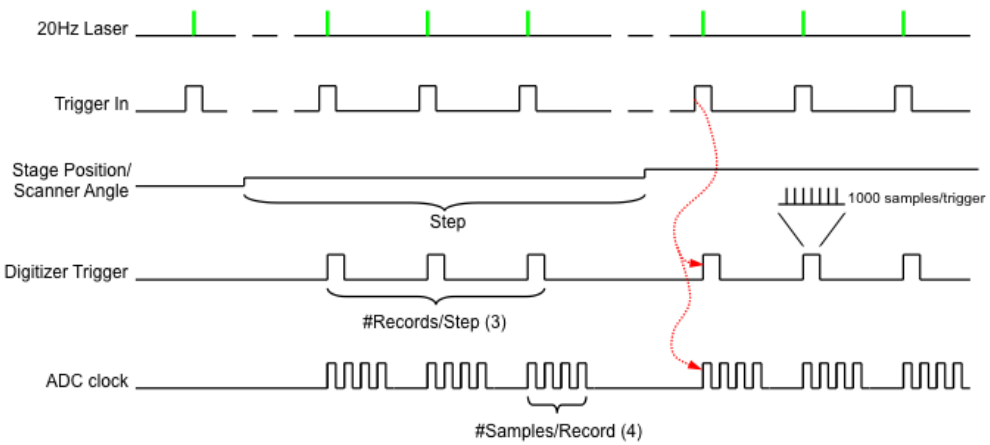

Figure 4.16: LWDAQ acquisition timing [35]. The red arrows represent so-called *cause and effect*.

i.e. an interval of 7.68 µs. This frequency is divided by a Stanford Systems DG535 Digital Delay Generator to 20 Hz to match the laser repetition rate. The DG535 fires the laser flash-lamps and the Q-switch for the Pockels cell. It also provides the trigger for LWDAQ (input via PXI-6653 Timing module). This trigger is then routed to the digitizer and DAQ modules via the PXI backplane. A further trigger is routed out of the PXI-6653 to the Basler camera with some delay.

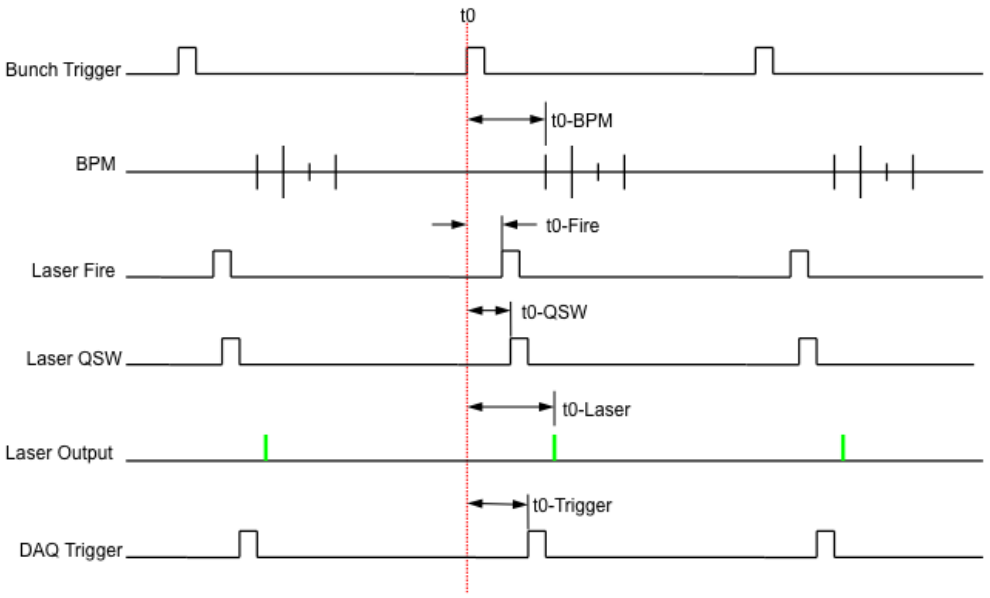

Figure 4.17: LWDAQ Petra-Laser-DAQ synchronisation [35].

The diagram in Fig. 4.18 shows how the laser pulse is timed so it arrives synchronised with the electron bunch. There is a 2.5-µs delay between the PETRA revolution clock and the firing of the laser flash-lamps; this delay can be adjusted remotely in oder to achieve maximum overlap

at the IP.

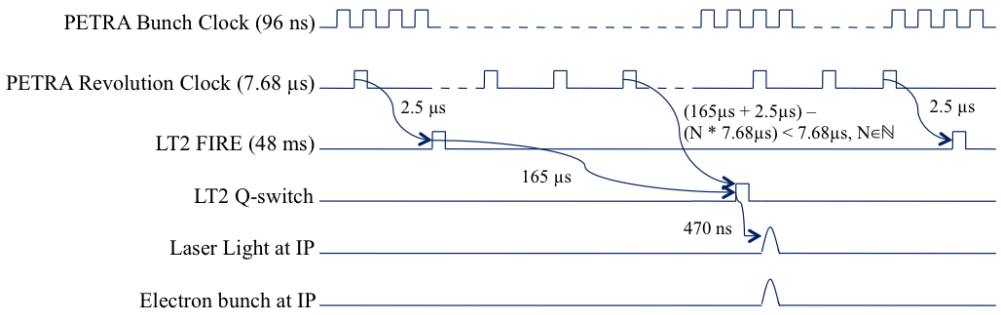

Figure 4.18: Timing the laser pulse with respect to the PETRA-III revolution clock [35]. The arrows represent *cause and effect* and show the propogation delay associated with them.

4.2.6.2 User interface

The user interface of LWDAQ is divided into three sections (see Fig. 4.19). All parameters needed to perform a scan are set inside the control panel: scan type, scan axis, transversal scan range, longitudinal position of the scanning lens and number of laser shots per position. A real-time graph of the scan is shown in the results panel. Scan progress and possible error messages are displayed in the status panel. The user interface also includes a sketch of the timing schematic, similar to Fig. 4.16.

4.2.7 Data analysis

In Fig. 4.20, a block diagram is shown of the LW data analysis (LWANA). The various steps of how the scan data is read from file and then processed are explained in the following sections.

4.2.7.1 Determine laser amplitude

The time it takes for the laser pulse to travel between the sampling trigger of the digitizer and the photodiode is used to find the amplitude of the laser pulse at the IP for each event. The peak value of the laser pulse is then used as a reference to normalise the laser amplitude at the interaction point.

Fig. 4.21 (a) and (b) show several laser pulse traces. It can be seen, that due to pulse jitter, not all laser pulses arrive at the IP with a maximum amplitude.

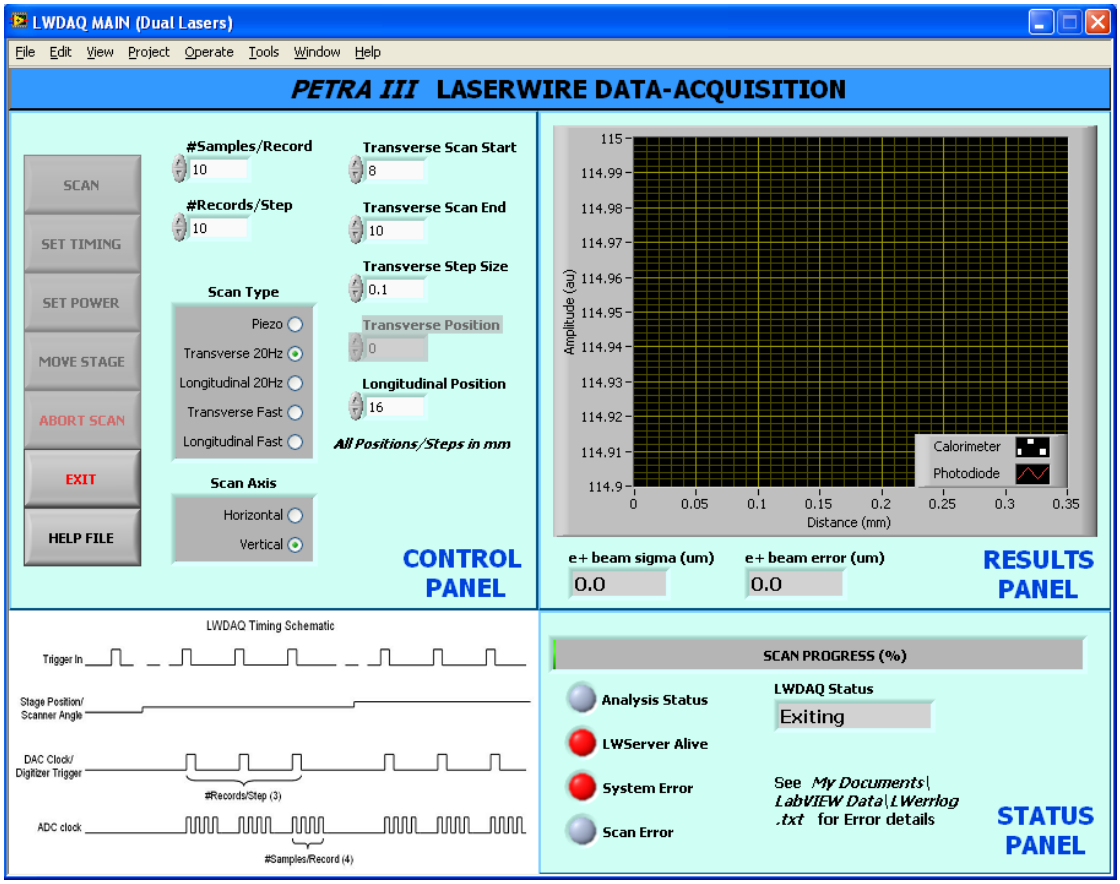

Figure 4.19: User Interface of LWDAQ [35].

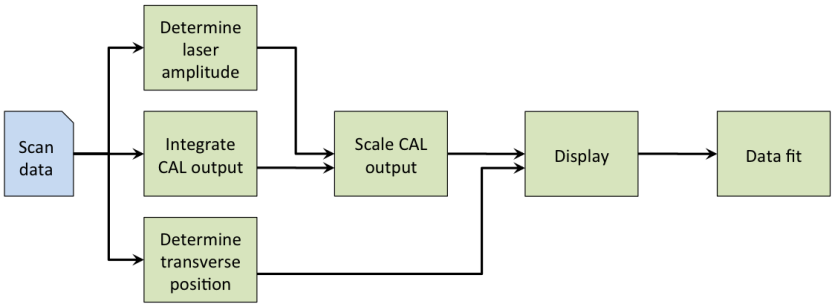

Figure 4.20: Steps of the data analysis process.

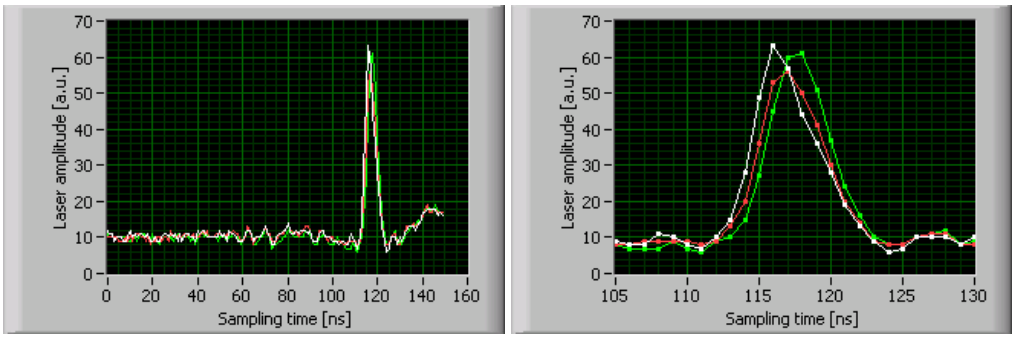

(a) Full sampling range. (b) Close up.

Figure 4.21: Example traces of sampled laser pulses, displayed (a) in the full 150 ns sampling range and (b) further zoomed in.

4.2.7.2 Determine transverse position

The piezo voltage is read from the ADC and converted according to the calibration value (see Fig. 5.2). The position of the transverse stage and the piezo mirror are added to get the full transverse position for each event.

4.2.7.3 Integrate and scale calorimeter output

For each event, the digitised CAL output values are summed and multiplied by the sampling time to get the integrated CAL output in units of $V_{min} \cdot t_s$. V_{min} is the smallest step change of the digitizer (7.8 mV) and t_s is the sampling time (1 ns).

Fig. 4.22 (a) and (b) show an example calorimeter output of a Compton event. Only a 150-ns window of the full raw trace is taken for the integration. The rest is used to determine a baseline, which is removed from the raw trace.

To scale the integrated CAL output, the relative laser power at the IP is taken (see Sec. 4.2.7.1) and each integrated CAL value is multiplied by this value.

4.2.7.4 Display and bin data

A scatter plot of the scaled integrated CAL output versus the full transverse position is diplayed (see Fig. 4.23(a)). These data points are then binned according to the step size of the scan. The mean value and standard error of the binned data are then also plotted against the transverse position (see Fig. 4.23(b)).

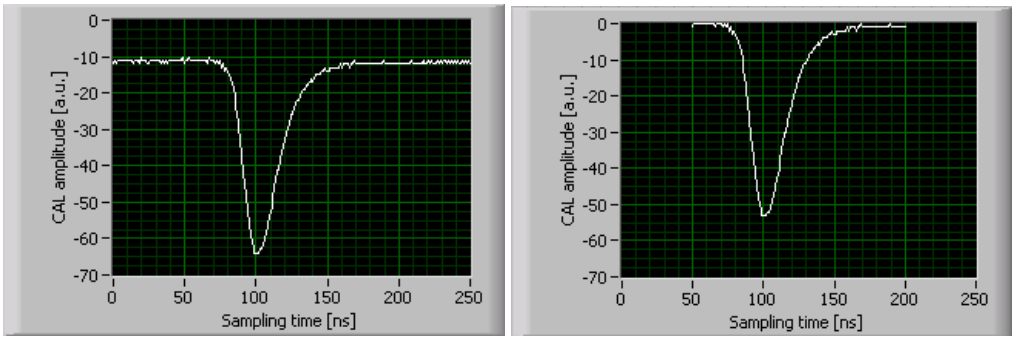

(a) Full sampling range. (b) Windowed CAL output with pedestal removed.

Figure 4.22: Example calorimeter output of a Compton event: (a) raw trace and (b) windowed signal with pedestal removed.

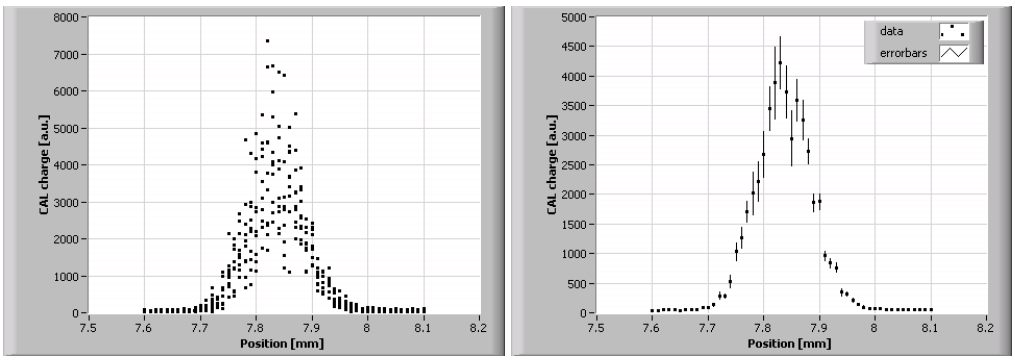

(a) Scatter plot. (b) Binned data.

Figure 4.23: The integrated calorimeter pulses plotted against the transverse position: (a) scatter plot and (b) binned.

4.2.7.5 Fit binned data

The data was fitted using a convolved function $f(x)$. This function is a convolution between the mixed-mode Gaussian function defined in Eq. 4.3 which describes the laser profile and another simple Gaussian function describing the transversal electron beam profile.

$$
\begin{aligned}
f_{\text{Laser}}(x) &= A_1 \cdot \exp\left(-\frac{(x-\mu_1)^2}{2\sigma_1^2}\right) \cdot \left(1 + b\,(x-\mu_1-\Delta)^2\right) + d_1 \\
f_{e^-}(x) &= A_2 \cdot \exp\left(-\frac{(x-\mu_2)^2}{2{\sigma_2}^2}\right) + d_2 \\
f(x) &= f_{\text{Laser}}(x) \otimes f_{e^-}(x) = \qquad (4.1) \\
&= A \cdot \frac{1}{\sqrt{\frac{1}{{\sigma_1}^2} + \frac{1}{{\sigma_2}^2}}\left({\sigma_1}^2 + {\sigma_2}^2\right)^2} \cdot \sqrt{2\pi} \cdot e^{-\frac{(-x+\mu)^2}{2({\sigma_1}^2+{\sigma_2}^2)}} \times \\
&\quad \times \left(\left(1 + b\Delta^2\right){\sigma_2}^4 + {\sigma_1}^2{\sigma_2}^2\left(2 + b\left(2\Delta(-x+\Delta+\mu) + {\sigma_2}^2\right)\right) + \right. \\
&\quad \left. + {\sigma_1}^4\left(1 + b\left((-x+\Delta+\mu)^2 + {\sigma_2}^2\right)\right)\right) + d, \qquad (4.2)
\end{aligned}
$$

where the fit parameters were the profile centroid μ, the electron beam sigma σ_2 (or σ_b), the amplitude of the convolved profile A and a profile offset d. The laser profile half-width σ_1 (or σ_{Laser}), the mode-mixing factor b and the mode offset Δ were fixed to the results from the laser profile studies presented in Section 4.3.2.

All beam scans were done at laser focus, so the input for σ_{Laser} was fixed to the smallest measured laser size (see Fig. 4.30 and 4.32). The b and Δ parameters were fixed to the values which correspond to the longitudinal position of the minimum laser sigma (see Fig. 4.29 and 4.31). The values for both scan axes are given in Table 4.4.

(a) Vertical scan.

Parameter	Unit	Value
σ_{Laser}	[µm]	12.53 ± 0.16
b	[mm^{-2}]	7333 ± 798
Δ	[µm]	13.24 ± 0.56

(b) Horizontal scan.

Parameter	Unit	Value
σ_{Laser}	[µm]	21.22 ± 0.14
b	[mm^{-2}]	3080 ± 222
Δ	[µm]	-17.09 ± 0.33

Table 4.4: Input parameters for the convolved profile fit.

To estimate the systematic error, contributing from the parameters σ_{Laser}, b and Δ, the fit was performed using each parameter shifted by its statistical error and the signal re-fit for σ_b. There are three parameters, each with three values (nominal, positive shift and negative shift), resulting in 27 fits per scan. For each combination of possible input values for σ_{Laser}, b and Δ,

the scan data was fitted with the function in Eq. 4.2. Therefore, the result for each fit is a set of fit parameters $\{\mu, \sigma_b, A, d\}_i$ and their errors $\{\Delta\mu, \Delta\sigma_b, \Delta A, \Delta d\}_i$. The beam size that is presented for all the beam scans in Chapter 5, is the mean value of those individual fit sizes $\sigma_b = \overline{\sigma_{b,i}}$. The overall statistical error of the beam size can be determined by $\Delta\sigma_b{}^{\text{stat}} = \overline{\Delta\sigma_{b,i}}$. However, the beam size will also have a systematic error due to the error of the input parameters. This can be easily calculated by $\Delta\sigma_b{}^{\text{sys}} = \text{std}(\sigma_{b,i})$. Therefore, if not stated otherwise, explicit results are always presented in the form $\sigma_b \pm \Delta\sigma_b{}^{\text{sys}} \pm \Delta\sigma_b{}^{\text{stat}}$.

Example binned profiles with applied fits for vertical and horizontal scans respectively are shown in Fig. 4.24 (a) and (b). The vertical beam size is $\sigma_{b,V} = 22.10 \pm 0.15^{\text{sys}} \pm 0.45^{\text{stat}}$ µm and the horizontal beam size is $\sigma_{b,H} = 221.66 \pm 0.02^{\text{sys}} \pm 4.06^{\text{stat}}$ µm. As the horizontal beam size is much larger than the vertical one, the laser size error has much less of an impact and the systematic error is insignificant. Vertically, the beam size is almost down to the laser spot size, so the systematic error cannot be neglected.

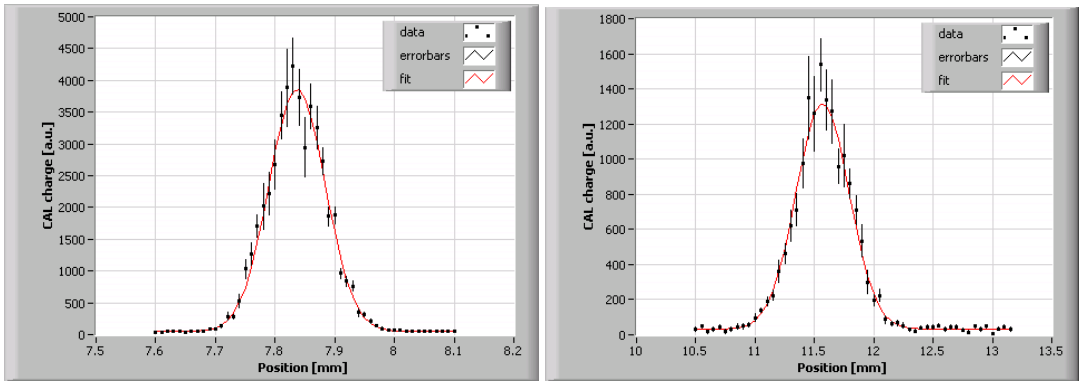

(a) Vertical (b) Horizontal

Figure 4.24: Example binned scan profiles with applied fit.

4.3 Characterisation of the Laser System

This section presents the results of the studies regarding two important laser parameters, i.e. pointing jitter and transverse mode.

4.3.1 Pointing jitter

Random, thermal vibrations occurring in the laser head cause the direction in which the laser pulse is fired from the laser to fluctuate [19]. This directional fluctuation is called pointing jitter.

The pointing jitter at the laser IP for both scanning directions was measured by deflecting the laser beam after the respective scanning lens and just before the entrance window of the vacuum chamber and putting a laser diagnostic camera (Gentec WinCamD) exactly at its focus point. The centroid positions of several consecutive laser shots were recorded and their values relative to their mean fill the histograms shown in Fig. 4.25.

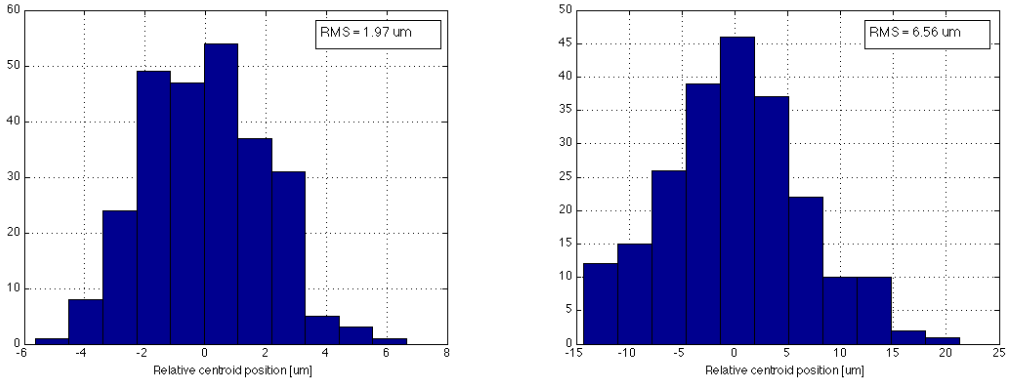

(a) LAP 250. (b) LAP 750.

Figure 4.25: Histograms showing the pointing jitter at the laser IP for the LAP 250 lens (a) and the LAP 750 lens (b) respectively.

Therefore the pointing jitter angle can be calculated using the RMS values from the histograms as $1.97\ \mu m/0.25\ m = 7.86\ \mu rad$ for the vertical scan and $6.56\ \mu m/0.75\ m = 8.74\ \mu rad$ for the horizontal scan.

4.3.2 Transverse mode

The laser beam propagates longitudinally as described by Eq. 3.112, where $W(z)$ is the laser waist defined as the distance from the centroid of the spot to the position where the intensity drops by a factor $\frac{1}{e^2}$, W_0 is the minimum laser waist, λ is the laser wavelength and M^2 is a factor ≥ 1 which represents the quality of the real beam compared to an ideal TEM_{00} Gaussian beam (for which $M^2 = 1$).

The longitudinal profile of the laser beam was measured by focusing it with the same lenses

used for the horizontal and vertical setup at a location close to actual interaction point thus reproducing real conditions. CCD images of the laser beam were recorded using a laser diagnostic camera (Gentec WinCamD) at a range of distances from the focusing lens. An image of the laser intensity profile can be seen in Fig. 4.26. This shows the laser spot focussed by the LAP250 lens used for scanning in the vertical direction.

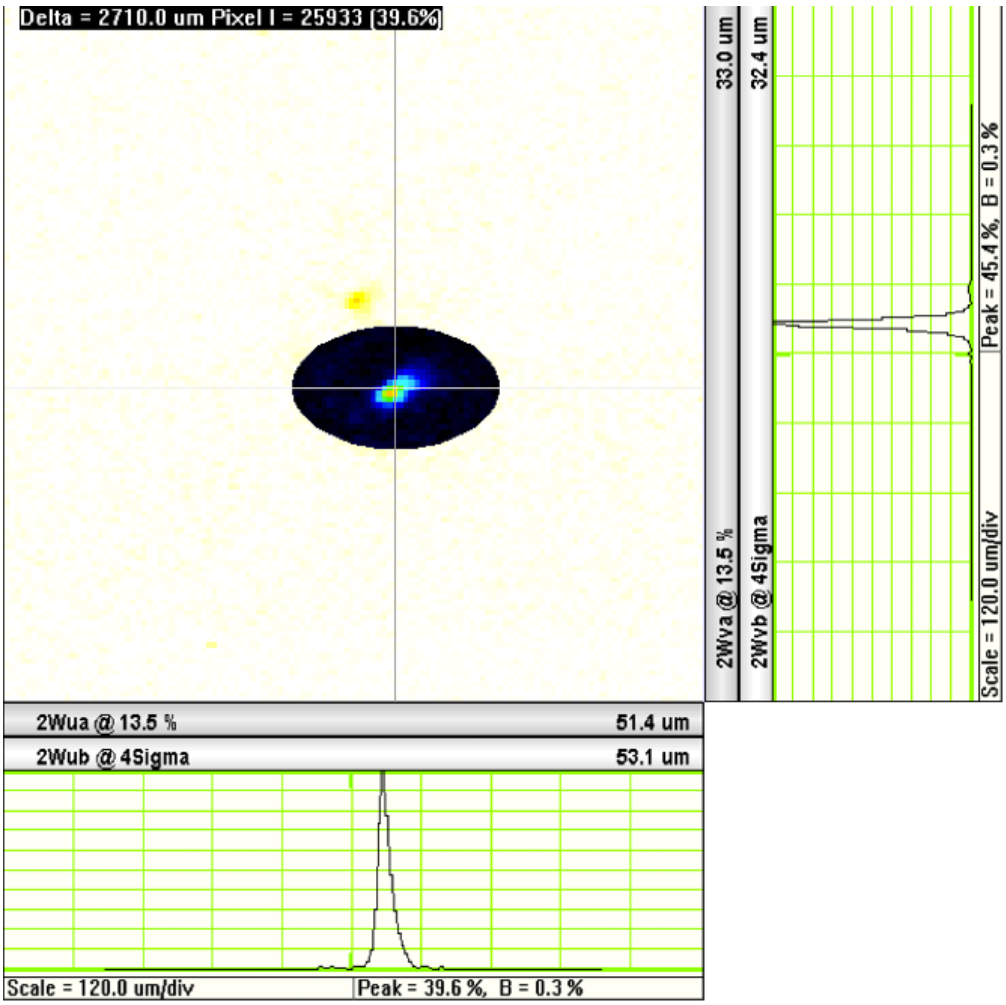

Figure 4.26: Laser pulse image taken using CCD profiling equipment in the post IP section of the LW system.

The profiling software provides a 2D profile of the laser intensity, however only the horizontal projection is of importance as this is the direction in which the laser traverses while scanning. It can be seen that the laser pulse does not have a Gaussian profile, but shows a slight skew. For this reason, several CCD images were taken at each position along the longitudinal axis and

their horizontal profiles extracted and then fitted with a mode-mixing Gaussian function,

$$f(x) = A \cdot \exp\left(-\frac{(x-x_0)^2}{2\sigma^2}\right) \cdot \left(1 + b\,(x - x_0 - \Delta)^2\right) + d, \tag{4.3}$$

where x_0 is the centroid of the laser pulse, σ is half the laser pulse width, A is the fit amplitude and d represents the fit offset. This function takes a mixing of the first two laser modes into account which is described by a linear combination of the first two Hermite polynomials. This is accounted for by a mode mixing factor b. The orthogonal laser modes are thus assumed to be incoherent and shifted by some offset Δ.

The mode-mixing can be observed when going further away from the focus of the lens. Fig. 4.27 shows a CCD image of laser pulse in the far field. Two peaks can be seen in the horizontal projection, a clear indication of two competing modes.

Example laser profiles fitted with Eq. 4.3 are shown in Fig. 4.28. These are the laser profiles at 100 µm intervals across the Rayleigh range along the longitudinal axis. The numbers $i) - ix)$ correspond to arbitrary longitudinal stage positions of $20100 - 20900$ µm. The error bars on the profile data result from imaging 20 laser shots at every step and taking mean value and the standard deviation of the spot sizes obtained from all of these images.

The resulting fit parameters x_0, Δ, A, and b of the fits in Fig. 4.28 are shown in Fig. 4.29. The laser pulse half-widths σ of the fit in Eq. 4.3 are presented in Fig. 4.30. All values are plotted against the stage position along the longitudinal axis. The arrows on the data points in Fig. 4.29 and 4.30 mark the values which were then used for fitting the beam scan data as they correspond to the smallest laser spot size (see Section 4.2.7.5).

The longitudinal development of the transversal laser beam size in Fig. 4.29 was also fitted with the Rayleigh fit given in Eq. 3.112. The results of that fit are stated in Table 4.5. It can be seen that the laser mode quality M^2 is much bigger than the ideal value 1 which proves that the laser was definitely not running in single mode.

Table 4.5: Fit parameters for the Rayleigh fit for the LAP250 lens.

Parameter	Value	Unit
Minimum waist W_0	25.79 ± 0.15	µm
Profile sigma σ	12.89 ± 0.08	µm
Mode quality factor M^2	4.99 ± 0.18	
Rayleigh range	0.787 ± 0.029	mm

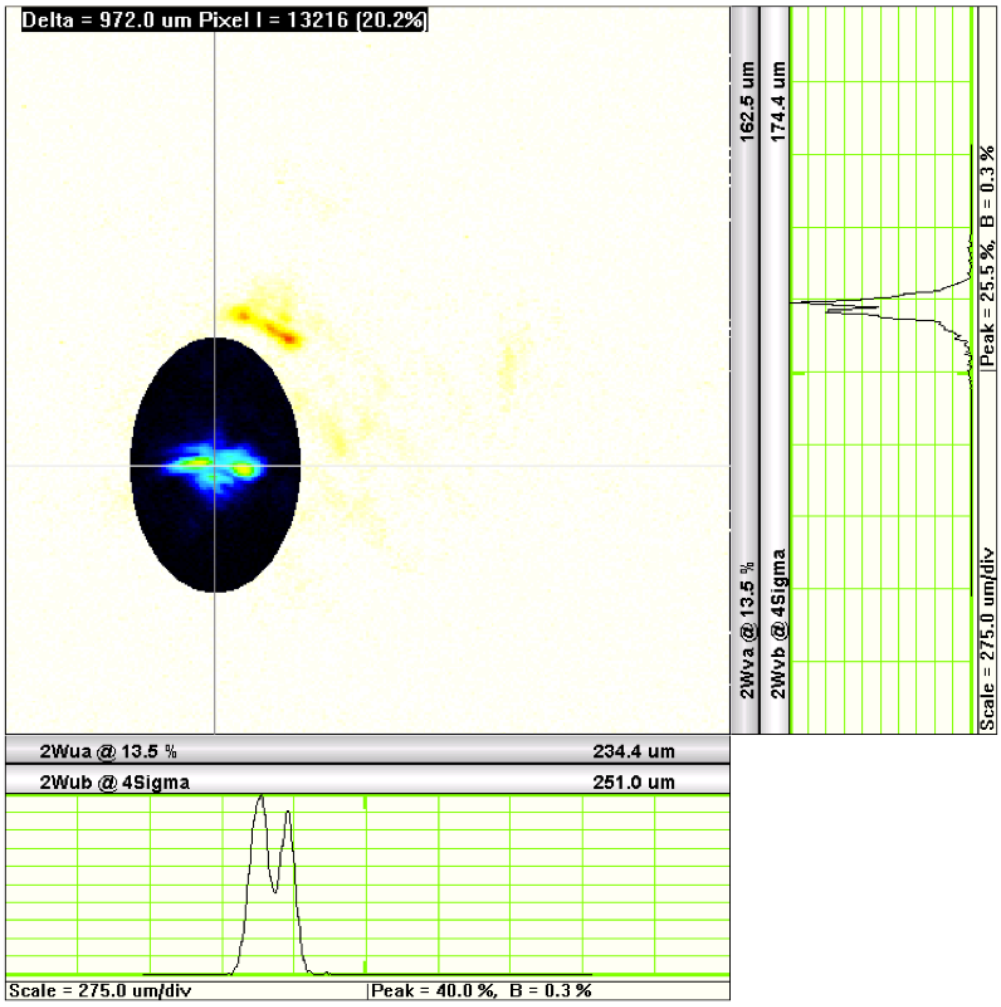

Figure 4.27: CCD image of a laser pulse in the far field.

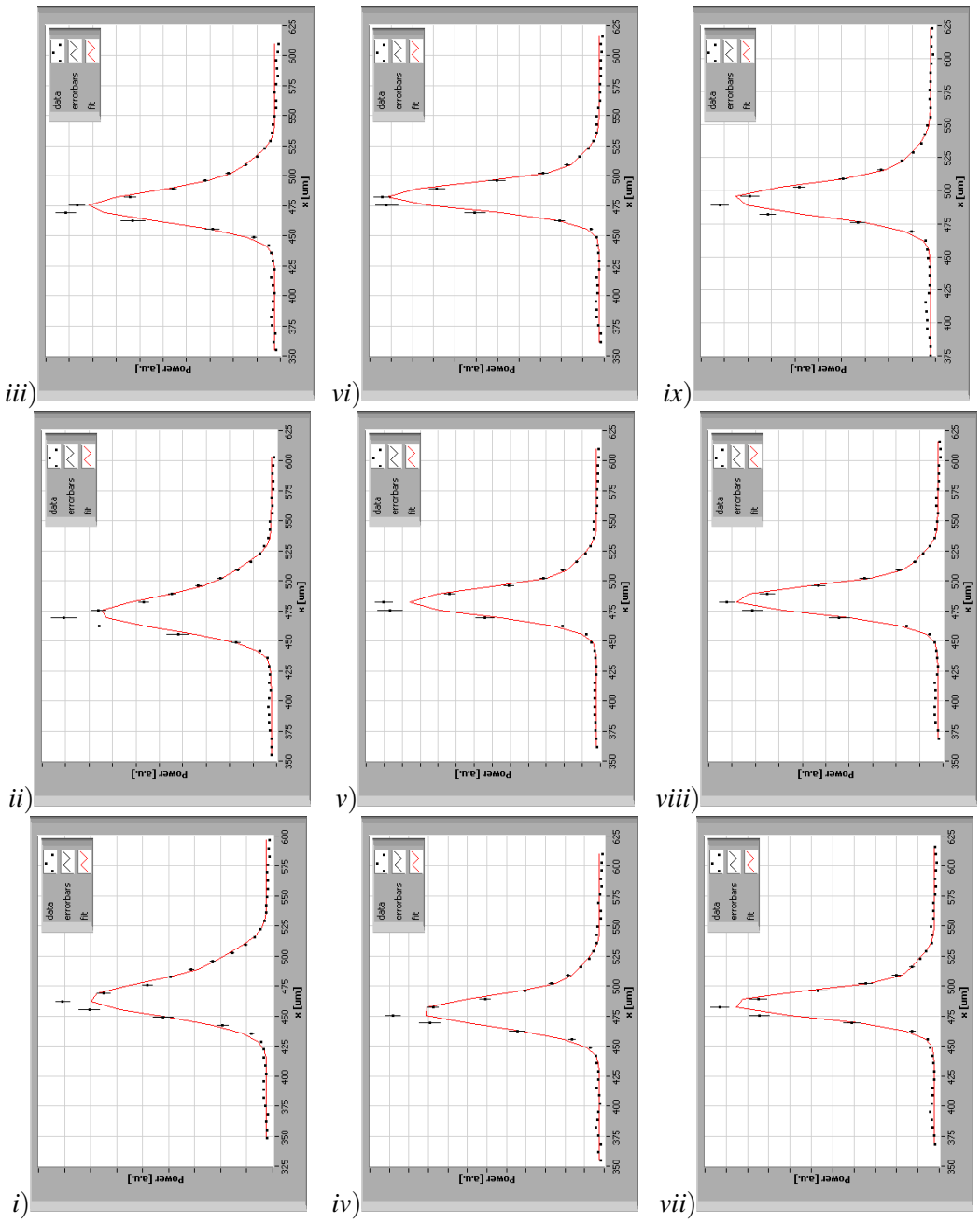

Figure 4.28: Binned laser pulse profiles fitted with the mode-mixing Gaussian fit-function in Eq. 4.3. The plots show the laser profile at 100 µm intervals along the longitudinal axis. The numbers $i) - ix)$ correspond to longitudinal stage positions of 20100 – 20900 µm respectively.

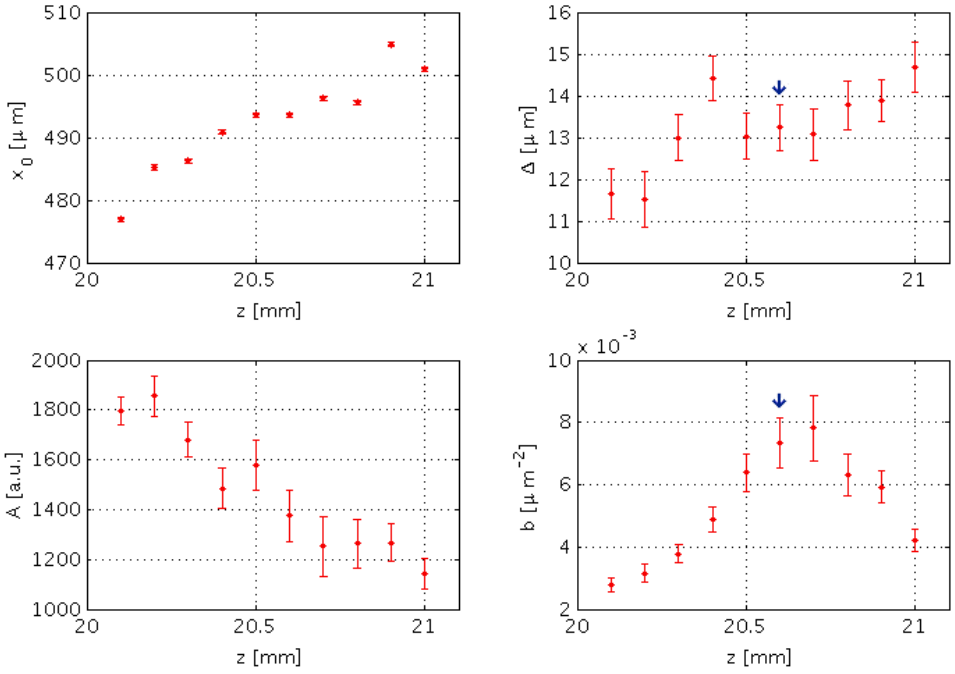

Figure 4.29: Parameters of the mode-mixing Gaussian fit in Eq. 4.3 along the longitudinal axis for the LAP250 lens. The arrows on the data points mark the values used for fitting the beam scan data as they correspond to the smallest laser spot size (see Section 4.2.7.5).

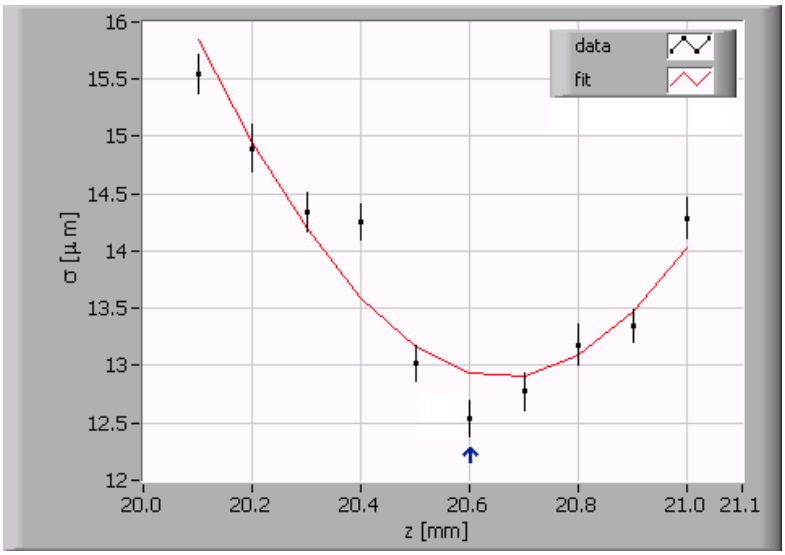

Figure 4.30: σ of the mode-mixing Gaussian fit in Eq. 4.3 plotted against the stage position along the longitudinal axis for the LAP250 lens. The fit was done using the Rayleigh fit in Eq. 3.112. The arrows on the data points mark the values used for fitting the beam scan data as they correspond to the smallest laser spot size (see Section 4.2.7.5)

The same procedure was used to study the longitudinal behaviour of the transverse laser profile for the LAP750 lens which is used for the horizontal scans. The same mode-mixing fit function was applied to the CCD images taken in the tunnel. The resulting fit parameters of the these fits are shown in Fig. 4.31 and the results from the Rayleigh fit applied to the laser profile sigmas in Fig. 4.32 is given in Table 4.6.

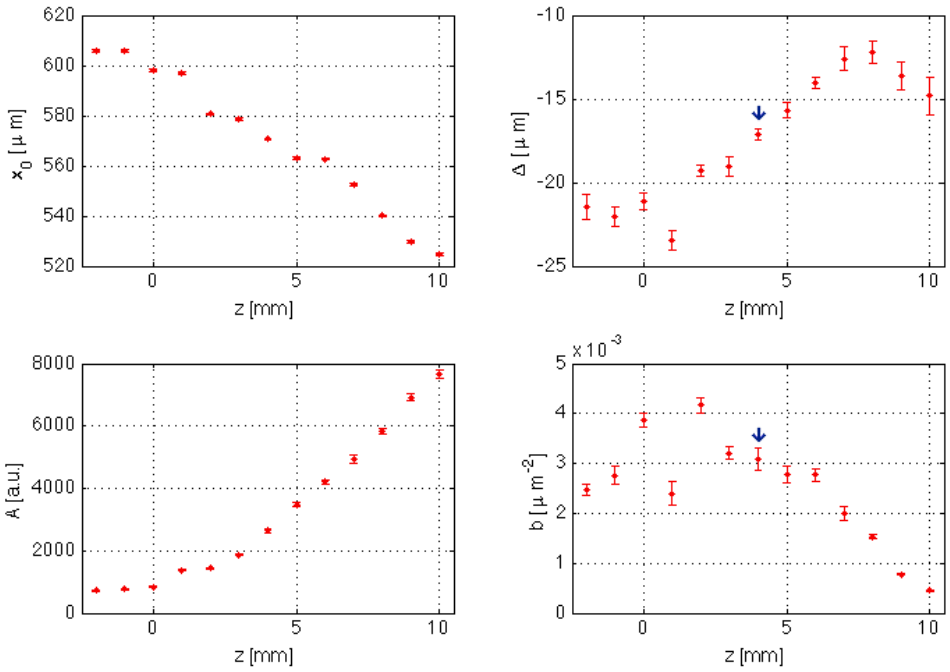

Figure 4.31: Parameters of the mode-mixing Gaussian fit along the longitudinal axis for the LAP750 lens. The arrows on the data points mark the values used for fitting the beam scan data as they correspond to the smallest laser spot size (see Section 4.2.7.5).

As mentioned above, the arrows on the data points in Fig. 4.31 and 4.32 mark the values which were then used for fitting the beam scans data as they correspond to the smallest laser spot size (see Section 4.2.7.5).

Table 4.6: Fit parameters for the Rayleigh fit for the LAP750 lens.

Parameter	Value	Unit
Minimum waist W_0	41.77 ± 0.16	μm
Profile sigma σ	20.89 ± 0.08	μm
Mode quality factor M^2	1.49 ± 0.02	
Rayleigh range	6.928 ± 0.123	mm

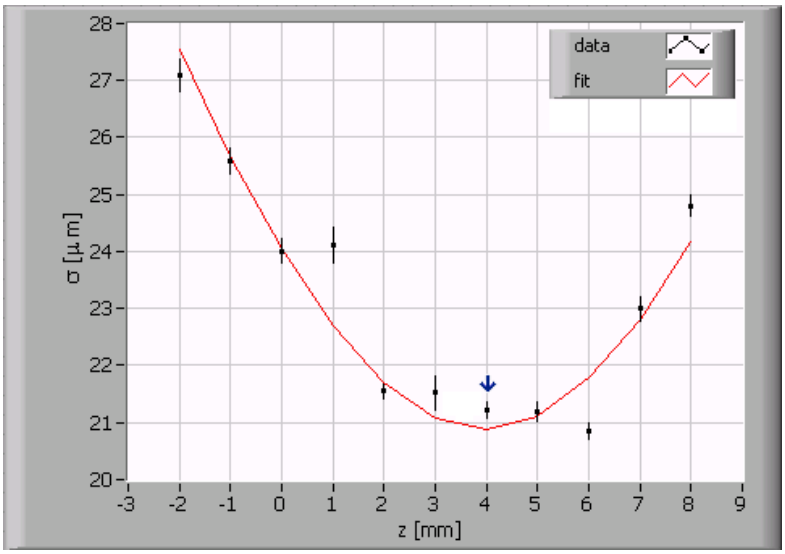

Figure 4.32: σ of the mode-mixing Gaussian fit plotted against the stage position along the longitudinal axis for the LAP750 lens. The Rayleigh fit is also shown. The arrows on the data points mark the values used for fitting the beam scan data as they correspond to the smallest laser spot size (see Section 4.2.7.5).

4.3.3 Conclusions and discussion of discrepancies

Comparing the Rayleigh fit parameters for both axes from Table 4.5 and 4.6, it is remarkable that the horizontal minimum beam waist is not three times the vertical minimum beam waist. If believing the horizontal minimum beam waist $W_H = 41.77$ µm and the corresponding $M^2 = 1.49$, using $W_{\text{in}} = \frac{M^2 \lambda f}{\pi W_H}$ (see Eq. 3.116), the input beam size for the LAP750 lens can be calculated to $W_{\text{in}} = 4.53$ mm. With the same input beam size at the LAP250 lens and with the measured $M^2 = 4.99$, the vertical minimum beam waist would be $W_V = 46.63$ µm, which corresponds to vertical laser beam size of $\sigma_{l,V} = 23.32$ µm. Using the horizontal M^2, the vertical minimum beam size would be $W_V = 13.92$ µm, which corresponds to vertical laser beam size of $\sigma_{l,V} = 6.96$ µm. This laser spot size could not have been resolved sufficiently by the profiling as the camera only had a CCD pixel size of 6.7 µm (see Section 4.2.5).

Chapter 5

Laser-Wire Measurements

This chapter is divided into several parts. Section 5.1 illustrates the preliminary measurements that were carried out to understand and calibrate the behaviour of the scanning units (translation stages and piezo mirrors). Also, the behaviour of the calorimeter was studied. In Section 5.2, the LW results are then compared with the synchrotron radiation imaging system introduced in Section 4.1.2, which sits at the other side of the ring. A possible influence of an unexpected laser tilt at the interaction point or an effect on the laser spot size caused by the vacuum window were scrutinised. Both effects would limit the minimum laser spot size at the IP and therefore limit the accuracy of positron beam size measurement (see Section 5.3).

The calibrated LW was then used to carry out several beam studies, the results of which are presented in Section 5.4. First, the particle beam was bumped vertically to measure the vertical shift of the scan profile and to check for a systematic scaling error. Then the orientation of the transversal beam ellipse was studied by changing two adjacent skew quadrupoles. Finally, frequency shifts were applied to the RF thereby changing the beam energy in order to determine the dispersion by measuring the horizontal shift of the scan profile as a function of the beam energy.

5.1 Preliminary measurements

5.1.1 Translation stage linearity

To measure the linearity of the translation stages, the WinCamD was set up in a similar configuration to that when measuring the transverse mode of the laser (see Section 4.3.2), i.e. for each

scan axis the camera was mounted to be in the focal plane of the laser-wire lens. The translation stages were then moved in steps of 1 mm and 20 images per step were taken with the CCD camera. The images were evaluated with the same profiling software, taking the laser spot centroid of each image.

In Fig. 5.1, the binned data is shown plotted against the position of the translation stage. The data was fitted with a linear fit, the proportionality factor is also given in the plot.

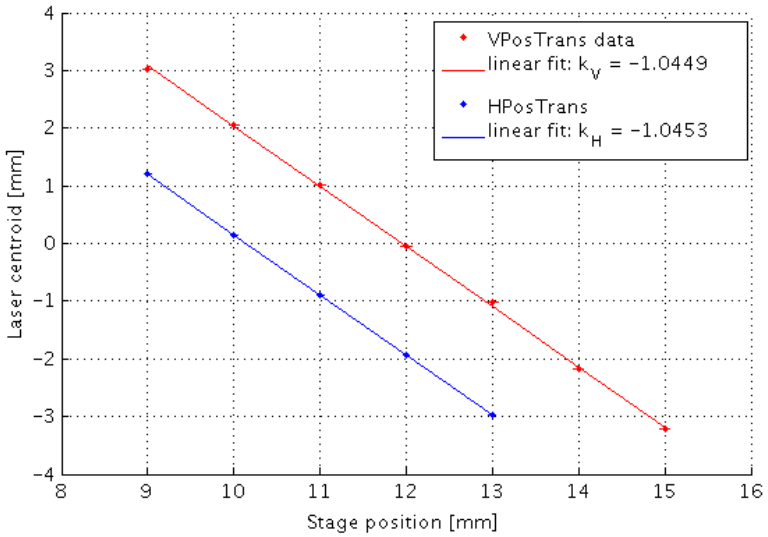

Figure 5.1: Measured laser centroid position versus set translation stage position for both scan axes. The proportionality factor is given in the legend.

This means that the scale error in the stage position for both axes is less than 5%.

5.1.2 Piezo range

In the same way, the response of the piezo-driven mirrors was measured. Voltage was applied to the mirrors in steps of 2 V and 20 images per step were taken with the CCD camera. Again, the laser spot centroid of each image was determined with the CCD image profiling software.

The binned data is plotted against the applied piezo voltage in Fig. 5.2. The data was fitted with a linear fit, the proportionality factor is also given in the plot.

5.1.3 Calorimeter behaviour

The calorimeter signal amplitudes of several LW scans were taken and plotted against their errors (see Fig. 5.3). If the error is purely statistical, a $\sqrt{x}$-like shape would be expected. Therefore,

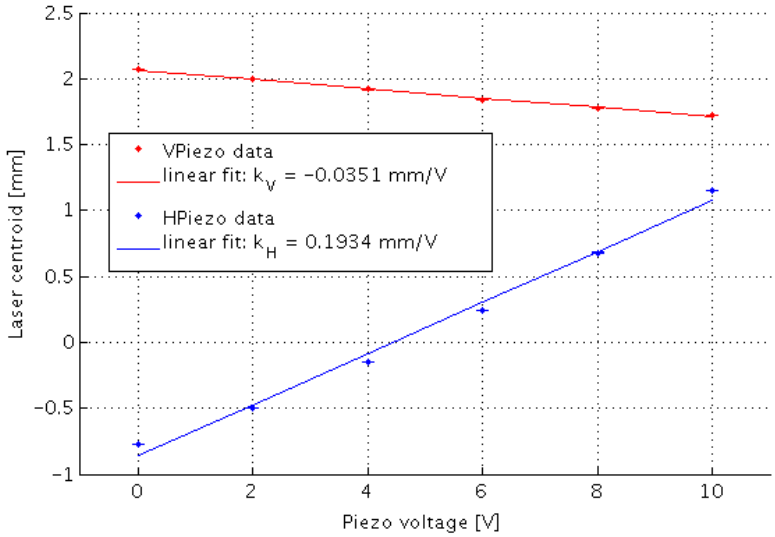

Figure 5.2: Measured laser centroid position versus applied piezo voltage for both scan axes. The proportionality factor is given in the legend.

the calorimeter behaviour was fitted with the following function,

$$f(x) = p_0 + p_1 \cdot x + p_2 \cdot \sqrt{x}, \tag{5.1}$$

which also takes a possible scaling factor into account.

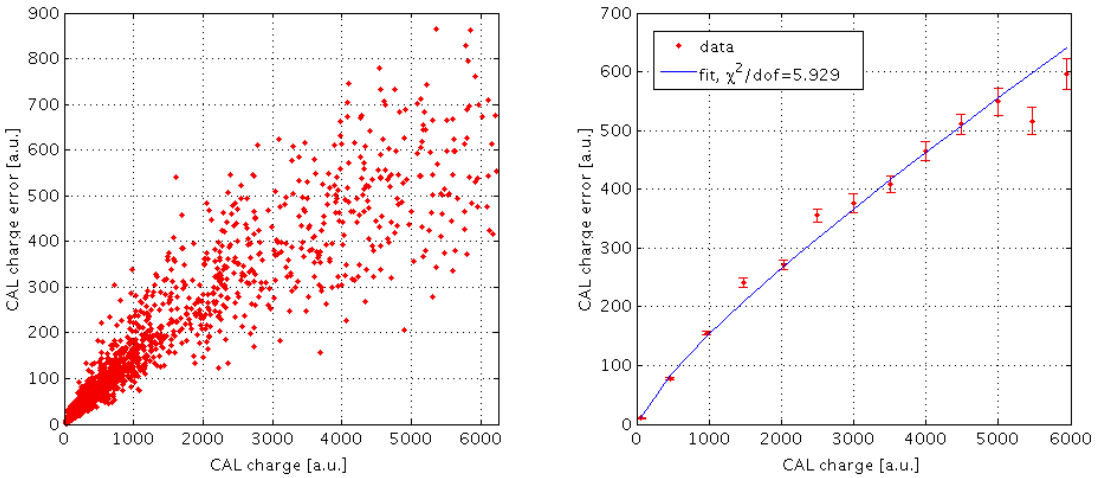

Figure 5.3: Measured calorimeter charge versus signal spread. The fit on the right plot was performed using the function in Eq. 5.1.

The resulting fit parameters are $p_0/10^{-5} = -21.20 \pm 3.48$, $p_1/10^{-2} = 6.72 \pm 0.95$ and $p_2 = 3.41 \pm 0.50$.

5.2 Benchmarking the Laser-Wire

On two days at the end of October 2011, the laser-wire was used to perform scans synchronous with the synchrotron radiation (SR) imaging system introduced in Section 4.1.2. The aim of these measurements was to compare the results of both systems, which are given in Table 5.1. For the first set of measurements, PETRA-III was running in 40-bunch mode with a total current of about 80 mA, which gives a bunch current of about 2 mA; for the second set of measurements, the filling pattern was 60 bunches with a total current of about 100 mA, i.e. a bunch current of about 1.7 mA

In this table, the error for the measured beam width at the LW location is given as a total error $\Delta\sigma^{\text{tot}} = \sqrt{(\Delta\sigma^{\text{sys}})^2 + (\Delta\sigma^{\text{stat}})^2}$. The emittance was calculated using the optics parameters at the LW location: $\beta_x = 11.24$ m, $\beta_y = 19.98$ m, $D_x = 139.2$ mm and $\frac{\Delta E}{E} = 1.3 \cdot 10^{-3}$ [36, 37]. Each measurement is presented with its timestamp.

(a) 19/10/2011

	Laser-wire		SR imaging system	
Timestamp	$\sigma_{b,y}$ [µm]	ε_y [pm·rad]	Timestamp	ε_y [pm·rad]
20:17:49	19.45 ± 0.40	18.94 ± 0.78	20:15:15	12.33
20:29:45	26.46 ± 0.36	35.03 ± 0.94	20:39:01	19.44
20:44:46	21.98 ± 0.36	24.17 ± 0.80	20:49:06	12.06
	Laser-wire		SR imaging system	
Timestamp	$\sigma_{b,x}$ [µm]	ε_x [nm·rad]	Timestamp	ε_x [nm·rad]
20:00:18	222.14 ± 4.12	1.48 ± 0.09	20:15:09	1.14

(b) 25/10/2011

	Laser-wire		SR imaging system	
Timestamp	$\sigma_{b,y}$ [µm]	ε_y [pm·rad]	Timestamp	ε_y [pm·rad]
15:23:12	20.29 ± 0.40	20.61 ± 0.82	15:04:09	5.9
15:27:58	19.56 ± 0.31	19.15 ± 0.61	15:29:32	6.0
15:55:27	19.30 ± 0.37	18.65 ± 0.71	16:01:41	6.5

Table 5.1: Comparing the results of the laser-wire and the synchrotron radiation imaging system (see Section 4.1.2).

On the first day (see Table 5.1 (a)), after a first vertical and horizontal measurement with a stable beam, the emittance was increased and the measurement repeated. The emittance was then restored to its previous value for a final measurement. In this first set of measurements, the ratio between the vertical emittance determined by the LW and the value from the SR imaging system lies between 1.5 and 2. The horizontal emittance as measured by the LW is a factor 1.3

larger than the result of the SR imaging system.

For the second set of vertical measurements (see Table 5.1 (b)), where the beam was kept stable for three successive measurement, this ratio computes to be between 2.9 and 3.5. It can therefore be seen, that not only is there a disagreement between the LW and the SR imaging system by a rather large factor, but also and more worryingly this factor is not constant.

In order to investigate these discrepancies, several possibilities were considered:

- Non-linearity across the vertical range (see Section 5.4.1).
- Laser tilt (see Section 5.3.1).
- Effect of the vacuum window on the laser spot size (see Section 5.3.2).

5.3 Laser studies

5.3.1 Laser tilt

An unexpected tilt in the vertical plane of the laser beam would result in a measured beam size that is larger than the actual beam size, as now the horizontal profile is coupled into the measurement (see Fig. 5.4).

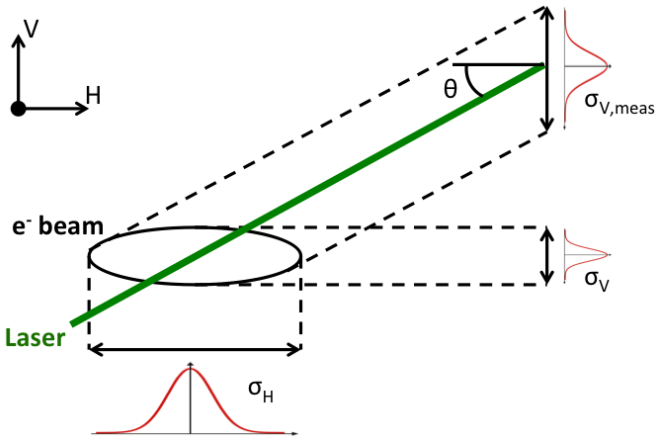

Figure 5.4: Schematic illustrating how the beam size measurement is affected by a tilted laser beam.

When rotating coordinates by an angle θ, the following relation applies,

$$\begin{pmatrix} x' \\ y' \end{pmatrix} = \begin{pmatrix} \cos\theta & \sin\theta \\ -\sin\theta & \cos\theta \end{pmatrix} \begin{pmatrix} x \\ y \end{pmatrix}. \tag{5.2}$$

With this, the expectation value for y'^2 can be calculated,

$$\langle y'^2 \rangle = \langle x^2 \rangle \sin^2\theta + \langle y^2 \rangle \cos^2\theta - \cancel{\langle xy \rangle} \cos\theta \sin\theta. \tag{5.3}$$

The cross term $\langle xy \rangle$ vanishes because the x and y positions are uncorrelated in the untilted beam. This leads to the following equation for the vertical beam size,

$$\sigma_{V,m}{}^2 = \sigma_H{}^2 \sin^2\theta + \sigma_V{}^2 \cos^2\theta, \tag{5.4}$$

where σ_V and σ_H are the actual electron bunch profile sizes and $\sigma_{V,m}$ is the measured vertical profile size.

This leads to the an expression for a possible laser tilt angle,

$$\sin\theta = \sqrt{\frac{\sigma_{V,m}{}^2 - \sigma_V{}^2}{\sigma_H{}^2 - \sigma_V{}^2}}. \tag{5.5}$$

At the end of October 2011, the synchrotron radiation system measured the vertical emittance to be 12.33 pm·rad (see Table 5.1 (a)). Taking the Twiss parameters at the laser-wire IP, this would lead to a vertical beam size of 15.70 µm. However, the LW result was $\sigma_{V,m} = 19.45 \pm 0.40$ µm. The SR system measured a horizontal emittance of 1.14 nm·rad, which leads to an expected horizontal beam size at the LW IP of 213.44 µm. Therefore, the possible tilt would be 54 mrad or 3.1°, which is far too much considering that a tilt of this magnitude would be visible by eye. A change in the laser beam tilt of $\Delta\theta = \pm 1°$ would correspond to a change in vertical beam size of only $\Delta\sigma_{V,m} = \pm 0.43$ µm.

5.3.2 Vacuum window effect on spot size

As described in subsection 4.2.2, for both directions, the laser parameters including sigma at the focus of the lens was measured by setting a mirror just before the vacuum window and putting a CCD camera in the focus. In this setup, the laser light propagates only in air. When scanning the electron beam however, the laser goes through the vacuum window before the focus. To rule out a possible magnification effect due to aberration, a similar setup was tested in the lab. Twenty CCD frames for each measurement were taken. The laser spot size without the vacuum window was $\sigma_x = 22.87 \pm 0.07$ µm and $\sigma_y = 22.48 \pm 0.05$ µm. After inserting the window into the laser

path at the same position as in the real experimental setup, the spot size was measured to be $\sigma_y = 22.01 \pm 0.05$ µm and $\sigma_x = 23.07 \pm 0.03$ µm. This means that propagating the laser beam through the vacuum window has no significant contribution to the spot size at the IP.

5.4 Beam studies

5.4.1 Vertical bump

In order to check if there was systematic error in the beam size measurement in the form of an unwanted scaling factor, the PETRA-III beam was bumped vertically at the laser-wire IP. A bump of 2 mm caused a beam loss before a measurement could be taken. After refilling the machine a scan was taken, then the beam was shifted by 1 mm and measured again. More bumps could not be applied as the beam was lost again shortly after. The PETRA-III was running in 60-bunch mode with a total current of about 100 mA, which gives a bunch current of about 1.7 mA.

The scan profiles before and after the vertical bump can be found in Fig. 5.5. These plots show, that the centre of the scan profile got shifted by 0.95 mm while the size remained the same before and after the bump. This means that the error in the profile shift is less than 5%.

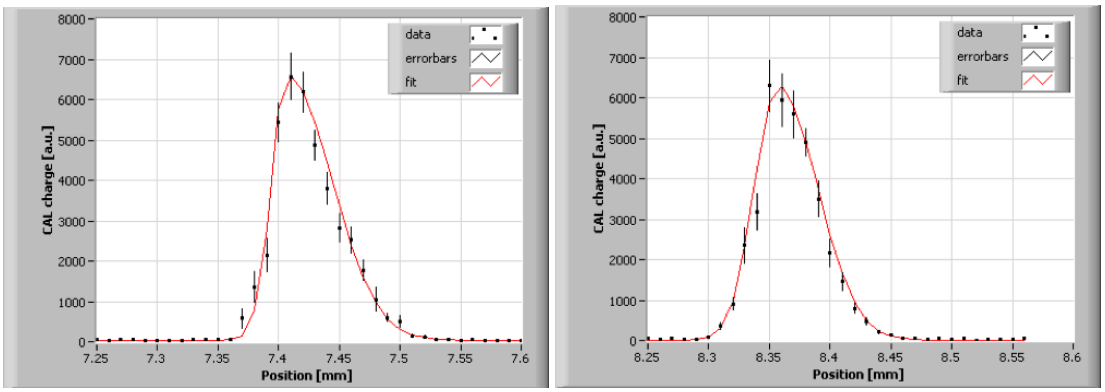

(a) $\bar{y} = 7.41$ mm, $\sigma_y = 25.0 \pm 0.6$ µm (b) $\bar{y} = 8.36$ mm, $\sigma_y = 25.8 \pm 0.4$ µm.

Figure 5.5: Vertical scan profiles, before (a) and after (b) bumping the beam vertically by 1 mm (note: different horizontal scales).

5.4.2 Adjusting the beam ellipse

To measure the orientation of the transversal beam ellipse, skew quadrupoles were used to rotate the beam. This was done to ensure the beam ellipse was sitting upright. In Fig. 5.6 and 5.7, the vertical and horizontal beam sigmas are shown when varying the currents for the skew quadrupole magnets QS1 and QS4. The error bars for the measured beam width data represent a total error $\Delta\sigma^{\text{tot}} = \sqrt{(\Delta\sigma^{\text{sys}})^2 + (\Delta\sigma^{\text{stat}})^2}$. For each measurement series, the current in one magnet was varied while the current for the other was kept constant. For the QS1 series, QS4 was set to $I_{\text{QS4}} = -4.5$ A and for the QS4 measurements, QS1 was fixed to a value of $I_{\text{QS1}} = -6.8$ A.

For most of these measurements, PETRA-III was running in top-up mode. However, for currents $|I_{\text{QS1,4}}| \geq 40$ A topping up the beam was not possible anymore. The filling pattern for the entire shift was 60 bunches with a total current of about 70 mA, which gives a bunch current of about 1.2 mA.

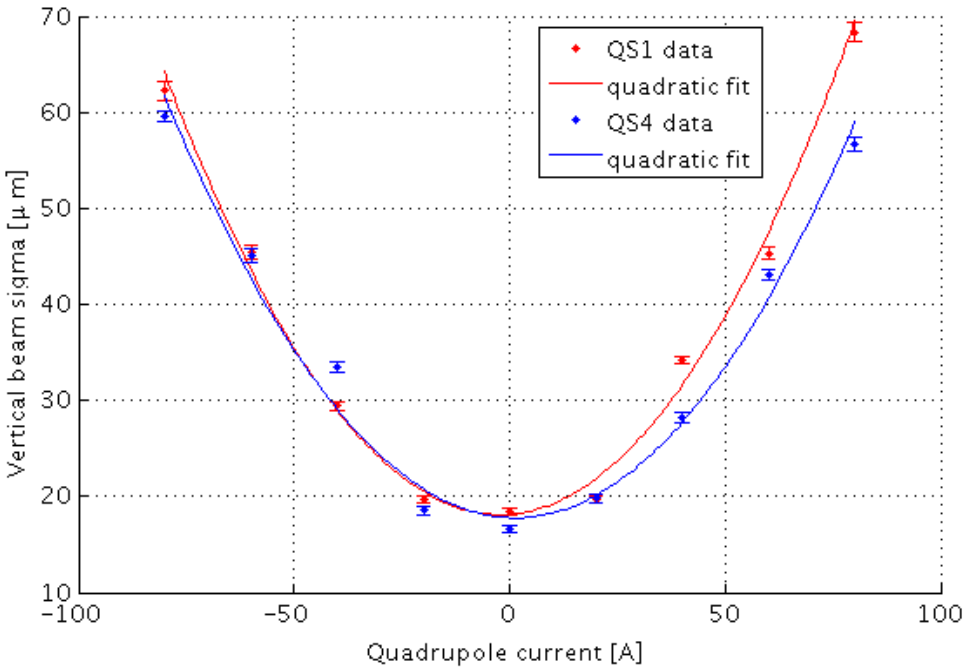

Figure 5.6: Measured vertical beam sigma versus the current applied to quadrupole QS1 and QS4 respectively

The data were fitted to second order polynomials, $f(x) = p_0 + p_1 \cdot x + p_2 \cdot x^2$, and the results for all four fits are given in Tables 5.2 (a) and (b). For both axes, the beam ellipse was measured

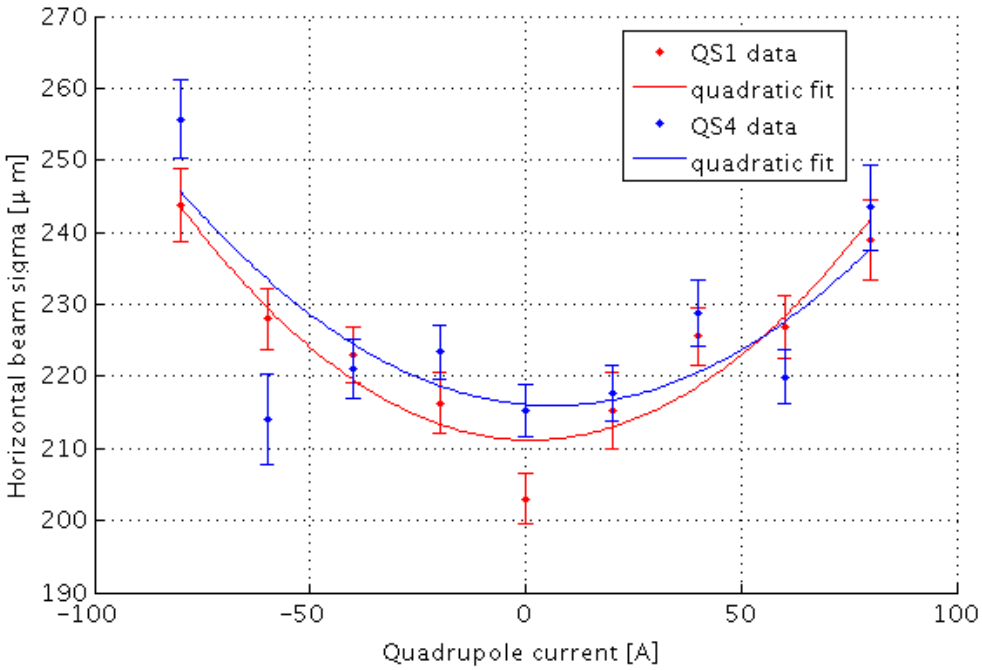

Figure 5.7: Measured horizontal beam sigma versus the current applied to quadrupole QS1 and QS4 respectively.

to be at its minimum when both skew quadrupoles are set to their default current.

(a) Vertical

	$p_2/10^{-3}$	$p_1/10^{-2}$	$p_0/10$
QS1	7.61 ± 0.45	3.28 ± 1.94	1.81 ± 0.10
QS4	6.65 ± 0.44	-1.75 ± 2.18	1.78 ± 0.13

(b) Horizontal

	$p_2/10^{-3}$	$p_1/10^{-2}$	$p_0/10^2$
QS1	4.94 ± 0.97	-1.10 ± 4.37	2.11 ± 0.03
QS4	4.01 ± 1.48	-4.96 ± 6.97	2.16 ± 0.04

Table 5.2: Results from the quadratic fit for the beam ellipse orientation.

5.4.3 Dispersion measurement

As shown in Eq. 3.49, an offset from the betatron motion of the particle trajectory due to dispersion can be written as

$$\Delta x = D_x \frac{\Delta p}{p}. \tag{5.6}$$

The change in revolution frequency Δf_0 for one particle with a difference in momentum Δp

is given by

$$\frac{\Delta f_0}{f_0} = \left(\frac{1}{\gamma^2} - \alpha_p\right)\frac{\Delta p}{p} \sim -\alpha_p \frac{\Delta p}{p}, \tag{5.7}$$

where α_p is the momentum compaction factor and γ is the Lorentz factor.

The cavity frequency f_{HF} is per definition a multiple of the revolution frequency.

$$f_{HF} = h f_0 \longrightarrow \frac{\Delta f_{HF}}{f_{HF}} = \frac{\Delta f_0}{f_0}, \tag{5.8}$$

where h is the harmonic number.

Therefore, the expression for the transverse trajectory displacement due to dispersion can be written as

$$\Delta x = D_x \frac{\Delta p}{p} = -\frac{1}{\alpha_p} D_x \frac{\Delta f_{HF}}{f_{HF}}. \tag{5.9}$$

For this set of measurements, PETRA-III was operated with 40-bunch fill pattern with a total current of about 30 mA, which means a bunch current of about 750 µA. With nominal frequency of $f_{HF} = 499.66432$ MHz [37], the frequency was shifted by up to ± 2 kHz. The momentum compaction factor was given as $\alpha_p = 1.221 \cdot 10^{-3}$ [37, 38].

In Section 4.2.6, it was explained that the laser output delay has to be manually adjusted so as to achieve maximum overlap with the particle bunch for a certain PETRA-III operational setting (see Fig. 4.18). In Fig. 5.8, this time shift is plotted against the applied frequency shift. The data was fitted with a linear fit, $f(x) = p_0 + p_1 \cdot x$, the results are $p_1/10 = -9.67 \pm 0.03$ ns $\cdot$ kHz^{-1} and $p_0/10^3 = 2.50 \pm 0.00$ ns.

For each frequency shift, a horizontal profile was taken with two different step sizes for the scanning translation stage (50 and 100 µm). Fig. 5.9 shows the horizontal profile centroids plotted against the frequency shift. The corresponding values for the relative energy change are given in the second axis on top of the plot. The error bars for the centroid data represent a total error $\Delta\mu^{\text{tot}} = \sqrt{(\Delta\mu^{\text{sys}})^2 + (\Delta\mu^{\text{stat}})^2}$. This data was also fitted with a linear fit, the results are $p_1/10^{-1} = -2.30 \pm 0.04$ mm $\cdot$ kHz^{-1} and $p_0 = 11.54 \pm 0.01$ mm.

The proportionality factor can then be used to calculate the local dispersion value,

$$D_x = (-2.30 \pm 0.04) \cdot 10^{-1} \text{ mm} \cdot \text{kHz}^{-1} \cdot f_0 \cdot -\alpha_p = 140.42 \pm 2.51 \text{ mm}.$$

The energy spread of PETRA-III is $\frac{\Delta E}{E} = 1.3 \cdot 10^{-3}$ [37]. The implication of D_x on the measured

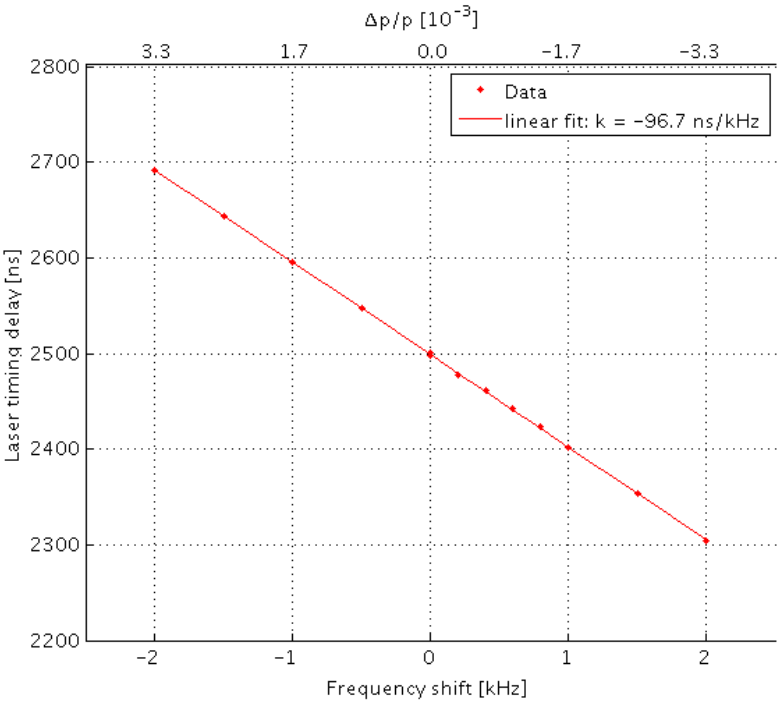

Figure 5.8: Laser timing delay versus frequency shift. The proportionality factor is also given in the legend.

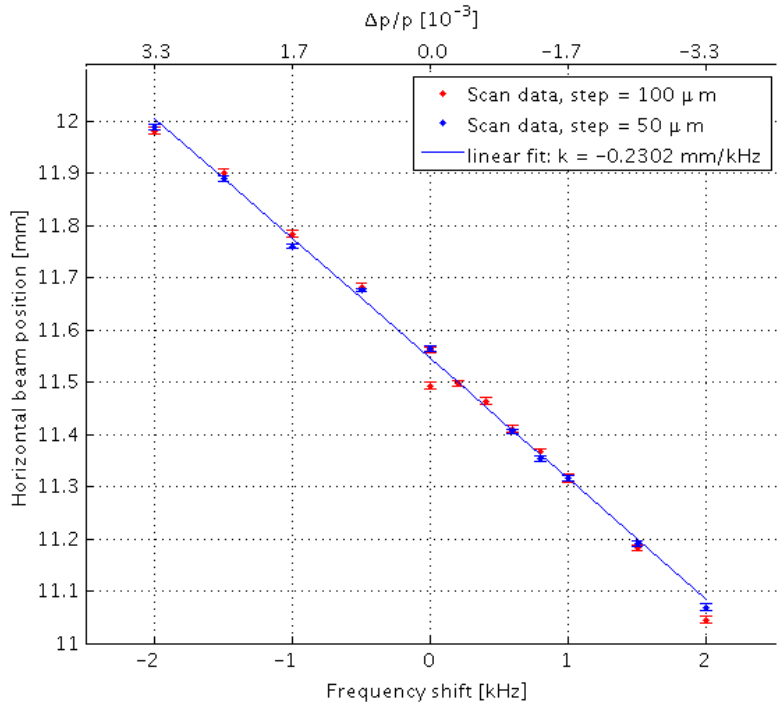

Figure 5.9: Horizontal beam position versus frequency shift. The proportionality factor of the linear fit is given in the legend.

beam size is therefore $D_x \frac{\Delta E}{E} = 182.55 \pm 3.26$ µm. However, the real contribution is considerably smaller due to the square root in Eq. 3.65.

The vertical position was also measured, because of time constraints however, the translation stage step size was set to only 10 µm. The resolution of the transversal scan did therefore not give enough points across the profile to confidently apply the full fit function (see Eq. 4.3). Instead, only the 5 points around the peak were fitted with a simple Gaussian. Fig. 5.10 shows the centroids of the Gaussian peak fits plotted against the frequency shift. The corresponding values for the relative energy change are given in the second axis on top of the plot. This data was also fitted with a linear fit, the results are $p_1 = 3.41 \pm 1.84$ µm $\cdot$ kHz^{-1} and $p_0 = 7.567 \pm 0.001$ mm.

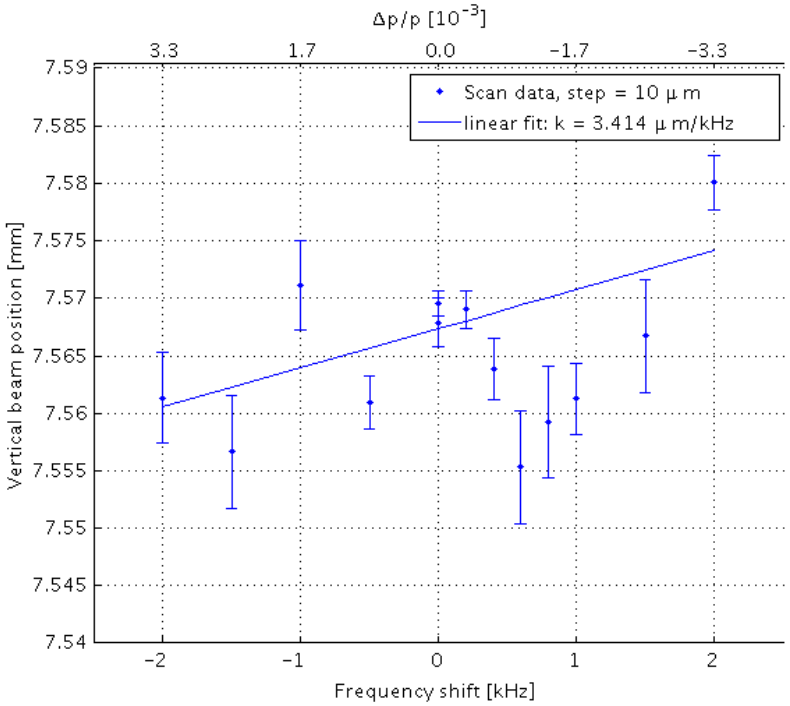

Figure 5.10: Vertical beam position versus frequency shift. The proportionality factor of the linear fit is given in the legend.

With this, the vertical dispersion can be calculated,

$$D_y = 3.41 \pm 1.84 \text{ µm} \cdot \text{kHz}^{-1} \cdot f_0 \cdot -\alpha_p = -2.08 \pm 1.12 \text{ mm}.$$

Taking the energy spread into account, the implication of D_y on the measured beam size is therefore $D_y \frac{\Delta E}{E} = 2.70 \pm 1.46$ µm. Again, the real contribution is considerably smaller due to the square root in Eq. 3.65.

5.5 Conclusions and discussion of discrepancies

Careful studies showed that the discrepancy between the results from the SR imaging system in the PETRA-III diagnostics beam-line and the laser-wire can neither be explained by a possible laser tilt, non-linearities in the laser-wire setup or the measurement nor by an unexpected increase of the laser spot size caused by the vacuum window.

All vertical scan profiles have a visible asymmetry (see Fig. 5.5). Assuming that the electron beam is purely Gaussian, this shape can only derive from the laser pulse, which leads to the conclusion that the laser beam for the vertical scan must in fact have a size comparable to the electron beam size. Furthermore, all laser-wire scans have a consistent minimum of about 20 µm (see Fig. 5.6 and Table 5.1), while the the SR system measured a factor 2 difference between the emittances of Table 5.1 (a) and (b).

From the collision data of the first scan in Table 5.1 (a), the laser size can be estimated. The standard deviation of the the convoluted scan profile is $\sigma_c = 34.65$ µm. The expected electron beam size for a vertical emittance of $\varepsilon_y = 12.33$ pm·rad is $\sigma_e = 15.70$ µm. The estimated laser size is therefore $\sigma_l = \sqrt{{\sigma_c}^2 - {\sigma_e}^2} = 30.89$ µm.

A first step solving these discrepancies would be to measure the laser focus of both lenses with better diagnostics, e.g. a profiler rotating slit laser profiler [39]. Also good input beam size diagnostics are required in order to ensure that the lenses are not overfilled and the laser beam is not clipped. The differences in the vertical and horizontal M^2 show that there are aberrations in the vertical axis. Therefore more laser M^2 diagnostics are required before focusing by the two different lenses.

Possible explanations could also be an unexpected correlation between the horizontal and vertical plane of the electron beam, a large unknown error in the beta functions at the laser-wire location or the time variation of both measurement systems, which are on opposite sides of the ring.

The vertical and horizontal beam sizes were measured while adjusting the orientation of the beam ellipse with skew quadrupoles. For both axes, the beam ellipse was measured to be at its minimum when both skew quadrupoles are set to their default current. Furthermore, the horizontal and vertical dispersion at the laser-wire location were measured by determining the shift of the profile centroid of the transversal beam profile when changing the RF frequency of the machine. The results are $D_x = 140.42 \pm 2.51$ mm and $D_y = -2.08 \pm 1.12$ mm.

Chapter 6

Simulations for the Laser-Wire in the CLIC Drive Beam Transfer Line

For the CLIC project, laser-wire scanners (LWS) would be useful tools for measuring the transverse beam profiles for both, the Main Beam (high energy $9-15$ GeV, low current and very small dimension) and the Drive Beam (low energy $0.24-2.38$ GeV, high current). The use of classic OTR or Cerenkov screens to monitor the transverse beam profiles becomes problematic due to the energy deposited inside the the screens which is high enough to destroy them if the beam size is kept as small as required by the beam transport optimisation. For that reason, a non-invasive diagnostic such as the laser-wire scanner would be a good solution in measuring the beam profiles.

About 20 transverse beam size monitors are needed in the frequency multiplication section of the Drive Beam (see Table 2.3), 6 for the transfer lines (TL) alone. A TL is composed of a matching/dispersive section with bending magnets at the exit and the entrance of the line. In the present design, 2-m long dipole magnets with a 15° deflection angle are used. This chapter presents simulations for a first design of a LWS which would fit in this configuration.

6.1 Transfer Line TL2

The Transfer line 2 (TL2) is the link between the two combiner rings (CR1 and CR2; see Fig. 2.1). It has a total length of 415.1 m and consists of an ejection dogleg from CR1, a transverse Optical Matching Section (OMS1), a long straight section, another transverse Optical

Matching Section (OMS2) section and an injection dogleg into CR2. The long straight section is made up of 40 FODO units and one further quadrupole. Each FODO unit is 8 m long and consists of one focussing and one defocussing quadrupole. The straight section has therefore a total length of 324 m.

Fig. 6.1 depicts the last few FODO units of the straight section (∼45 m) followed by the OMS2 section and the injection dogleg into CR2 (note that the beam comes in from the right.). The blue element after the straight section is bending magnet tl2.bend110. This is a 2 m long, 15° bending magnet and it is planned to be used to separate the laser-wire photons from the electron beam.

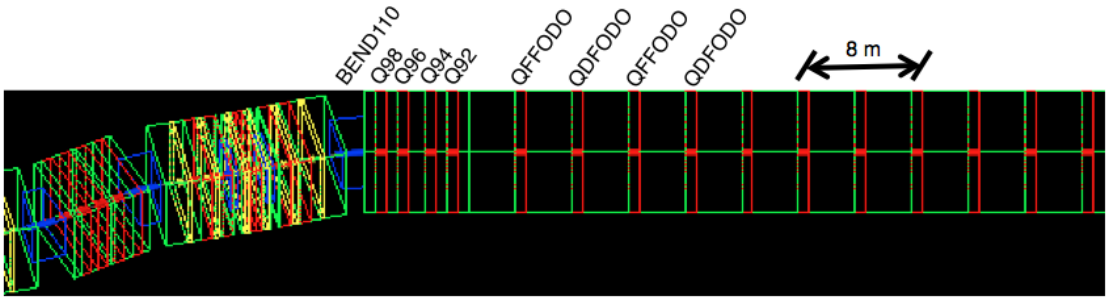

Figure 6.1: BDSIM visualisation of the end of the straight section of TL2 .

6.2 Proposed detector

For detecting the high-energy photons generated from the LW Compton events, a Cerenkov detector similar to the ATF2 laser-wire is considered [39, 40]. The high background in the CLIC Drive-Beam makes need for a detector with a lower detection threshold. A system based on Cerenkov detector is useful in order to differentiate the signal from synchrotron related backgrounds; such a system can also be located in difficult to access positions in the beam-line, with the Cerenkov light directed to photomultipliers situated well away from the beam-line.

The Accelerator Test Facility (ATF) is a test accelerator primarily for damping ring development, but also development of new beam diagnostic devices intended for the ILC. The main parameters of the ATF are given in Table 6.1.

At ATF2, the LW Compton photons leave the beam pipe via a window made of 1-mm thick aluminium, before they hit the detector. The Cerenkov detector consists of four main components:

Table 6.1: ATF parameter list [40].

Parameter	Unit	Value
Beam energy	GeV	1.28
No. of electrons / bunch		1×10^{10}
Bunch frequency	Hz	1.56
Bunch length	ps	30
Vertical emittance ε_y	m·rad	5×10^{-11}
Horizontal emittance ε_x	m·rad	1.6×10^{-9}

1. A 4-mm thick lead converter was placed normal to the LW Compton scattered photon beam.

2. Behind the lead converter sits a layer of SP-15 aerogel, again normal to the LW Compton scattered photon beam. This detector is placed 10 m downstream of the IP. The aerogel has a thickness of 5 mm and a refractive index of 1.015.

3. A periscope deflects visible Cerenkov photons downwards. It consists of two light tight, aluminium coated, mylar lined, square cross-sectioned tubes, which are connected by a triangular cross-sectioned piece.

4. The Cerenkov photons are then detected with a photomultiplier tube (PMT) at the bottom and the signal pulse is digitised by a gated integrating ADC.

Compton-scattered photons from the laser-wire hit the lead converter on the front face of the telescope normal to the surface. Approximately 15% of the photons are converted to e^+e^- pairs in the lead which then pass through the aerogel. A charged particle radiates if its velocity is greater than the local phase velocity of light. So as the e^+e^- pairs traverse the aerogel, they emit Cerenkov radiation in the form of visible light.

The Cerenkov velocity of electrons through SP-15 aerogel can be calculated following [41]. The threshold velocity β_t is $1/n$, and

$$\gamma_t = \sqrt{\frac{1}{1-{\beta_t}^2}}. \tag{6.1}$$

Therefore,

$$\beta_t \gamma_t = \sqrt{\frac{1}{2\delta+\delta^2}}. \tag{6.2}$$

where $\delta = n - 1$ and n is the refractive index. For a refractive index of $n = 1.015$, the Cerenkov threshold is therefore 2.983 MeV.

6.3 Optics simulation using MADX

Modular Accelerator Design X (MADX) is a software tool for processing charged-particle optics in alternating-gradient accelerators and beam lines [42]. This has been used to obtain the beta functions, β_x and β_y, and horizontal dispersion, D_x. As there are no dipole magnets used to bend the electron beam trajectory in the $y-z$ plane, the vertical dispersion, D_y, is equal to zero.

Using these functions, the theoretical beam size can be calculated by

$$\sigma_x = \sqrt{\varepsilon_x \beta_x + \left(D_x \frac{\Delta E}{E}\right)^2} \tag{6.3}$$

$$\sigma_y = \sqrt{\varepsilon_y \beta_y}, \tag{6.4}$$

where $\frac{\Delta E}{E}$ is the RMS momentum spread for the bunch.

In Fig. 6.2 and 6.3, the MADX calculated beam sizes are shown for the last 80 m of the straight section of the transfer line, i.e. the last ten FODO cells. This is the section where the laser-wire most likely will be placed.

6.3.1 Tracking

Comparing the theoretical beam size calculated from the TWISS parameters with MADX with the sigma of the particles tracked with MADX inbuilt Polymorphic Tracking Code (PTC) [43], gives good results. Fig. 6.4 and 6.5 each show the same part of the FODO section of the transfer line, i.e. the last ten FODO cells.

6.4 Optics simulation using BDSIM

BDSIM is a Geant4 [44] based package for simulating particle transport in accelerator beam lines [45]. It can simulate both particle transport through beam lines and also secondary particles from various physics processes when particles hit apertures such as the beam pipe or the pole faces of a magnet.

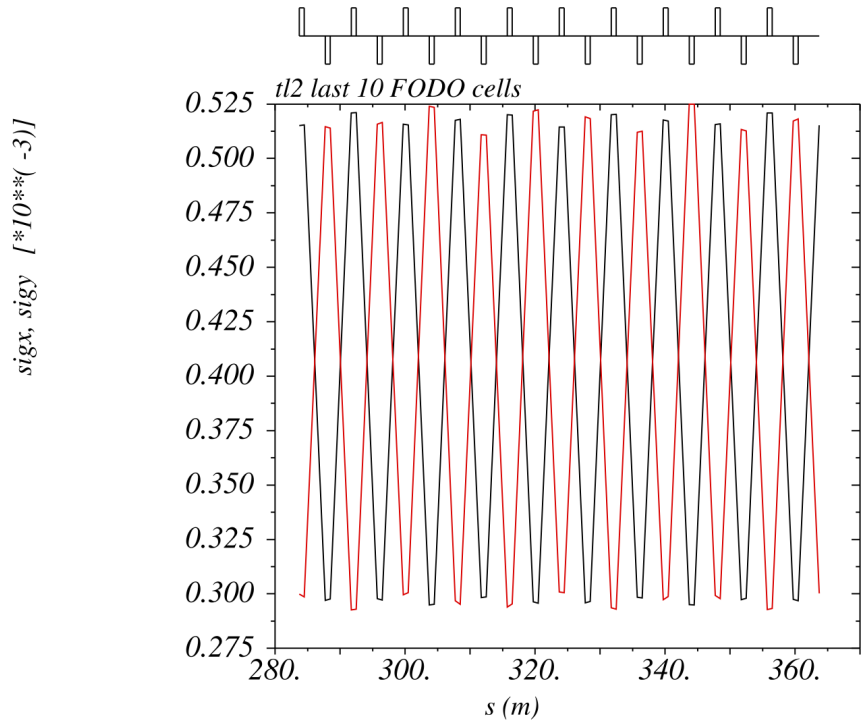

Figure 6.2: Theoretical beam sigma without an energy spread.

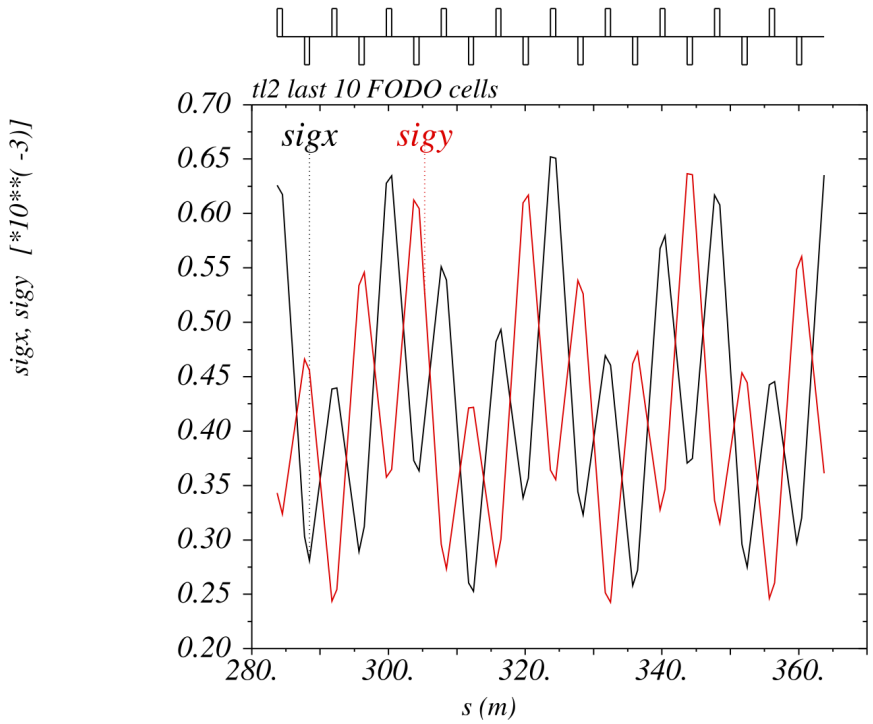

Figure 6.3: Theoretical beam sigma with an energy spread of $\frac{\Delta E}{E} = 0.0033333$.

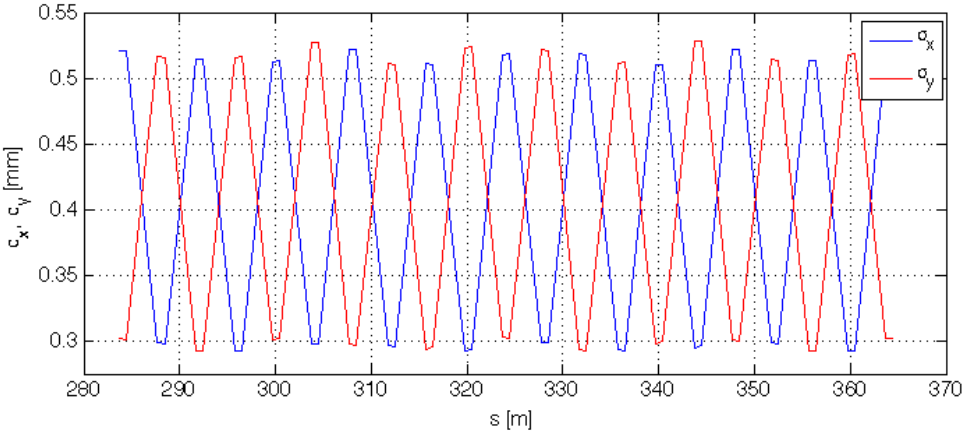

Figure 6.4: Beam sigma of the tracked particles without an energy spread.

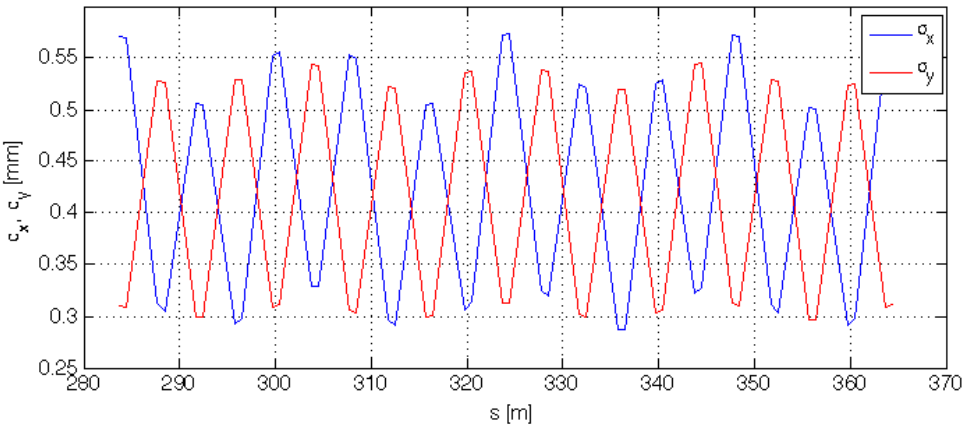

Figure 6.5: Beam sigma of the tracked particles with an energy spread of $\frac{\Delta E}{E} = 0.0033333$.

Fig. 6.6 shows the energy distribution of the generated electrons at the injection of the transfer line. An inverse Compton scattering event was simulated for each electron. The energy distributions of the electrons and the Compton photons after the scattering are presented in Fig. 6.7 and 6.8. In Fig. 6.7, only the Compton-scattered electrons are shown, most of the electrons have the original distribution. The maximum number of detected Compton photons is 619.2 per bunch with a bunch population of $N_{e^-} = 5.2 \times 10^{10}$ e^- (see Section 6.5.1).

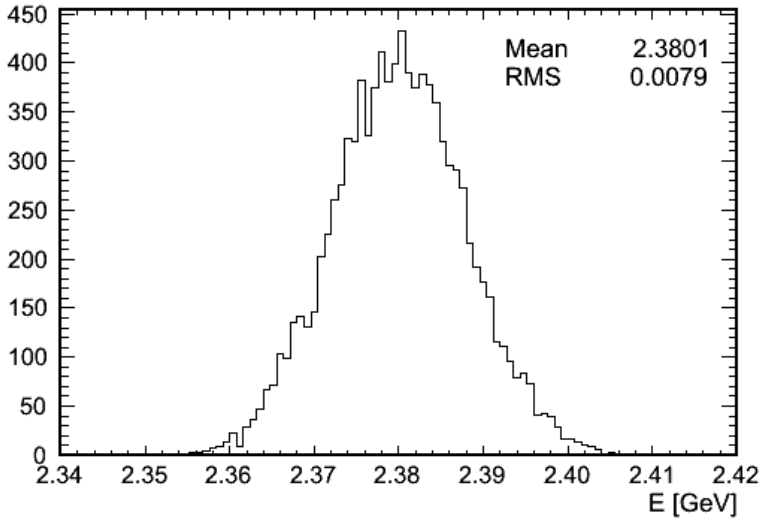

Figure 6.6: Energy distribution of the electrons at injection.

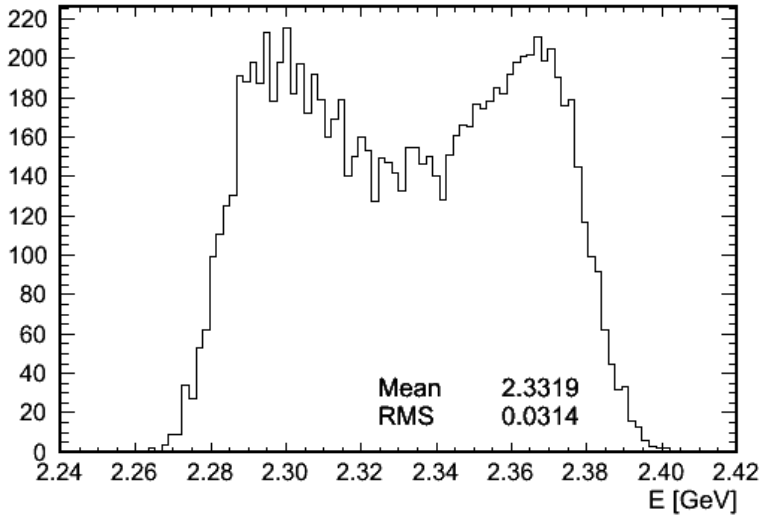

Figure 6.7: Energy distribution of the Compton-scattered electrons after the laser IP.

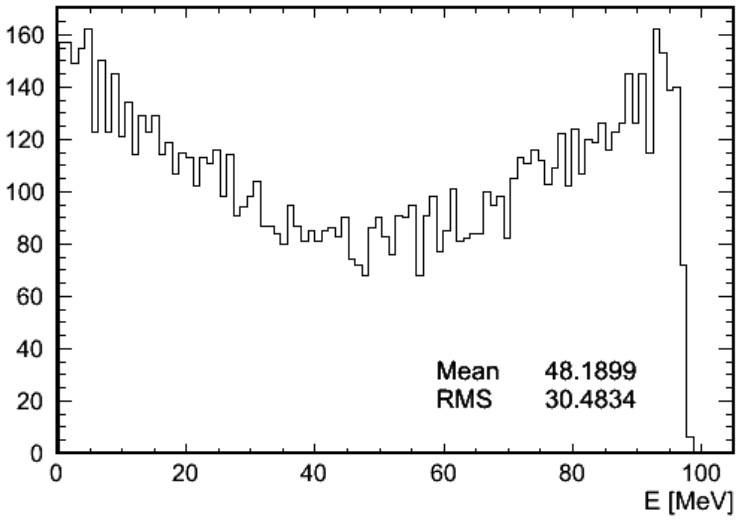

Figure 6.8: Energy distribution of the Compton photons.

6.5 Simulations

6.5.1 Laser-wire Compton rates

The Compton cross-section, σ_C, decreases with increasing electron beam energy. It is related to the Thomson cross-section, $\sigma_T = 0.665 \times 10^{28}$ m^2, by $\sigma_C = \sigma_T f(\omega)$, with $f(\omega)$ calculated as in Eq. 3.86 where $\omega = \frac{hcE_b}{\lambda m_e{}^2 c^4}$ is the normalised photon energy in the rest frame of the electron. For an electron beam energy of $E_b = 2.38$ GeV and a laser wavelength of $\lambda = 1064$ nm, this factor results in $f(\omega) = 0.979$.

The normalised transverse beam emittance in the CLIC drive-beam is estimated to $\gamma\varepsilon = 100\pi$ μm·rad [46]. The beam has a typical transverse size of $\sigma_e = 400$ μm.

The laser is assumed to have a quality factor of $M^2 = 1.3$ and the optics to have an f-number of $f_\# = 20$. This leads to a minimum laser spot size of $\sigma_l = 27.66$ μm and a Rayleigh range of $x_R = 6.95$ mm. Because this is about seventeen times the transverse beam size, the Rayleigh range can be considered as infinite. The number of Compton photons produced, $N(\Delta_y)$, is proportional to the overlap integral, $\varepsilon(\Delta_y)$ (see Eq. 3.126).

$$N(\Delta_y) = N_0 \varepsilon(\Delta_y) \tag{6.5}$$

$$= \frac{N_{det}}{\sqrt{2\pi}\sigma_m} \exp\left[-\frac{\Delta_y{}^2}{2\sigma_m{}^2}\right]. \tag{6.6}$$

with

$$N_{det} = 1212 \times \frac{\eta}{0.05} \frac{P_l}{10\ \text{MW}} \frac{N_e}{2 \times 10^{10}} \frac{\lambda}{532\ \text{nm}} \frac{f(\omega)}{0.2}\ \mu\text{m}. \tag{6.7}$$

The width of the of the convoluted signal is $\sigma_m = \sqrt{{\sigma_e}^2 + {\sigma_l}^2} = 400.96\ \mu$m. With an electron bunch population of $N_{e^-} = \frac{8.4\ \text{nC}}{e} = 5.2 \times 10^{10}\ \text{e}^-$ and assuming an instantaneous laser power of $P_l = 100$ MW at the laser-wire IP and a total detector efficiency of $\eta = 10\%$, the maximum number of detected Compton photons is 619.2 [21]. In Fig. 6.9, a scan profile is shown.

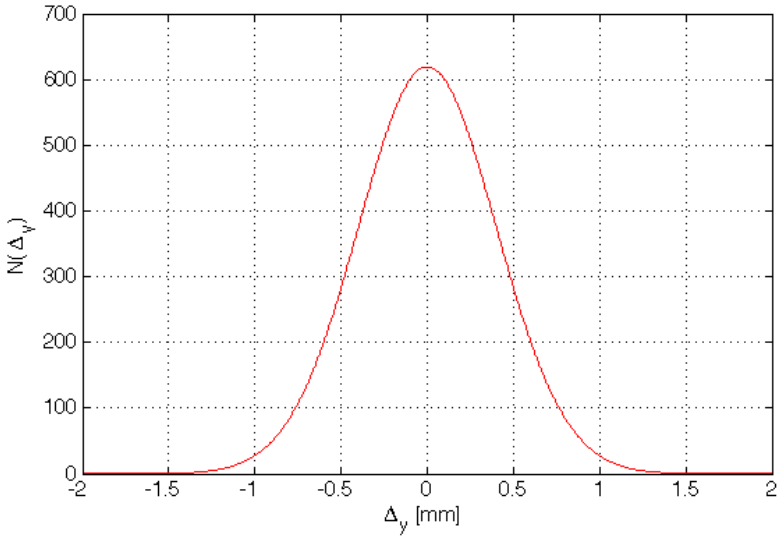

Figure 6.9: Scan profile at the laser-wire IP for a laser with $M^2 = 1.3$ and wavelength $\lambda = 1064$ nm. The electron bunch is assumed to have a Gaussian transverse profile with $\sigma_e = 400\ \mu$m.

The ATF2 Cerenkov detector has a detection efficiency of approximately 15% (see Section 6.2). Therefore, a detection efficiency of $\eta = 10\%$ is a conservative assumption for the detector at TL2, but depends on the background spectrum and rate.

6.5.2 Angular distribution

The energy dependence of the scattered photons on angular distribution is given by (see [47])

$$h\nu_{sc} = h\nu_0 * \left(\frac{\gamma_0 m_e c^2 (1 - \beta_0 \cos(\psi))}{\gamma_0 m_e c^2 (1 - \beta_0 \cos(\theta)) + h\nu_0 (1 - \cos(\psi - \theta))} \right). \tag{6.8}$$

In the case of the laser-wire, the collision angle is $\pi = 90^\circ$. The maximum photon energy is emitted in the forward direction ($\theta = 0^\circ$) and can be expressed as $h\nu_{sc,max} = \frac{h\nu_0 \gamma_0 m_e c^2}{h\nu_0 + \gamma_0 m_e c^2 (1 - \beta_0)}$.

The critical angle of the scattered flux is given by

$$\alpha_c = \sqrt{1+2\omega}. \tag{6.9}$$

Using the values for the CLIC Drive-Beam transfer line, these quantities compute to $h\nu_{sc,max} =$ 49.5 MeV and $\alpha_c = 21.7$ mrad. Considering a beam pipe radius of 4 cm [46], the distance between IP and detection can be 184.4 m before most of the photons get lost. The angular distribution of the scattered photons can be seen in Fig. 6.10.

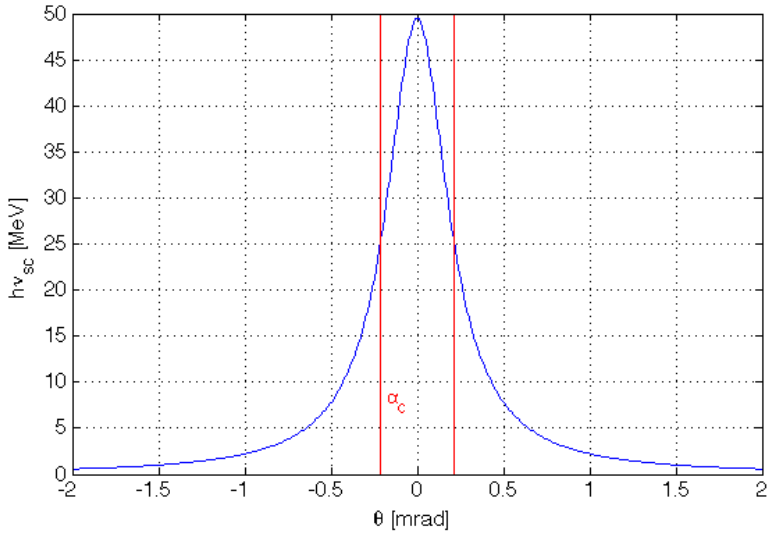

Figure 6.10: Evolution of the energy of the scattered photons as a function of the observation angle. The vertical red lines represent the critical angle (see Eq. 6.9).

6.5.3 Separating the Compton photons

The length S of an arc of a circle with radius R and subtending an angle θ with the circle centre is defined as $S = \theta R$. The chord L is given by

$$L = 2R\sin\frac{\theta}{2} \tag{6.10}$$

$$= 2\frac{S}{\theta}\sin\frac{\theta}{2} \tag{6.11}$$

For bending magnet labelled tl2.bend110, the chord is 2 m and the bending angle is 15°. The actual arc length is therefore 2.0057 m, which results in a radius of $R = 7.66$ m.

To calculate, how much the bending magnet separates the Compton photons from the electron, the following geometrical relation has to be considered (see Fig. 6.11):

$$\begin{aligned} \cos\theta &= \frac{R}{R+d} \\ \rightarrow d &= \frac{R}{\cos\theta} - R \\ &= 7.93\ \text{m} - 7.66\ \text{m} \\ &= 0.2703\ \text{m} = 27.03\ \text{cm} \end{aligned}$$

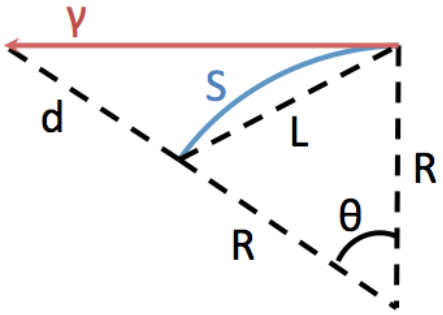

Figure 6.11: Sketch illustrating the photon separation.

By the end of the bending magnet, the Compton beam will be separated from the electron beam by 27.03 cm. The aperture of the bending magnet is foreseen to be rectangular with a flat pole face and a width of $40-60$ cm. For the separation distance to be well within the aperture of the bending magnet, the magnet width therefore has to be at the upper end of this scale. Then, a Y-shaped vacuum pipe can be installed.

In order to confirm the calculated separation with the simulated beam, the horizontal distributions of electrons and photons before the separating bending magnet and photons after the bending magnet are shown in Fig. 6.12, 6.13 and 6.14 respectively.

6.5.4 Signal detection efficiency

Fig. 6.15 shows the efficiency plot for Compton detection when moving the position of the laser IP progressively further away from the entrance of the separating bending magnet. Only scattered photons which are contained within the beam pipe at that position were counted.

Introducing a lower-energy Cerenkov threshold only makes a difference for short distances

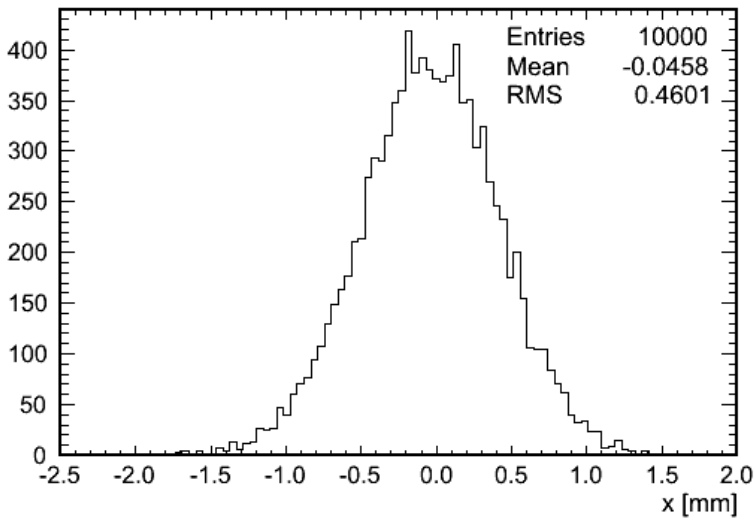

Figure 6.12: Horizontal distribution of the electrons before the bending magnet.

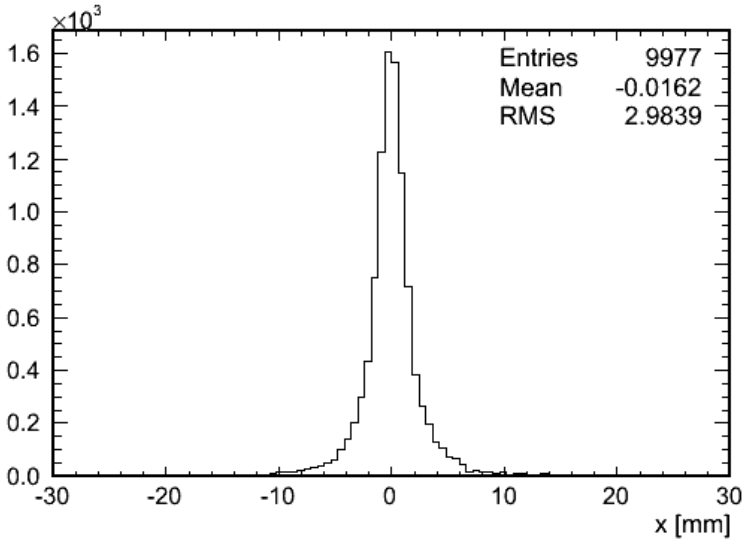

Figure 6.13: Horizontal distribution of the photons before the bending magnet with respect to the beam centroid.

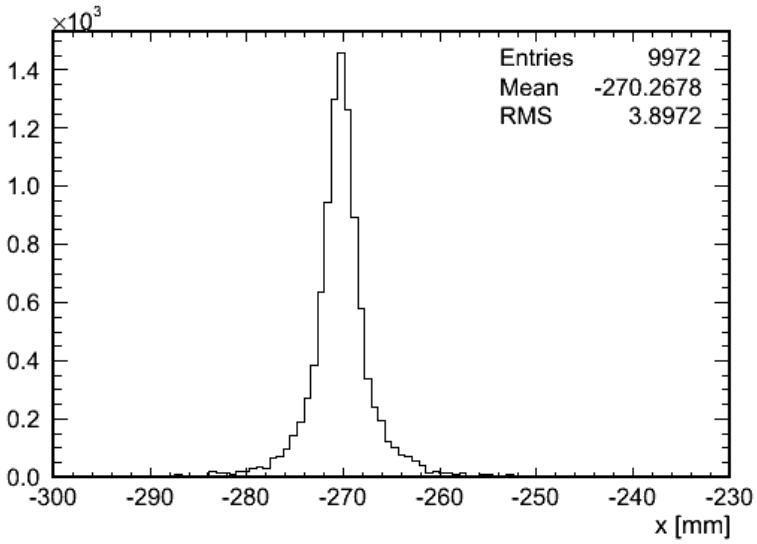

Figure 6.14: Horizontal distribution of the photons after the bending magnet with respect to the beam centroid.

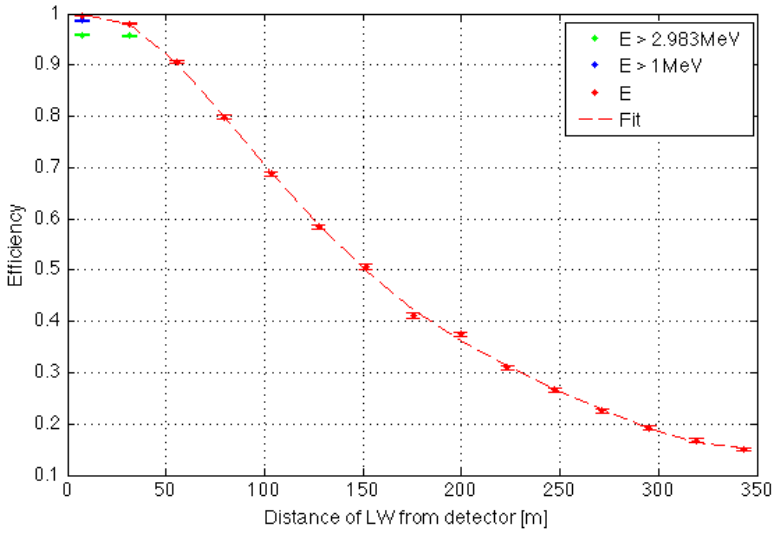

Figure 6.15: Efficiency of Compton detection over distance for all energies, $E > 1$ MeV and $E > 2.983$ MeV.

as those photons are scattered at larger angles and hit the beam pipe earlier. Fig. 6.15 shows the efficiency plot for two different thresholds: $E > 1$ MeV which is needed for pair-production before the Cerenkov detector and $E > 2.983$ MeV which is the threshold for the Cerenkov counter at ATF2.

6.5.5 Energy loss

The energy loss per metre due to laser-wire Compton photons is shown in Fig. 6.16. The x-axis shows the position along the transfer line. The laser was placed right at the beginning of the straight FODO section ($s = 43.7$ m), $20 \cdot 10^3$ photons were used in this simulation. The energy loss is displayed until the photons are separated from the electrons by the bending magnet at $s = 375.1$ m, after which they hit the detector.

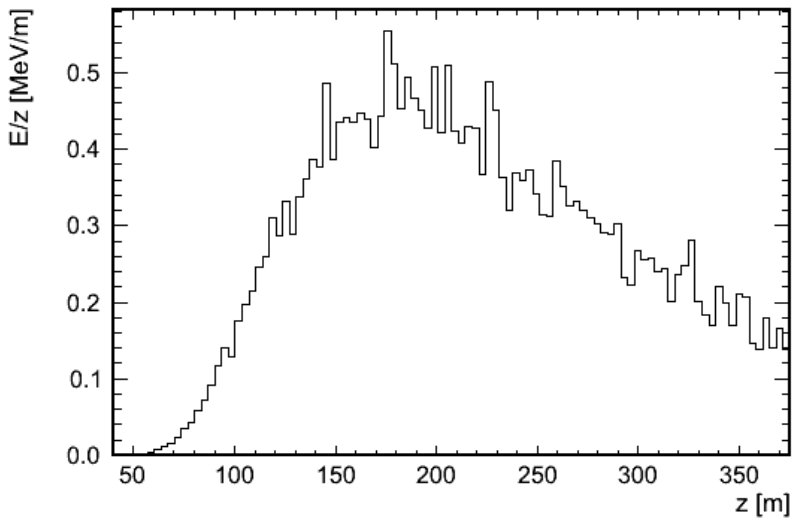

Figure 6.16: Energy loss per metre of the Compton photons normalised to one Compton event.

6.5.6 Background from beam-gas bremsstrahlung

An interaction between an incoming electron and a beam-gas molecule in the beampipe can be approximated by a hardshell model. The cross-section of an individual scattering is therefore given by $\sigma_i = {r_{mol}}^2 \pi$, where r_{mol} is the radius of the beam-gas molecule. The total cross-section of all molecules contained within a beampipe of length l and size A can then be written as

$$\sigma_{tot} = \sigma_i l A \rho \tag{6.12}$$

with ρ being the number density of beam-gas molecules. An incoming electron beam can described as a flux of particles, $f_{e^-} = \frac{N_{e^-}}{A(\Delta t)}$. The scattering rate then simply becomes

$$R_s = f_{e^-}\sigma_{tot} = \frac{N_{e^-}}{A(\Delta t)}\sigma_i l A \rho = R_{e^-}\sigma_i l \rho. \tag{6.13}$$

From the ideal gas law, $pV = nk_BT$, where p is the pressure and V the volume. The number density is given by $\rho = \frac{n}{V} = \frac{p}{k_BT}$. With this, the fraction of scattered electrons can be expressed as

$$\frac{R_s}{R_{e^-}} = \frac{N_s}{N_{e^-}} = \sigma_i l \frac{p}{k_BT}. \tag{6.14}$$

Estimating the background from beam gas bremsstrahlung can also be done following [22]. The straight section of the transfer line is $D = 400$ m long. The cross-section for bremsstrahlung off N_2 or CO gas is estimated to be $\sigma_B \approx 5.51^{-28}$ m^2 when the scattering cut-off is set to 1% of the beam energy. Assuming a vacuum pressure of $P = 10$ nTorr and a temperature of $T = 293$ K, the number of background events per electron bunch is $\frac{DPN_e\sigma_B}{k_BT}$ which gives about 4 bremsstrahlung photons per bunch. The nominal signal is 619.2 detected Compton photons per bunch, which is well above this background (see Section 6.5.1).

6.5.7 Measurement sensitivity

For a laser-wire scan, the relationship between the number of detected Compton photons N_γ and measured beam size σ_m is as follows:

$$N_\gamma \propto \frac{\eta}{\sigma_m}, \tag{6.15}$$

where η is the detection efficiency. For simulations presented here, only the measurement of the horizontal beam size $\sigma_m = \sigma_{m,x}$ was studied. Therefore, the measured beam size is defined as

$$\sigma_{m,x} = \sqrt{\varepsilon_x\beta_x + \left(\frac{\Delta E}{E}\right)^2 {D_x}^2} \tag{6.16}$$

with horizontal beta function β_x, horizontal dispersion D_x, horizontal emittance ε_x and energy spread $\frac{\Delta E}{E}$.

The horizontal and vertical beta functions and the horizontal dispersion over the last 100 m of the straight section of the transfer line TL2 are shown in Fig. 6.17. The resulting horizontal

and vertical beam sizes over the same distance are plotted in Fig. 6.18.

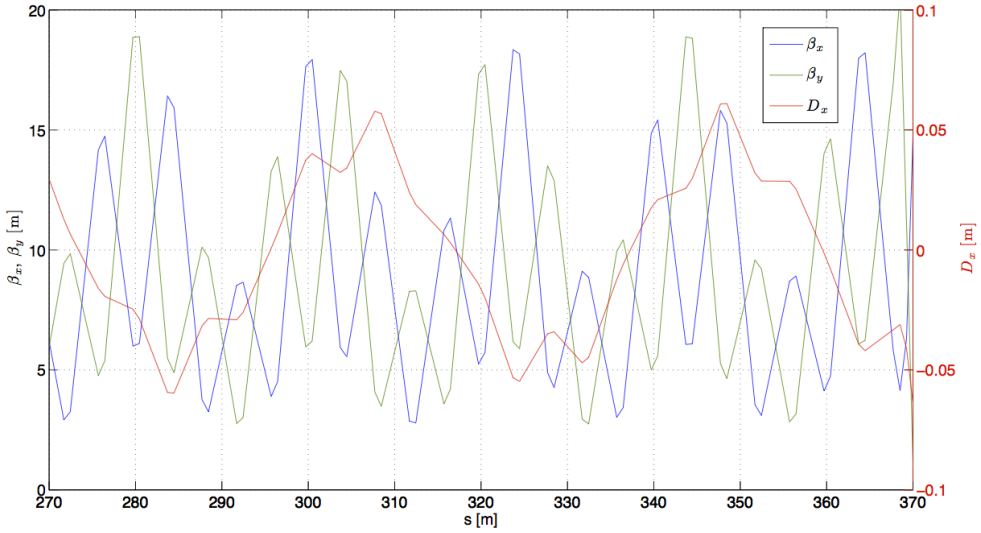

Figure 6.17: Beta functions and horizontal dispersion over the last 100 m of the straight section in TL2.

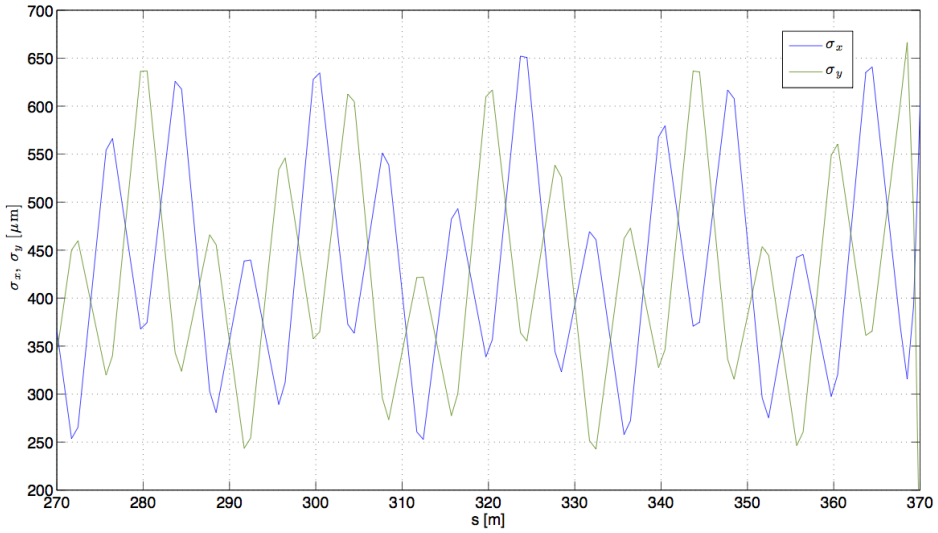

Figure 6.18: Theoretical beam size $\sigma_{x,y}$ over the last 100 m of the straight section in TL2.

The error of a beam size measurement with respect to a parameter of interest X, e.g. $X = \varepsilon_x$ or $\frac{\Delta E}{E}$, goes as

$$\Delta\sigma_x = \left|\frac{\partial\sigma_x}{\partial X}\right| \Delta X.$$

The statistical error of the measurement however follows

$$\frac{\Delta\sigma_x}{\sigma_x} \propto \frac{1}{\sqrt{N}}.$$

Therefore, in order to find the best measurement location, the following function has to be maximised,

$$\sqrt{N}\left|\frac{\partial\sigma_x}{\partial X}\right| = \sqrt{\frac{\eta}{\sigma_x}}\left|\frac{\partial\sigma_x}{\partial X}\right|. \tag{6.17}$$

In Fig. 6.19, the sensitivity of the beam size measurement with respect to the horizontal emittance and the energy spread is shown over the last 100 m of the straight section in TL2. This plot does not take the detector efficiency into account.

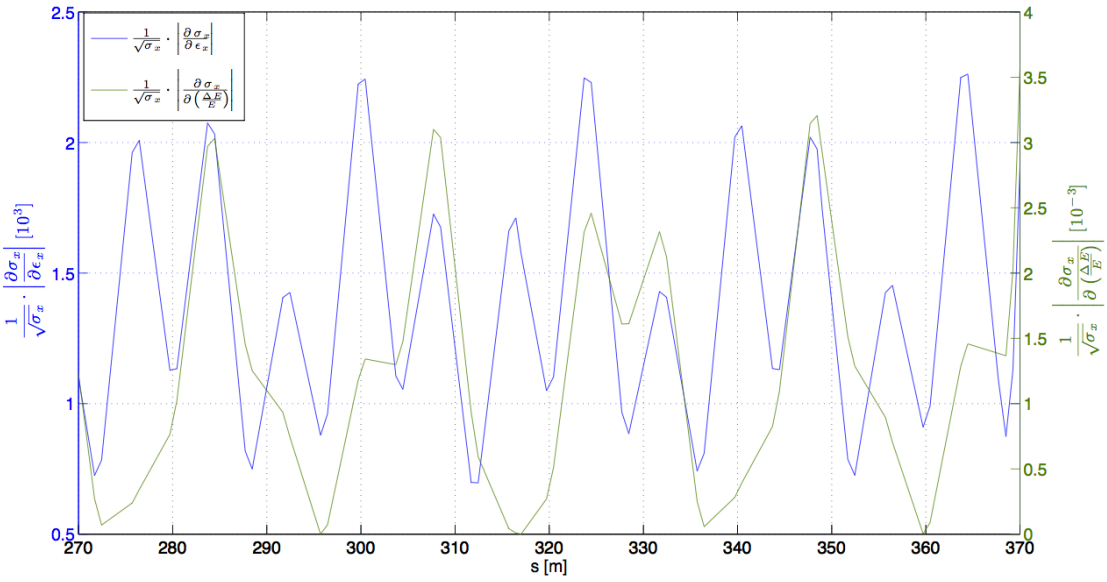

Figure 6.19: Sensitivity of the beam size measurement with respect to the horizontal emittance and the dispersion over the last 100 m of the straight section in TL2.

The theoretical detection efficiency over the last 100 m is shown in Fig. 6.20 (see Sec. 6.5.4). This is used to calculate the effective sensitivity of the beam size measurement with respect to the horizontal emittance and the dispersion given in Eq. 6.17, which is plotted in Fig. 6.21.

6.5.8 Finding a laser-wire location

The laser-wire at the transfer line TL2 would primarily be used for two types of measurements: emittance and energy spread, as these are beam related parameters. The beta function and the dispersion are defined by the optics and will most probably be measured some other way. Therefore, to select the best possible position for either type of measurement, the following requirements should be met:

1. Emittance: $\sqrt{\frac{\mathrm{Eff}}{\sigma_x}} \times \left|\frac{\partial\sigma_x}{\partial\varepsilon_x}\right| = \max,\ D_x = 0$

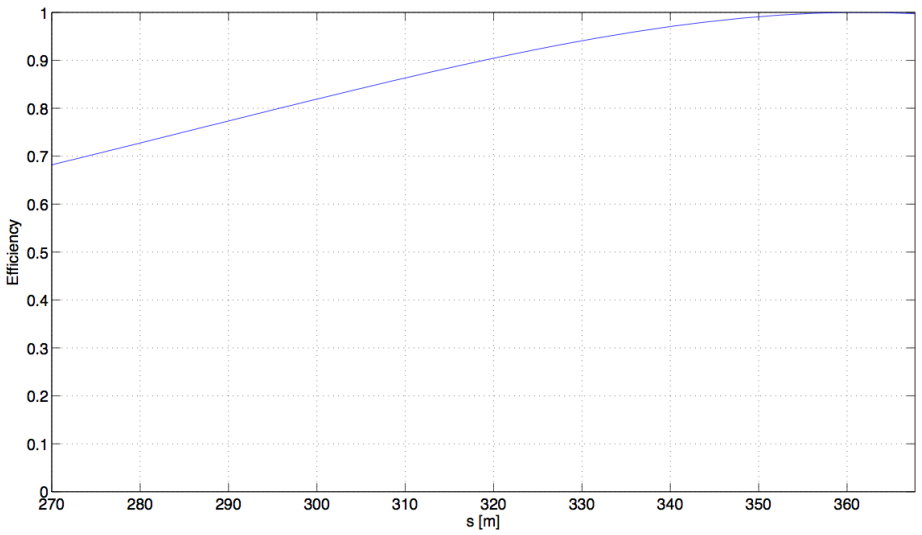

Figure 6.20: Theoretical detection efficiency over the last 100 m of the straight section in TL2.

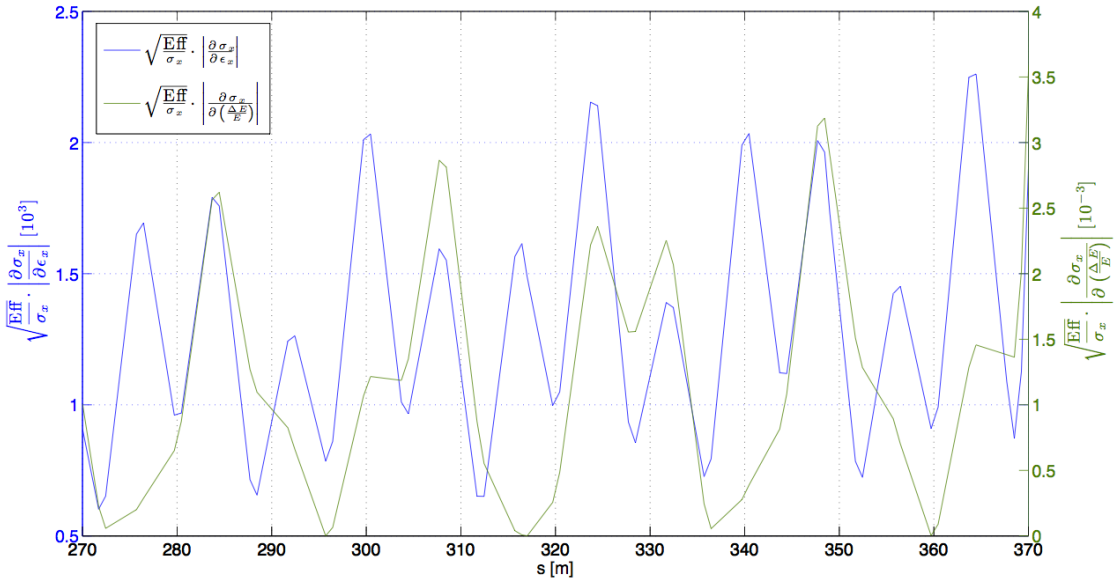

Figure 6.21: Effective sensitivity of the beam size measurement with respect to the horizontal emittance and the energy spread.

2. Energy spread: $\sqrt{\frac{\mathrm{Eff}}{\sigma_x}} \times \left| \frac{\partial \sigma_x}{\partial \left(\frac{\Delta E}{E} \right)} \right| = \max, \beta_x = \min$

Therefore, to find the optimum location for an emittance measurement, Fig. 6.22 has to be considered. In order to select the best location for an energy spread measurement, Fig. 6.23 must be referred to.

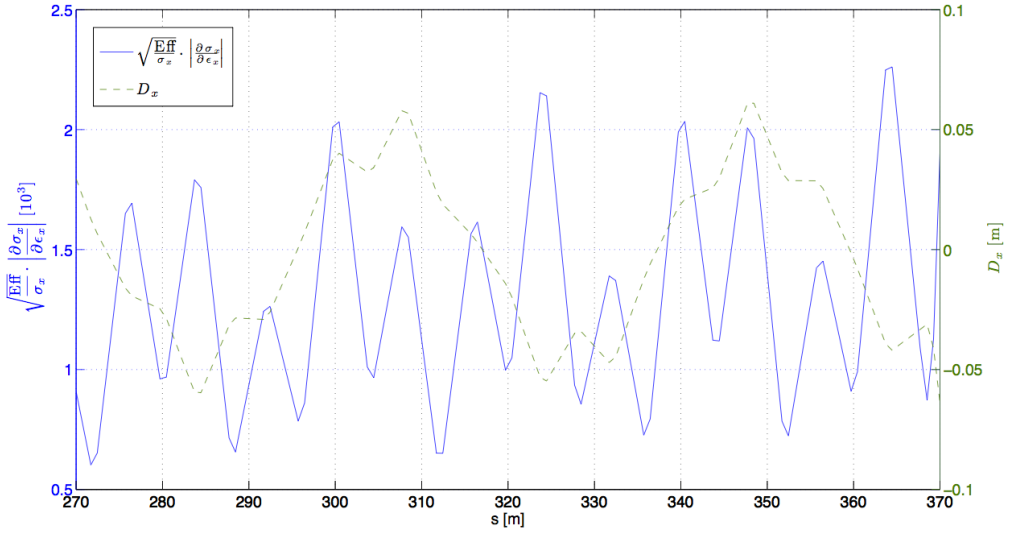

Figure 6.22: Horizontal dispersion and effective sensitivity of the beam size measurement with respect to the horizontal emittance.

6.5.8.1 Emittance measurement

From Eq. 6.16, emittance can be expressed as

$$\varepsilon_x = \frac{1}{\beta_x} \left({\sigma_x}^2 - \left(\frac{\Delta E}{E} \right)^2 {D_x}^2 \right). \tag{6.18}$$

The emittance error $\Delta\varepsilon_x$ at a location where $D_x = 0$ then calculates to

$$(\Delta\varepsilon_x)^2 = \left(\frac{\partial \varepsilon_x}{\partial \beta_x} \Delta\beta_x \right)^2 + \left(\frac{\partial \varepsilon_x}{\partial \sigma_x} \Delta\sigma_x \right)^2 \tag{6.19}$$

$$= \left(-\frac{\varepsilon_x}{\beta_x} \Delta\beta_x \right)^2 + \left(\frac{2\sigma_x}{\beta_x} \Delta\sigma_x \right)^2 \tag{6.20}$$

Zooming into Fig. 6.22, a possible location for a laser-wire setup measuring the horizontal emittance can be determined. The LW would be placed in a drift section, 0.5624 m after a focussing quadrupole. The location is marked with a vertical red line in Fig. 6.24 and the values

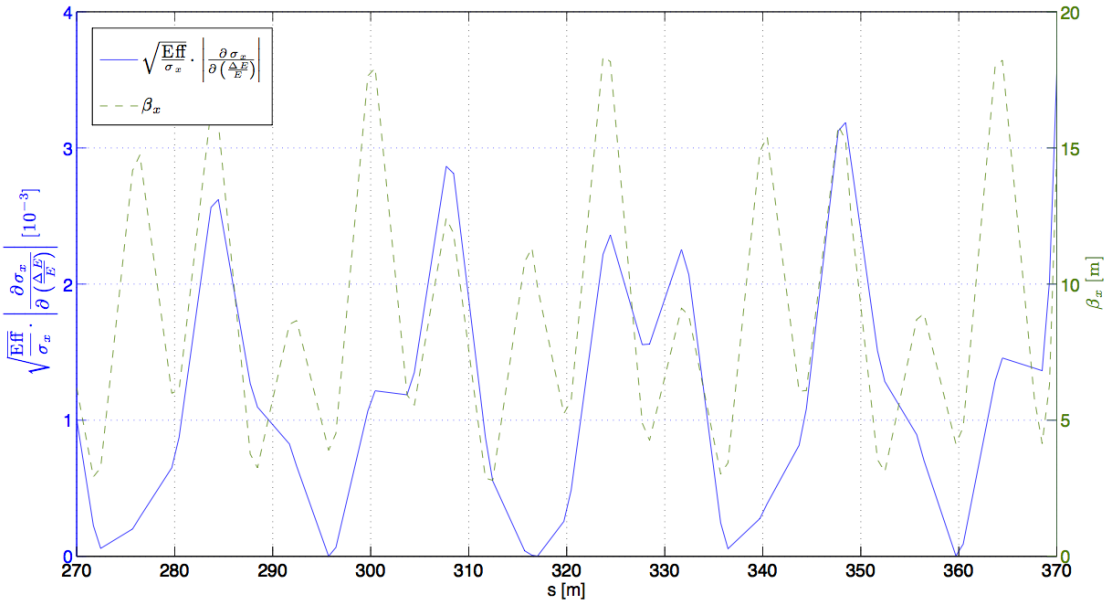

Figure 6.23: Horizontal beta function and effective sensitivity of the beam size measurement with respect to the energy spread.

for β_x, D_x and σ_x are given in the plot.

Typical beam scans at PETRA-III measured horizontal sizes of the order of 220 ± 4 µm (see Section 4.2.7.5). The relative beam size measurement error is therefore $\frac{\Delta\sigma_x}{\sigma_x} = 1.8\%$ These scans were typically of 50 µm resolution and took between 1 and 2 minutes. Using the values for the proposed LW location in Fig. 6.24, the contribution from a beam size measurement error with scan settings similar to PETRA-III would be

$$\frac{\partial \varepsilon_x}{\partial \sigma_x} \Delta\sigma_x = \frac{2 \cdot 461.01\ \mu\mathrm{m}}{9.9\ \mathrm{m}} \cdot (461.01\ \mu\mathrm{m} \cdot 1.8\%) = 772.84\ \mathrm{pm} \cdot \mathrm{rad}.$$

In order to prevent the emittance error to be dominated by a beta measurement error, the contribution from a beta measurement error is be limited to 10% of the contribution from the beam size measurement error.

$$\begin{aligned} \frac{\partial \varepsilon_x}{\partial \beta_x} \Delta\beta_x &= \frac{\partial \varepsilon_x}{\partial \sigma_x} \Delta\sigma_x \cdot 0.1 \\ -\frac{21.47\ \mathrm{nm} \cdot \mathrm{rad}}{9.9\ \mathrm{m}} \cdot \Delta\beta_x &= 77.28\ \mathrm{pm} \cdot \mathrm{rad} \\ \longrightarrow \Delta\beta_x &= -35.64\ \mathrm{mm} \\ \frac{\Delta\beta_x}{\beta_x} &= -3.60 \cdot 10^{-3} \end{aligned}$$

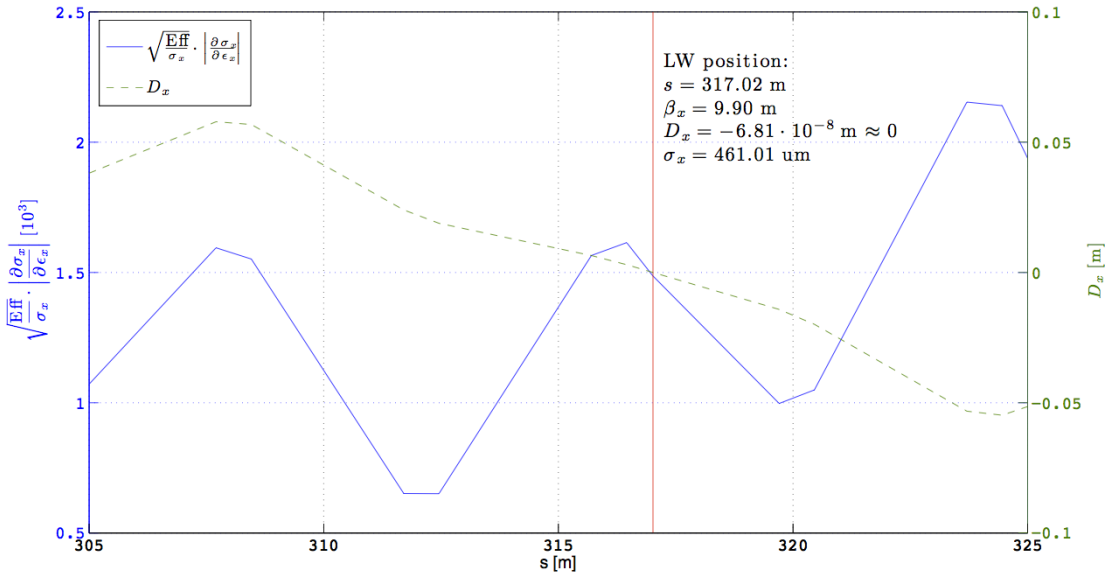

Figure 6.24: Proposed location for a laser-wire experiment, optimised for measuring the horizontal emittance.

The total emittance error can then be calculated to

$$\begin{aligned} \Delta\varepsilon_x &= \sqrt{(772.84\ \text{pm}\cdot\text{rad})^2 + (77.28\ \text{pm}\cdot\text{rad})^2} = 776.69\ \text{pm}\cdot\text{rad} \\ \frac{\Delta\varepsilon_x}{\varepsilon_x} &= 3.62\cdot 10^{-2} \end{aligned}$$

Table 6.2 summarises the theoretical parameter values and the allowed absolute and relative measurement errors at the laser-wire location.

Table 6.2: Parameter values and errors for the emittance measurement.

Parameter	Theoretical value	Allowed error	
		absolute	relative
β_x	9.90 m	35.64 mm	0.36%
σ_x	461.01 µm	8.39 µm	1.82%
ε_x	21.47 nm·rad	776.69 pm·rad	3.62%

6.5.8.2 Energy spread measurement

From Eq. 6.16, energy spread can be expressed as

$$\frac{\Delta E}{E} = \frac{1}{D_x}\sqrt{\varepsilon_x\beta_x - \sigma_x{}^2}. \tag{6.21}$$

The energy spread error $\Delta\left(\frac{\Delta E}{E}\right)$ at any location is then determined by

$$\begin{aligned}\left(\Delta\left(\frac{\Delta E}{E}\right)\right)^2 &= \left(\frac{\partial\left(\frac{\Delta E}{E}\right)}{\partial D_x}\Delta D_x\right)^2 + \left(\frac{\partial\left(\frac{\Delta E}{E}\right)}{\partial \varepsilon_x}\Delta\varepsilon_x\right)^2 + \dots \\ &\quad + \left(\frac{\partial\left(\frac{\Delta E}{E}\right)}{\partial \beta_x}\Delta\beta_x\right)^2 + \left(\frac{\partial\left(\frac{\Delta E}{E}\right)}{\partial \sigma_x}\Delta\sigma_x\right)^2 \\ &= \left(-\frac{1}{D_x}\left(\frac{\Delta E}{E}\right)\Delta D_x\right)^2 + \left(\frac{\beta_x}{2{D_x}^2}\left(\frac{\Delta E}{E}\right)^{-1}\Delta\varepsilon_x\right)^2 + \dots \\ &\quad + \left(\frac{\varepsilon_x}{2{D_x}^2}\left(\frac{\Delta E}{E}\right)^{-1}\Delta\beta_x\right)^2 + \left(-\frac{\sigma_x}{{D_x}^2}\left(\frac{\Delta E}{E}\right)^{-1}\Delta\sigma_x\right)^2\end{aligned}$$

Zooming into Fig. 6.23, a possible location for a laser-wire setup measuring the energy spread can be determined. Again, the location is marked with a vertical red line in Fig. 6.25 and the values for β_x, D_x and σ_x are given in the plot.

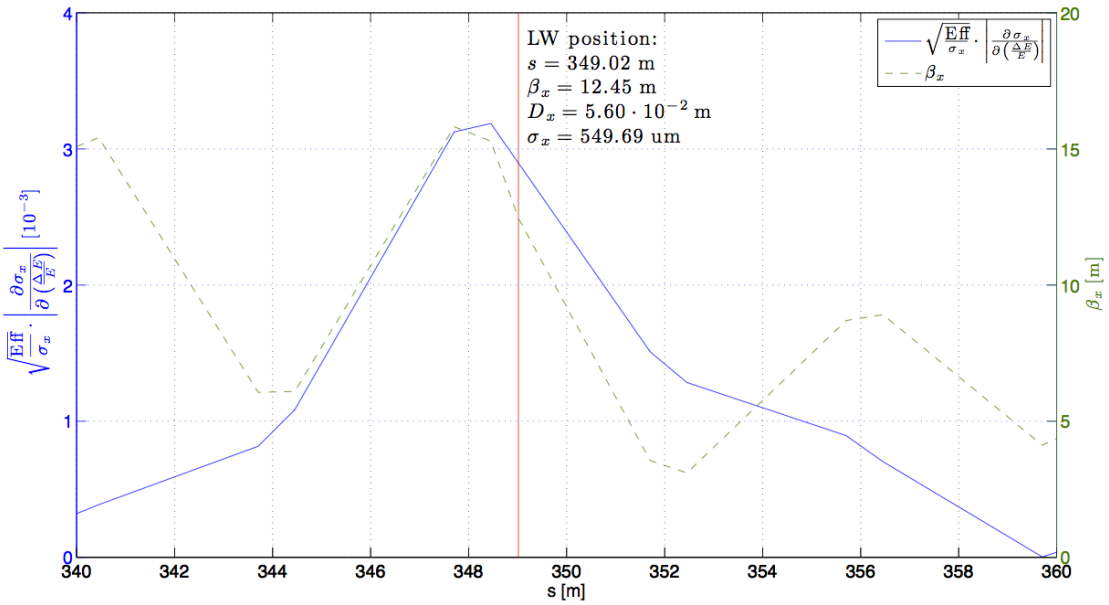

Figure 6.25: Proposed location for a laser-wire experiment, optimised for measuring the energy spread.

The maximum sensitivity for an energy spread measurement is at the end of a focusing quadrupole, therefore the location was moved further downstream into the drift section. The distance was kept the same as for the emittance measurement.

For a given energy spread of $\frac{\Delta E}{E} = 3.333 \cdot 10^{-3}$ and for a similar setup as before, the contribution from a beam size measurement error using the values in Fig. 6.25 can be calculated

as

$$\frac{\partial\left(\frac{\Delta E}{E}\right)}{\partial\sigma_x}\Delta\sigma_x = -\frac{549.69\ \mu\text{m}}{(5.60\cdot 10^{-2}\ \text{m})^2}\cdot\left(3.333\cdot 10^{-3}\right)^{-1}\cdot(549.69\ \mu\text{m}\cdot 1.8\%) = -5.204\cdot 10^{-4}.$$

With measurement errors on β_x and ε_x as determined above (see Table 6.2), the contributions from a beta or emittance measurement error can also be determined

$$\begin{aligned}\frac{\partial\left(\frac{\Delta E}{E}\right)}{\partial\varepsilon_x}\Delta\varepsilon_x &= \frac{12.45\ \text{m}}{2\cdot(5.60\cdot 10^{-2}\ \text{m})^2}\cdot\left(3.333\cdot 10^{-3}\right)^{-1}\cdot(21.47\ \text{nm}\cdot\text{rad}\cdot 3.62\%) = 4.629\cdot 10^{-4}\\ \frac{\partial\left(\frac{\Delta E}{E}\right)}{\partial\beta_x}\Delta\beta_x &= \frac{21.47\ \text{nm}\cdot\text{rad}}{2\cdot(5.60\cdot 10^{-2}\ \text{m})^2}\cdot\left(3.333\cdot 10^{-3}\right)^{-1}\cdot(12.45\ \text{m}\cdot -0.36\%) = -4.603\cdot 10^{-5}\end{aligned}$$

Similar to the derivation above, the contribution from the dispersion error is required to be 10% of the contribution from the beam size measurement.

$$\begin{aligned}\frac{\partial\left(\frac{\Delta E}{E}\right)}{\partial D_x}\Delta D_x &= \frac{\partial\left(\frac{\Delta E}{E}\right)}{\partial\sigma_x}\Delta\sigma_x\cdot 0.1\\ -\frac{1}{5.60\cdot 10^{-2}\ \text{m}}\cdot 3.333\cdot 10^{-3}\Delta D_x &= -5.204\cdot 10^{-5}\\ \longrightarrow \Delta D_x &= 8.743\cdot 10^{-4}\ \text{m}\\ \frac{\Delta D_x}{D_x} &= 1.561\cdot 10^{-2}\end{aligned}$$

The total energy spread error can then be calculated to

$$\begin{aligned}\Delta\left(\frac{\Delta E}{E}\right) &= \sqrt{(-5.204\cdot 10^{-5})^2+(4.629\cdot 10^{-4})^2+(-4.603\cdot 10^{-5})^2+(-5.204\cdot 10^{-4})^2}\\ &= 7.000\cdot 10^{-4}\\ \frac{\Delta\left(\frac{\Delta E}{E}\right)}{\left(\frac{\Delta E}{E}\right)} &= 2.100\cdot 10^{-1}\end{aligned}$$

Table 6.3 summarises the theoretical parameter values and the allowed absolute and relative errors for the energy spread measurement at the laser-wire location.

6.5.8.3 Independent emittance measurement ($\frac{\Delta E}{E} \neq 0$)

For a self-sufficient measurement of the beam emittance at any point in the transfer line, laser-wire monitors have to be set up at three different locations along the line (see Eq. 3.84). For the measurements to be independent of energy spread, the LW locations are chosen to be where

Table 6.3: Parameter values and errors for the energy spread measurement.

Parameter	Theoretical value	Allowed error	
		absolute	relative
β_x	12.45 m	44.82 mm	0.36%
σ_x	549.69 µm	10.00 µm	1.82%
ε_x	21.47 nm·rad	776.69 pm·rad	3.62%
D_x	56.00 mm	0.87 mm	1.56%
$\frac{\Delta E}{E}$	$3.333 \cdot 10^{-3}$	$7.000 \cdot 10^{-4}$	21%

$D_x = 0$. The LW locations and the reference point together with their values for β_x, α_x and σ_x are shown in Fig. 6.26.

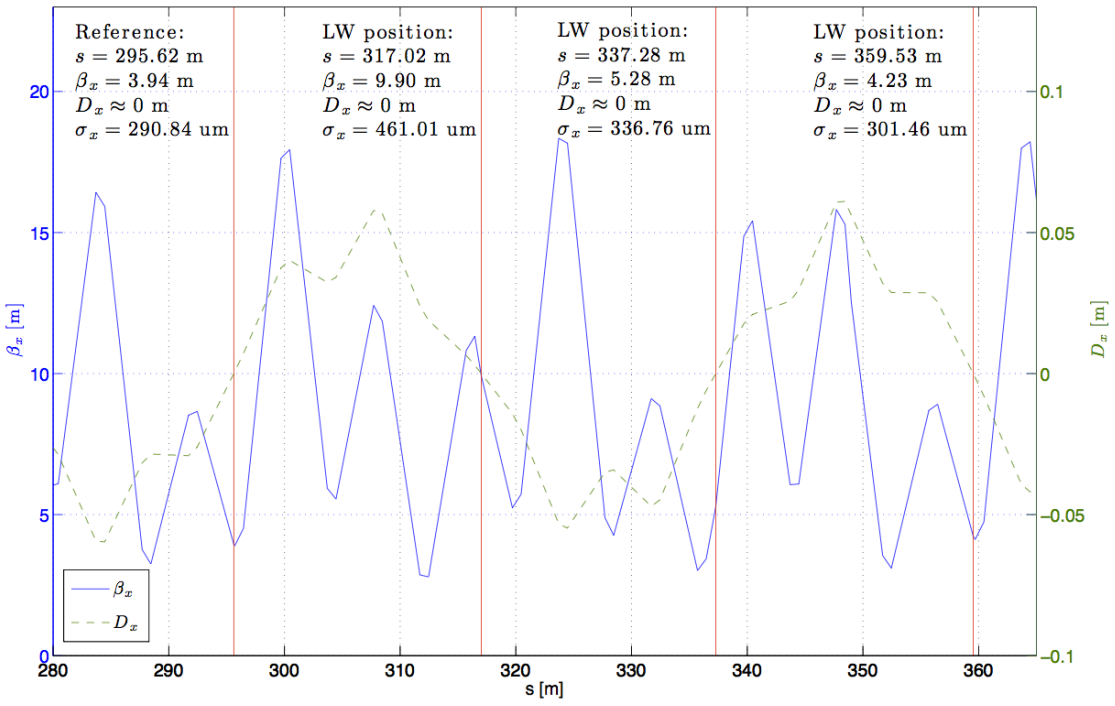

Figure 6.26: Studied locations for a three-fold laser-wire experiment, optimised for measuring the emittance independently.

The transfer matrices between the reference point s_0 and the LW locations $s_{1,2,3}$ are

$$M(s_1|s_0) = \begin{pmatrix} R_{11} & R_{12} \\ R_{21} & R_{22} \end{pmatrix} = \begin{pmatrix} -1.5941 & -0.1196 \\ 0.1471 & -0.6163 \end{pmatrix},$$

$$M(s_2|s_0) = \begin{pmatrix} 1.1700 & 0.1668 \\ 0.3549 & 0.9053 \end{pmatrix}, \; M(s_3|s_0) = \begin{pmatrix} -1.0516 & -0.2128 \\ 0.0256 & -0.9458 \end{pmatrix}.$$

With these and following Eq. 3.83, $\mathcal{M}_\sigma$ can be calculated to

$$\mathcal{M}_\sigma = \begin{pmatrix} 2.5410 & 0.3813 & 0.0143 \\ 1.3690 & 0.3904 & 0.0278 \\ 1.1058 & 0.4475 & 0.0453 \end{pmatrix}. \tag{6.22}$$

Now using the theoretical beam size at the LW locations, the emittance can be calculated. With a Monte-Carlo (MC) simulation, the emittance error was determined (see Fig 6.27).

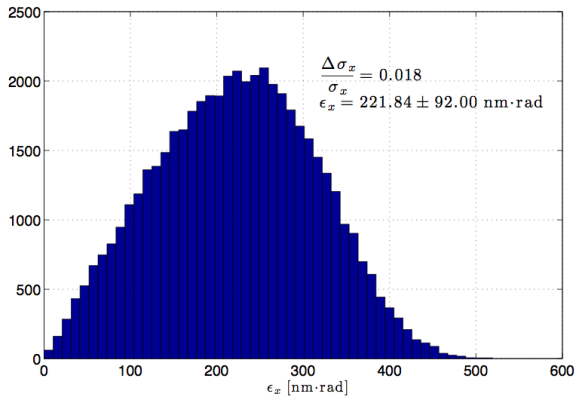

Figure 6.27: MC simulation of the emittance measurement with an LW transversal profile measurement error of 1.8%.

It can be seen that with this configuration the measurement does not deliver the correct result. Therefore, the procedure was repeated for various input LW scan errors. Fig. 6.28 shows MC simulated emittance and emittance error versus increasing LW transversal profile measurement error.

Only with a relative error of $\frac{\Delta\sigma_x}{\sigma_x} \leq 10^{-5}$, is the correct emittance achieved with a realistic measurement error. This is due to the fact that the rows in the transformation matrix $\mathcal{M}_\sigma$ are too similar to each other. Therefore, inversion delivers a matrix with very large values which results in small beam size errors causing drastic changes in emittance.

6.5.8.4 Independent emittance measurement ($\frac{\Delta E}{E} = 0$)

In order to prove, that above method indeed works, the same procedure was repeated, but this time choosing locations with very different values for β_x. In order to make the beam size measurements independent of dispersion, the energy spread was set to $\frac{\Delta E}{E} = 0$. The LW locations

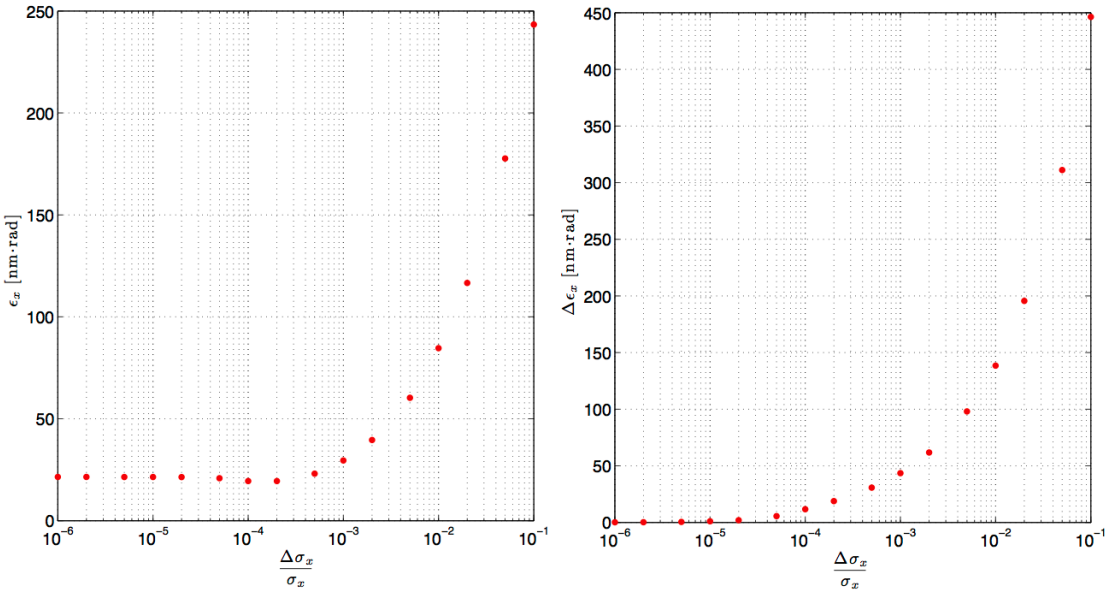

Figure 6.28: MC simulated emittance and emittance error versus increasing LW transversal profile measurement error.

and the reference point together with their values for β_x, α_x and σ_x are shown in Fig. 6.29.

With this setup, the transfer matrices between the reference point s_0 and the LW locations $s_{1,2,3}$ are

$$M(s_1|s_0) = \begin{pmatrix} 0.7452 & 2.9730 \\ -0.2889 & 0.1894 \end{pmatrix}, M(s_2|s_0) = \begin{pmatrix} -1.3321 & 3.8008 \\ -0.2498 & -0.0379 \end{pmatrix},$$
$$M(s_3|s_0) = \begin{pmatrix} -0.3478 & -3.5355 \\ 0.1523 & -1.3272 \end{pmatrix}.$$

This results in a transformation matrix $\mathcal{M}_\sigma$ as follows,

$$\mathcal{M}_\sigma = \begin{pmatrix} 0.5553 & 4.4308 & 8.8390 \\ 1.7745 & -10.1263 & 14.4465 \\ 0.1209 & 2.4591 & 12.4998 \end{pmatrix}. \tag{6.23}$$

Again, using the theoretical beam size at the LW locations, the emittance can be calculated. The MC simulated emittance distribution can be seen in Fig 6.30.

The correct emittance is achieved, but there is a tail on the lower end of the distribution. Therefore, the procedure was again repeated for various input LW scan errors to check why this

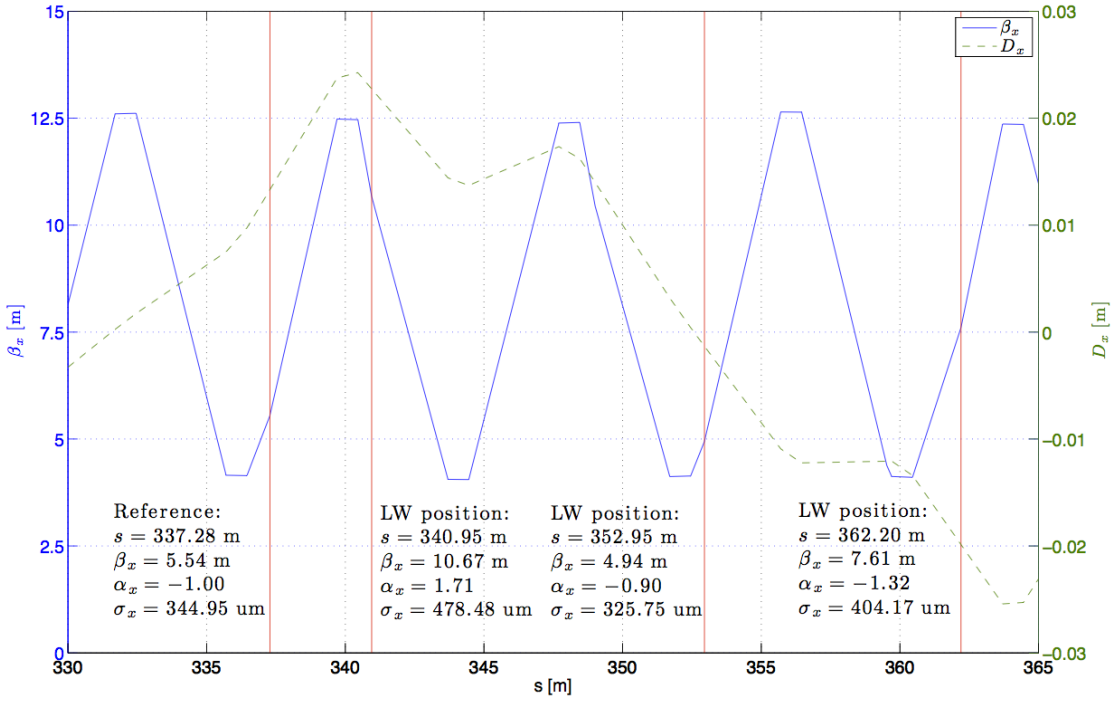

Figure 6.29: Studied locations for a three-fold laser-wire experiment, optimised for measuring the emittance independently ($\frac{\Delta E}{E} = 0$).

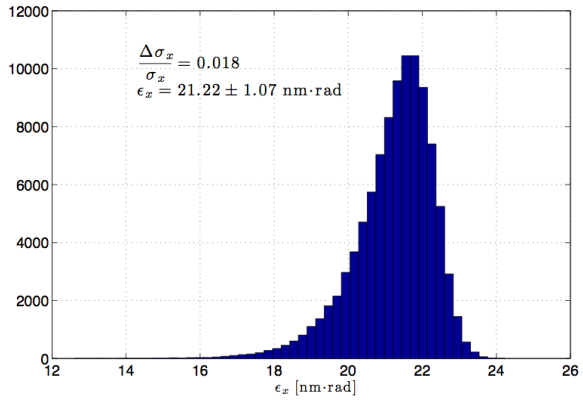

Figure 6.30: MC simulation of the emittance measurement with an LW transversal profile measurement error of 1.8%.

happens. Fig. 6.31 shows MC simulated emittance and emittance error versus increasing LW transversal profile measurement error.

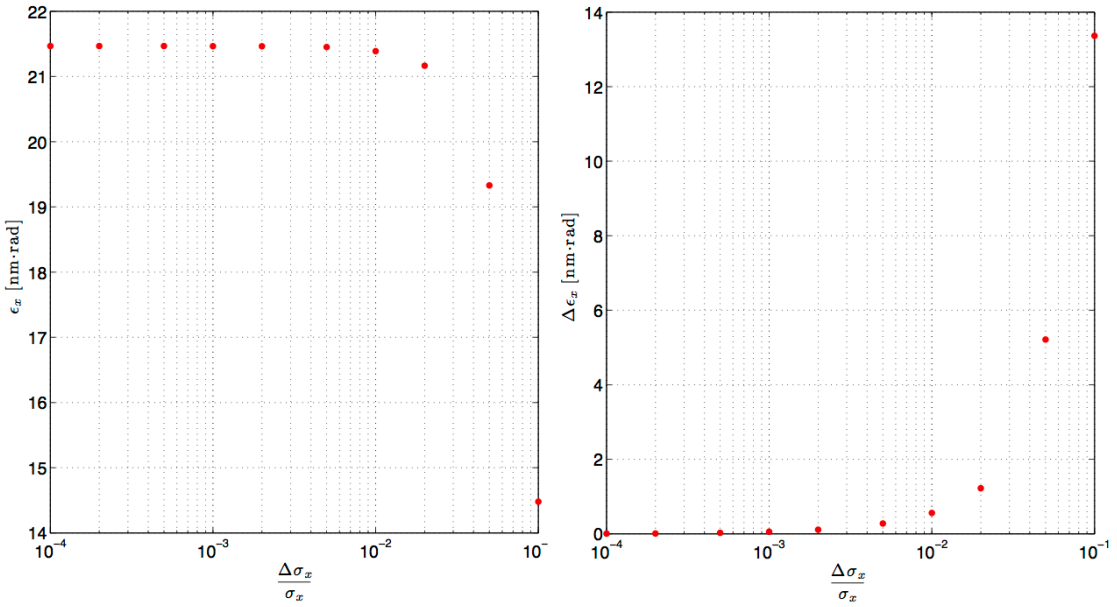

Figure 6.31: MC simulated emittance and emittance error versus increasing LW transversal profile measurement error.

With the relative beam size error achieved at PETRA-III, the emittance error is right at the limit before blowing up. In order to improve the emittance error, the LW scan will have to run for a longer time to measure the transversal profile more accurately. For a decrease of beam size error by a factor 3, the scan will have to take about 10 times longer.

It can be seen, that for an independent emittance measurement the locations will have to be chosen very carefully to avoid error blow-ups. For locations with $D_x \neq 0$, the energy spread will cause an increase in transversal beam size, so will therefore have to be factored out in a different way, for instance with a fourth LW location providing an independent measurement.

6.6 Summary

A PETRA-III type laser-wire system was investigated for installation at the CLIC Drive Beam transfer line TL2. Using MADX and BDSIM simulations were carried out the to model the possibility of installing one or more laser-wire systems along the straight section. A Cerenkov detector similar to the one used for the LW at ATF2 was assumed. Simulations showed that the detector can be located behind the bending dipole magnet at the end of the long straight

section, where the electron beam will be separated from the Compton photons. The detection efficiency along the straight section was determined. The nominal signal is 619.2 detected Compton photons per bunch, which is well above this background (about 4 bremsstrahlung photons per bunch). Measurement sensitivity was determined. Several locations of a possible LW system were studied for different purposes, i.e. measuring the emittance or the energy spread of the beam. Also the possibility of a three-fold laser-wire setup was investigated to enable an independent measurement of the emittance.

Chapter 7

Conclusions and Outlook

7.1 Summary and main conclusions

The PETRA-III laser-wire was studied in great detail and its key parameters in both scan directions were measured. The transversal profile of the laser pulse was modelled taking into account that the laser was running not with a single but rather multiple modes. The resulting fit is described by a linear combination of the first two Hermite polynomials. The longitudinal development of the transversal fit parameters were measured. The smallest vertical laser spot size was measured to be $\sigma_{\text{Laser},V} = 12.53 \pm 0.16$ µm and the minimum horizontal laser spot size was $\sigma_{\text{Laser},H} = 21.22 \pm 0.14$ µm

The laser-wire was then used to perform transversal beam scans. Beam studies were carried out and the results were compared to the synchrotron radiation imaging system at the other end of the ring. The discrepancy between the results of the two systems was investigated and several effects were considered: a laser tilt resulting in coupling between the horizontal and vertical plane; an unforeseen vacuum window effect leading to a blow-up of the laser spot size; and possible scaling issues which were ruled out by bumping the beam.

Varying the current in the skew quadrupoles at either side of the LW, the transversal beam ellipse was adjusted. Beam scans were performed in both directions to measure the change in beam size and to determine the minimum ellipse skew. For both axes, the beam ellipse was measured to be at its minimum when both skew quadrupoles are set to their default current. By shifting the RF frequency and measuring the change in the centroid location of the transversal profile, the horizontal and vertical dispersion at the LW location were determined. The results

are $D_x = 140.42 \pm 2.51$ mm and $D_y = -2.08 \pm 1.12$ mm.

The application of a laser-wire system similar to the at PETRA-III was studied for the CLIC Drive Beam transfer line TL2. The transfer line was modelled using MADX and BDSIM to investigate the possibility of installing one or more laser-wire systems along the straight section. A Cerenkov detector similar to the one used for the LW at ATF2 was assumed. Simulations showed that the detector is suitably located behind the bending dipole magnet at the end of the straight section, where the electron beam will be separated from the Compton photons. The detection efficiency along the straight section was determined. Several locations of a possible LW system were studied for different purposes, i.e. measuring the emittance or the energy spread of the beam. Also the possibility of a three-fold laser-wire setup was investigated to enable an independent measurement of the emittance.

Many laser-wire systems are required for CLIC. The small beam sizes in the Main Beam (especially the RTML and the BDS) ask for a emittance measurement section similar to the setup at ATF2, where micron-scale optics have been shown. The low energy and comparatively large beam sizes in the Drive Beam are similar to the parameters at PETRA-III. However, the background of both laser-wires at PETRA-III and ATF2 is low. The high current in the Drive Beam is a new area for LW type diagnostics. Despite the investigations carried out in this work, background could still be an issue and requires studies in more detail. There could also be other problems associated with high charge, for example possible beam halo effects. For this the background in CTF3, the Two-beam Test-stand studying the two-beam acceleration scheme envisioned in CLIC, should be modelled and possibly tested.

Furthermore, for a LW setup at TL2, the signal extraction will have to be developed. This has in fact to be applied to all laser-wires at CLIC.

7.2 Future work - PETRA-III laser system upgrade

Evidently, the main liability in a LW measurement is the actual laser. Therefore, to improve the performance of the PETRA-III LW, a new laser is currently being installed [48]. The new laser system is a Master Oscillator Power Amplified (MOPA) system consisting of a solid-state oscillator, pulse stretcher, regenerative pre-amplifier and two further amplification stages. All of these amplification stages are fibre based.

- The oscillator is a Nd:VO_4 mode-locked solid-state laser emitting pulses at 1064 nm. The pulse repetition rate is 62.45 MHz and the pulse duration is 10 ps. The repetition rate is the 8th subharmonic of the PETRA-III main clock (499.6 MHz). The pulse energy at the laser output is approximately 10 nJ. An integrated acousto-optic pulse picker within the laser reduces the output repetition rate, which can be selected by the user in a range between 50 and 1000 kHz.

- The stretcher unit is a 4-pass grating based pulse stretcher which increases the pulse length from 10 ps to about 200 ps FWHM. Efficiency of the gratings is about 70% at each passage, giving a total efficiency of about $20-25\%$. The pulse energy at the output of the stretcher is $2-2.5$ nJ.

- The pre-amplifier is a Nd-doped single mode polarisation maintaining fibre. The pumping source is a CW fibre pigtailed laser diode at 808 nm. The pump power is about 300 mW. The pulse energy of the laser is increased by this amplification stage to about $10-15$ nJ, which is slightly more than the original values.

- The first amplification stage is also a Nd-doped single mode polarisation maintaining fibre. The pumping source is also a CW fibre pigtailed laser diode at 808 nm but with a power of about 2 W. At this amplification stage, the pulse energy of the laser is increased to about 200 nJ.

- The second amplification stage is a Yb-doped single mode polarisation maintaining large mode area (LMA) fibre with a core diameter of 20 µm. The pumping source is also a CW fibre pigtailed laser diode but its wavelength is 976 nm and the output power is about 20 W. The pulse energy of the laser after this final amplification stage is increased to about $2-10$ µJ.

The corresponding pulse power for a 200-ps pulse is $10-50$ kW. The laser pulses are injected into a single mode photonic crystal fiber (PCF) with diameter of 25 µm. The total length of the fibre is about 25 m and it will transport the laser beam to the final focus lens without any complications regarding alignment or focus aberrations. The output laser beam will be collected by a single LAP125 lens in order to refocus it obtaining a sigma at the focus of about 6 µm.

This system has several advantages. Since the laser is coming from a single mode fibre, the transverse profile for mode TM00 has an M^2 of very close to 1 (see Fig. 7.1 (a) and (b). Also, the

longitudinal profile is perfectly smooth as it is inherent for mode-locked lasers (no intra-mode beating), as is shown in Fig. 7.2) Temporal synchronisation is much more efficient as the laser pulse length of 200 ps FWHM matches almost perfectly the bunch length, which has a sigma of about 40 ps. This means that all the photons will be interacting with the bunch as opposed to the former 5 ns pulse where only 4% overlap was achieved. Furthermore, beam transport and final focus are part of a stable system and not subjected to misalignment. Transversal jitter is virtually negligible as the laser will be coming from a stable assembly of fibre and final lens. Finally, the data rate will increase by a factor of 2500 which will makes for a faster and more statistically valid data acquisition.

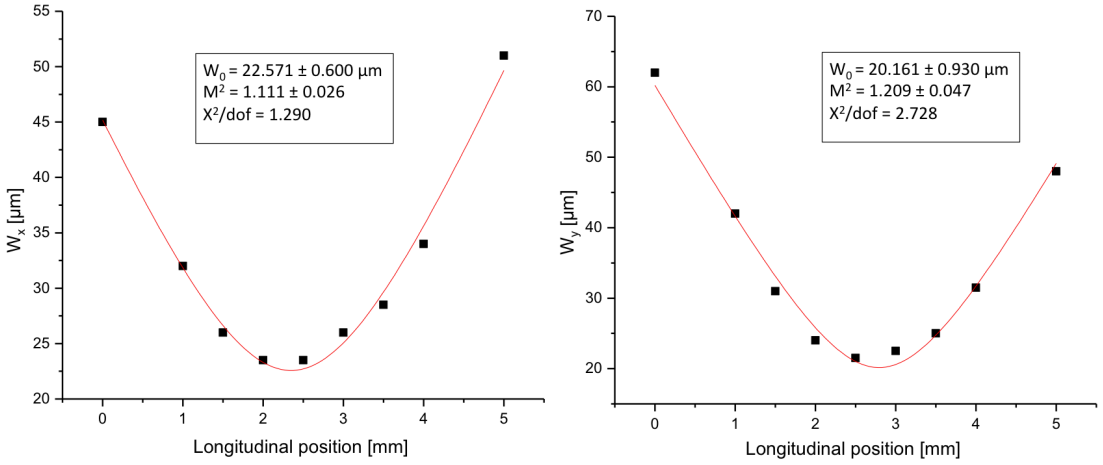

(a) Horizontal: $M^2 = 1.111 \pm 0.026$.

(b) Vertical: $M^2 = 1.209 \pm 0.047$.

Figure 7.1: Longitudinal development of the horizontal (a) and vertical (b) spot size of the laser before entering the fibre [48].

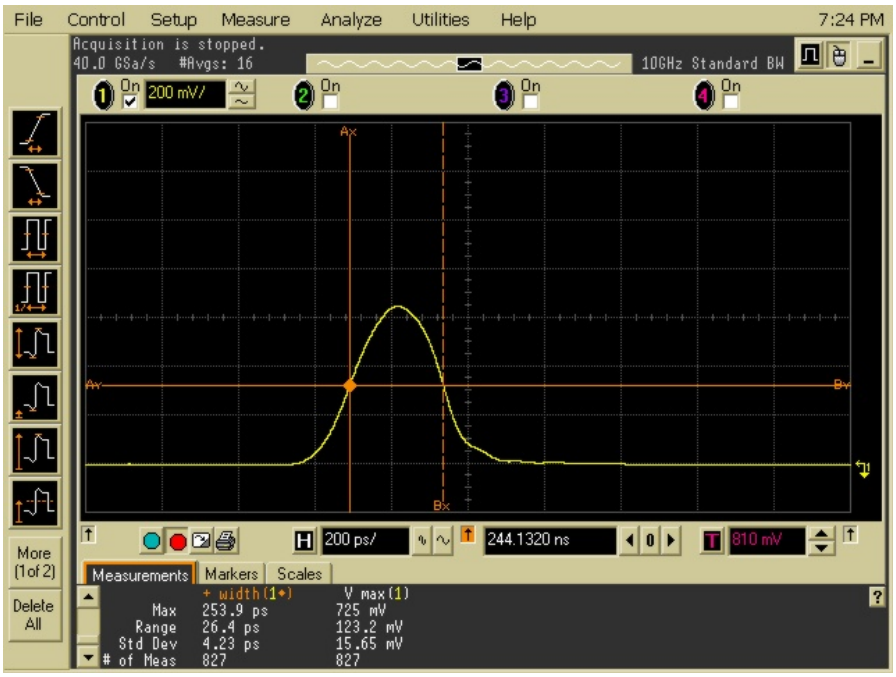

Figure 7.2: Oscilloscope trace showing a single laser pulse taken with a 12.5-GHz photodiode and a 10-GHz oscilloscope with a sampling rate of 40GSa/s [48].

Bibliography

[1] H. Braun, CLIC 2008 Parameters, CLIC Note 764.

[2] CLIC Conceptual Design Report, http://project-clic-cdr.web.cern.ch/project-CLIC-CDR/, in preparation.

[3] F. Tecker, CLIC and Room Temperature RF, Fifth International Accelerator School for Linear Colliders (Oct 2010).

[4] CLIC Parameter Table, http://clic-meeting.web.cern.ch/clic-meeting/clictable2010.html (July 2011).

[5] A. Anderson, J. P. H. Sladen, RF-Based Electron Beam Timing Measurement with Sub-10fs Resolution, CLIC Note 734.

[6] E. Bravin, T. Lefèvre, C. Vermare, OTR Studies for the High Charge CTF3 Beam, CLIC Note 570.

[7] T. Lefèvre, CLIC beam sizes, private communication (Dec. 2012).

[8] M. Ross, et al., A Very High Resolution Optical Transition Radiation Beam Profile Monitor, SLAC-PUB 9280.

[9] H. Hayano, Wire Scanners for Small Emittance Beam Measurement in ATF, Linac2000 MOC01.

[10] J. Alabau-Gonzalvo, et al., Multi Optical Transition Radiation System for ATF2, IPAC'10 MOPE050.

[11] K. Iida, et al., Measurement of an electron-beam size with a beam profile monitor using Fresnel zone plates, Nucl. Instrum. Meth. A 506 (1-2) (2003) 41 – 49.

[12] S. Takano, other, X-ray imaging of a small electron beam in a low-emittance synchrotron light source, Nucl. Instrum. Meth. A 556 (1) (2006) 357 – 370.

[13] M. Sjöström, et al., Characterisation of the MAX-II Electron Beam: Beam Size Measurements, EPAC'06 TUPCH090.

[14] R. Alley, et al., A laser-based beam profile monitor for the SLC/SLD interaction region, Nucl. Instrum. Meth. A 379 (3) (1996) 363 – 365, ¡ce:title¿Proceedings of the Sixth International Conference on Instrumentation for Experiments at e+ e- Colliders¡/ce:title¿.

[15] E. J. N. Wilson, An Introduction to Particle Accelerators, Oxford University Press, 2001.

[16] L. C. Deacon, A Micron-Scale Laser-Based Beam Profile Monitor for the International Linear Collider, Ph.D. thesis, Royal Holloway, University of London (2009).

[17] A. H. Compton, A Quantum Theory of the Scattering of X-rays by Light Elements, Phys. Rev. 21 (1923) 483–502.

[18] P. Tenenbaum, T. Shitake, Measurement of Small Electron-Beam Spots, Ann. Rev. Nucl. Part. Sci. 49 (1999) 125–162.

[19] A. E. Siegman, Lasers, University Science Books, 1986.

[20] A. E. Siegman, How to (maybe) measure laser beam quality, OSA Trends Opt. Photon. 17 (1998) 184–199.

[21] I. Agapov, G. A. Blair, M. Woodley, Beam emittance measurement with laser wire scanners in the International Linear Collider beam delivery system, Phys. Rev. ST Accel. Beams 10 (2007) 112801.

[22] L. C. Deacon, G. A. Blair, Laser Wire Simulation in the ILC Beam Delivery System, EUROTeV-Report-2008 018.

[23] S. Y. Lee, Accelerator Physics, World Scientific, 2004.

[24] G. Arduini, et al., LEP Operation and Performance with 100 GeV Colliding Beams, CERN-SL-2000-045-OP.

[25] K. Balewski, (ed.), et al., PETRA III: A Low Emittance Synchrotron Radiation Source. Technical Design Report, DESY-04-035.

[26] Machine Parameters PETRA III (Design Values), http://hasylab.desy.de/facilities/petra_iii/machine/parameters/index_eng.html (September 2011).

[27] G. Kube, et al., PETRA III Diagnostics Beamline for Emittance Measurements, IPAC'10 MOPD089.

[28] A. Bosco, et al., A Two-Dimensional Laser-Wire Scanner for Electron Accelerators, Nucl. Instrum. Meth. A 592 (3) (2008) 162–170.

[29] Y. Liu, et al., Laser Wire Beam Profile Monitor at SNS, EPAC'08 TUPC061.

[30] M. T. Price, Laser-Wire Studies for PETRA and the International Linear Collider, Ph.D. thesis, Royal Holloway, University of London (2007).

[31] Specifications for the WinCamD-UCM CCD camera, http://www.lambdaphoto.co.uk/pdfs/WinCamD_UCM.pdf (July 2012).

[32] Specifications for the Basler A601f CMOS camera, http://www.baslerweb.com/media/documents/BD00037602_Basler_A60xf_EMVA_Standard_1288.pdf (July 2012).

[33] P. Bartkiewicz, P. Duval, Tine as an accelerator control system at desy, Meas. Sci. Technol. 18 (8) (2007) 2379.

[34] Specifications for the NI PXI-5152 2 GS/s Digitizer/Oscilloscope, http://sine.ni.com/ds/app/doc/p/id/ds-247/lang/en (Jan 2013).

[35] G. Boorman, LW data acquisition, timing and synchronisation, private communication (Oct. 2011).

[36] G. K. Sahoo, PETRA III Optics - MADx input files, http://www.desy.de/~sahoo/WebPage/PETRA%20III%20Optics%20-%20MADx%20input%20files/ (October 2011).

[37] G. Kube, PETRA-III machine parameters, private communication (Jun. 2012).

[38] R. Wanzenberg, K. Balewski, Observation of Intensity Dependent Single Bunch Effects at the Synchrotron Light Source PETRA III, IPAC'11 MOPS055.

[39] S. T. Boogert, et al., Micron-scale laser-wire scanner for the KEK Accelerator Test Facility extraction line, Phys. Rev. ST Accel. Beams 13 (2010) 122801.

[40] S. T. Boogert, et al., A Laser-Wire System at the ATF Extraction Line, EPAC'06 MOPLS080.

[41] K. Nakamura, P. D. Group, Review of Particle Physics, J. Phys. G 37 (7A) (2010) 075021.

[42] MAD - Methodical Accelerator Design, `http://madx.web.cern.ch/madx/` (April 2012).

[43] PTC User's Reference Manual, `http://frs.web.cern.ch/frs/PTC_reference_manual/PTC_reference_manual.html` (April 2012).

[44] S. Agostinelli, et al., Geant4 - A Simulation Toolkit, Nucl. Instrum. Meth. A 506 (2003) 250 – 303.

[45] I. Agapov, G. A. Blair, S. Malton, L. Deacon, BDSIM: A particle tracking code for accelerator beam-line simulations including particle-matter interactions, Nucl. Instrum. Meth. A 606 (3) (2009) 708 – 712.

[46] T. Lefèvre, CLIC Drive Beam parameters, private communication (Apr. 2011).

[47] T. Lefèvre, Laser Wire Scanner: Basic Process and Perspectives for the CTFs and CLIC Machines, CLIC Note 504.

[48] A. Bosco, PETRA-III fibre laser system upgrade, private communication (May 2012).